The Dissertation Committee for Xiang Li Certifies that this is the approved version of the following dissertation:

Paper-based Electrochemical Platforms for Separation, Enrichment, and Detection

Committee:

Richard M. Crooks, Supervisor

Keith J. Stevenson

Jason B. Shear

Charles Buddie Mullins

Charles J. Werth

Paper-based Electrochemical Platforms for Separation, Enrichment, and Detection

by

Xiang Li, B.E.

Dissertation

Presented to the Faculty of the Graduate School of

The University of Texas at Austin

in Partial Fulfillment

of the Requirements

for the Degree of

Doctor of Philosophy

The University of Texas at Austin

May, 2017

Dedication

To my parents,

Jinqiang Li and Rong Li

Acknowledgements

I would like to sincerely thank my research advisor, Prof. Richard M. Crooks, who made this journey possible and wonderful. His patience, guidance and support in all these years led me to grow in both science and life.

I would like to thank my committee members at the University of Texas at Austin: Prof. Buddie Mullins, Prof. Jason Shear, Prof. Keith Stevenson, Prof. Charles Werth, for helping me finish my graduate study.

I would also like to thank Prof. Xinghua Xia (Nanjing University) and Prof. Shaowei Chen (UC Santa Cruz), who are my undergraduate mentors and prepared me for the PhD program.

My gratitude goes to my fellow Crooks group members for their assistance in the laboratory, especially my collaborators: Dr. Long Luo, Dr. Hong Liu, Dr. Christophe Renault, and Dr. Karen Scida. Special thanks go to Angie Missildine and Betsy Hamblen, who have been incredibly helpful and let me focus on my research.

Last but not least, I want to thank my parents and family, who have always been the reason why I can keep going.

Paper-based Electrochemical Platforms for Separation, Enrichment and Detection

Xiang Li, Ph. D.

The University of Texas at Austin, 2017

Supervisor: Richard M. Crooks

Paper based analytical devices (PADs) have great potential in the application of point-of-care diagnosis. This dissertation focuses on the design and application of PADs, especially ones that integrate with electrochemical systems, to tackle various problems in analytical chemistry, such as multi-analyte separation, sample enrichment, and sensitive detection. Four types of PADs are described in this dissertation.

The first PAD (oPAD-Ep) is designed for multi-analyte separation. The oPAD-Ep is fabricated using the principle of origami to create a stack of connected paper layers as an electrophoresis channel. Due to the thinness of paper, a high electric field can be achieved with low voltage supply. Serum proteins can be separated and the device can be unfolded for post-analysis.

The second PAD (oPAD-ITP) is designed on a similar principle as the oPAD-Ep, but it is applied for sample

enrichment. The major modification is to adjust electrolyte conditions to enable isotachophoretic enrichment of analytes. DNA with various lengths can be enriched within a few minutes, and can be collected on one of the paper folds.

The third PAD (hyPAD) also focuses on sample enrichment. The device is assembled with two different paper materials, nitrocellulose and cellulose. The hyPAD can perform faradaic ion concentration polarization experiments. This technique uses faradaic electrochemistry to create a local electric field gradient in the paper channel and can enrich charged analytes including: DNA, proteins, and nanoparticles.

The fourth PAD (oSlip-DNA) focuses on sensitive electrochemical detection of DNA hybridization assays. This method integrates magnetic enrichment and electrochemical signal amplification via silver nanoparticles. Using voltammetry, sensitive detection of Hepatitis B Virus DNA is achieved on the low-cost device.

Table of Contents

List of Tables

List of Figures

List of Illustrations

Chapter 1: Introduction

1.1 Paper Based Analytical Devices

Point-of-care (POC) diagnostics deliver rapid test results directly to patients at the time of care.[1,2] POC testing allows patients to be diagnosed in the physician`s office, an ambulance, the home, the field, or in the hospital, and it can be performed in resource-limited settings without help from laboratory trained personnel or complicated instruments. The World Health Organization designates the guidelines for POC testings as ASSURED: Affordable, Sensitive, Specific, User-friendly, Rapid and Robust, Equipment free, and Deliverable to end-users.[3] A variety of materials have been used to construct POC device,[4,5] especially glass,[6,7] plastic,[8,9] and paper.[2,8,10] Compared to glass and plastic, paper has several properties that make it more suitable for some POC applications. (1) Paper is porous with micro-structured hydrophilic cellulose backbones, which enables capillary flow without pump installation.[11] (2) Paper is robust but yet flexible enough to be folded, bent, or cut, which enables easier manufacturing.[12,13] (3) Paper is biocompatible and also fairly chemically inert, so that it can host most bioassays without biomolecule denaturation or reaction interference.[14]

(4) Paper is cheap and easy to produce at large scale, which lowers the material cost.

There are a few examples of using paper for POC applications in the last century. For instance, in 1949 Muller and coworkers conducted the preferential elution of a mixture of pigments in a restricted channel on ordinary filter paper.[15] In the 1970s, nitrocellulose paper based lateral flow assay was developed for the detection of human chorionic gonadotropin (hCG) which lays the groundwork for modern home pregnancy tests.[16] In the 1987, Matthews et al. designed a pen-sized glucose meter that used a paper strip to electrochemically measure glucose concentration in whole blood.[17] This device was then modified and finally evolved to become the commercially available personal glucose meter (PGM).

The paper-based analytical device (PAD) concept emphasizes the application of paper not only as a substrate but also as a complete device with specific functions. This concept was first introduced by the Whitesides group in 2007.[18] They patterned chromatography paper via photolithographic method into well-defined hydrophilic channels bounded by hydrophobic barriers. Sample solution wicks through channels and reacts with reagents that were pre-loaded on the paper. Simultaneous colorimetric detection of glucose and bovine serum albumin were achieved.[18] The

sample volume was small (a few microliters), the assay time short (a few minutes), the readout method simple (naked eye), and the device cost low (<$2 USD). The important outcome of the Whitesides publication was to show that the PAD concept is a natural fit for POC. Soon after their paper was published, PAD-based assays became a focus of research worldwide.

1.2 Fabrication of PADs

The very first step in PAD research is device fabrication, which aims at improving the stability of PADs and lowering the manufacture time and cost. The most common fabrication methods are photolithography[18,19] and wax printing.[20,21]

Photolithographic methods use hydrophobic photoresist on hydrophilic paper to pattern well-defined channels. The advantages of this method include high channel resolution, stable structures, and low leakage. However, this method involves expensive equipment, organic solvents (less bio-compatible), and is time consuming to implement.

Wax printing uses a commercially available inkjet printer to directly print solid wax on the surface of paper, which is followed by a thermal treatment to melt the wax through the thickness of the paper. This method is low-cost,

accessible, and very flexible, which makes it popular and widely used. Nevertheless, the drawbacks of wax printing, compared to photoresist, include lower resolution, lower stability, and incompatibility with organic solvents.

Besides these two methods, other fabrication methods have also been reported, such as plasma treatment,[22] plotting,[23] cutting,[24] inkjet printing,[25,26] vapor phase deposition,[27] Flexographic printing,[28] and stamping.[29]

1.3 Designs of PADs

Creative designs of PADs have been developed to fit specific applications.[30] Due to the flexibility and thinness of paper, PADs can be designed in very different ways compared to conventional microfluidic devices.[10,31] In this section, several design ideas that make PADs multi-functional and that are related to the work in this dissertation are introduced.

1.3.1 Multi-dimensional PADs.

Three-dimensional (3D) microfluidic systems can add more flow pathways and significantly expand device capabilities for analysis.[32] For conventional plastic and glass microfluidic devices, 3D fabrication has been achieved by methods such as multilayer soft lithography,[33] membrane stacking,[34] vertical passages,[35] and discrete

stereolithography.[36] However, these fabrication methods are usually time consuming and come with at a high cost, which make them not suitable for POC applications. Paper, on the other hand, differs from plastic and glass in its porous structure, thinness, and soft mechanical strength. These properties enable novel 3D fabrication methods.

In 2009, Whitesides and co-workers patterned multiple layers of paper and stacked them with adhesive tape (Illustration 1.1).[19] Holes ere punched in the adhesive tape, and then the holes were filled with cellulose powder. When the channels on different layers were aligned, fluids could be transported vertically between layers in a 3D fashion via the holes.

In 2011, Crooks and co-workers significantly simplified the 3D paper fabrication by using the principle of paper folding (Illustration 1.2) to produce a family of PADs which are called oPADs (o stands for origami).[12,37] Compared with the stacking method developed by Whitesides, the origami technique is advantageous for several reasons. First, the entire device can be fabricated on one piece of paper, instead of sequential layer-by-layer fabrication on multiple pieces. This saves time and reduces cost. Second, layers assembled by folding do not require adhesive tape or special alignment. Third, the device can be unfolded for post-assay analysis.

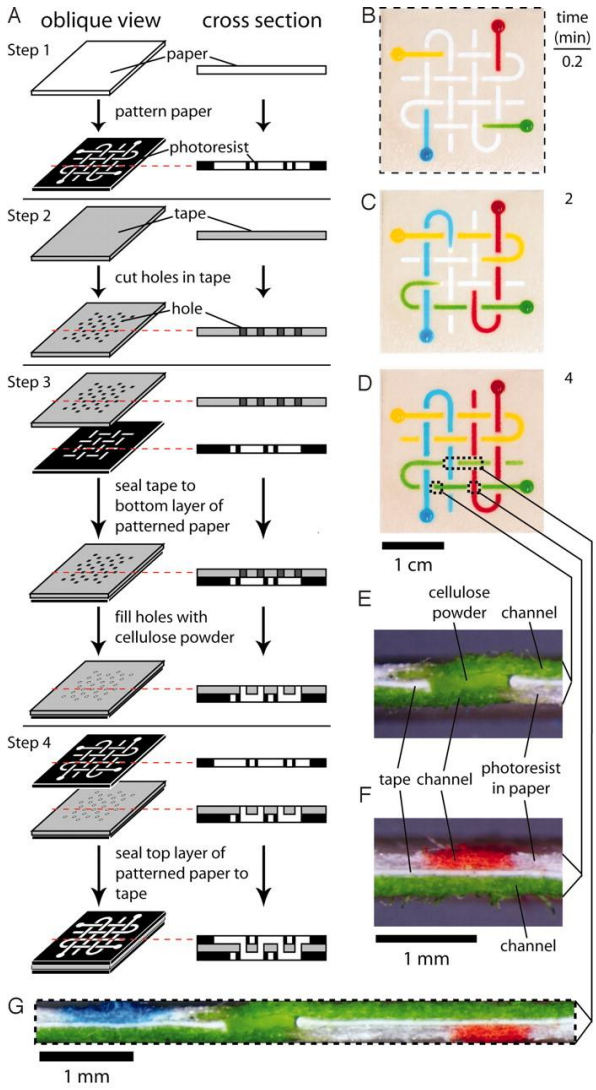

Illustration 1.1. *Demonstration of a 3D PAD by stacking. (A) Fabrication. (B, C, D) Photographs of a basket-weave system taken at different times after adding red, yellow, green, and blue aqueous solutions of dyes to the sample reservoirs. (E, F, G) Cross sections of the device showing the layers and the distribution of fluid in each layer of the device shown in (D). Image sourced from Reference 19.*

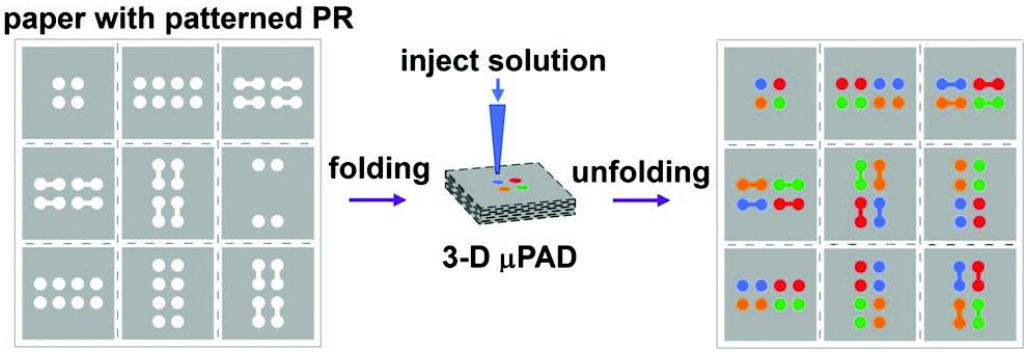

Illustration 1.2. *Demonstration of a 3D PAD by origami. A 3D PAD fabricated based on the principle of origami. Image sourced from Reference 12.*

1.3.2 Flow rate control systems.

Unlike conventional microfluidic systems in which pressure driven flow is applied and controlled through pumps, the porous structure and hydrophilicity of paper (cellulose matrix) enables on-chip capillary flow.[11] *As a result, sample solution can wick through the channels, which eliminates the requirement for external pumping. The capillary driven flow in a straight paper channel can be described by the Washburn equation (eq 1.1).*[38]

$$L^2 = \frac{\gamma D t}{4\eta} \qquad (1.1)$$

It shows the square of distance (L) is proportional to the liquid surface tension (γ), pore diameter (D), time (t), and inversely proportional to the liquid dynamic viscosity (η). This equation indicates that the flow rate decreases at longer times.[39] *To fit applications that require precise*

timing, different flow rate control systems have been developed on PADs.

A direct and obvious deduction from Washburn`s equation is that longer channels take a longer time to fill. Therefore, several groups have designed channels with different lengths and shapes, so that it takes different time for fluids to reach the end of channels.[11,39,40] *By this method, programmable and sequential reagent delivery can be achieved on PADs.*

Other design ideas take more complicated approaches. For example, Yager and co-workers designed dissolvable barriers to tune the flow rate. In their experiment, the authors pre-dried sugar (trehalose) barriers in the channels.[11,41] *When wicking up to the sugar barrier, the fluids are slowed to different extents based on the dissolution of different amount of sugar. Shen and co-workers made paper cantilevers on a 2D PAD.*[22] *When lifted up, the cantilever broke the connection of the channel to stop the flow. This design enables manual control of the flow. Likewise, Liu and co-workers integrated a magnetic control system with a cantilever design on PADs.*[42] *Instead of manual control, the cantilever is modified with ferromagnetic nanoparticles and is controlled by a circuit with electromagnetic attraction.*

I have participated in developing two flow rate control systems on paper: the Slip PAD[43] and the hollow-channel PAD.[44-46] The Slip PAD (Illustration 1.3) is inspired by the Slip Chip concept developed by Ismagilov and co-workers.[47,48] In this device, two paper layers are patterned with mismatched channels. The mismatched channels can be connected when users slip one layer against the other. The manual handle of the device offers accurate timing to deliver the reagents. The hollow-channel PAD (Illustration 1.4) is based on the idea to add pressure driven flow to capillary flow.[44] To achieve this, paper cellulose is removed in the channel, and the bottom of the channel is maintained hydrophilic by partially modifying the surface. In the hollow-channel, only a drop of fluid (~20 μL) is enough to activate pressure driven flow and it is reported that the flow rate is 7 times faster than conventional paper channel.[44] Others also proposed alternative methods to create hollow channels.[49,50]

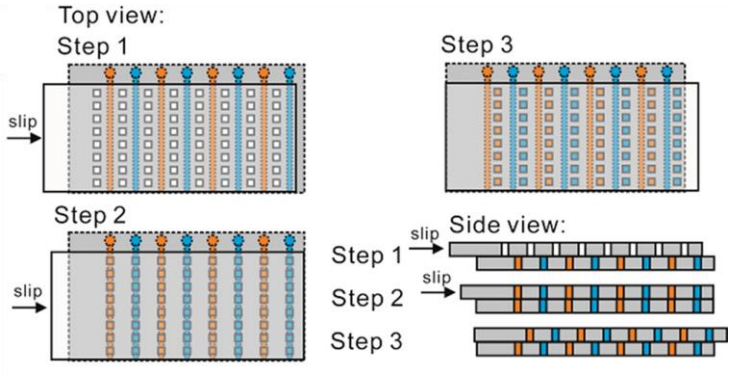

Illustration 1.3. Scheme for the Slip PAD. Two paper layers are patterned with mixmatched channels and zones. User can connect the channels and zones, with a simple slip function. Image sourced from Reference 43.

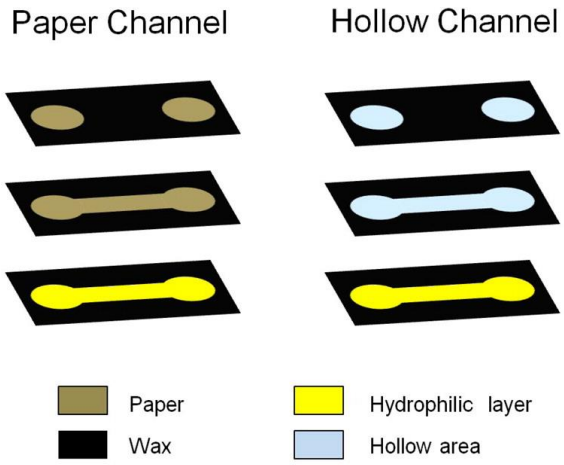

Illustration 1.4. Scheme for the hollow-channel PAD. In the hollow-channel, the paper cellulose is removed and the bottom of the channel is maintained hydrophilic by partially modifying the surface. Image sourced from Reference 44.

1.3.3 Electrochemistry.

Electrochemical analysis has great potential application in POC diagnosis for several reasons.[51,52] First, electrochemistry is quantitative and sensitive. Second, electrochemical measurements require only simple instrumentation. For example, a potentiostat can be manufactured at a cost of ~$100 USD and have the size of a regular cell phone.[53] Third, it is easy to integrate electrochemical systems on the device. The only requirement is electrode patterning on the device, which has been well developed.[54,55]

The first example of PAD based electrochemistry was reported by Henry and co-workers.[54] In the work, they patterned three sets of electrodes in three separated zones on paper. Each set of electrodes includes a working electrode, a reference electrode and a counter electrode. When electrochemical active biomolecules, such as uric acid, are present in the zones, electrochemical detection can be performed. Following that, a lot of electrochemical systems have been reported on paper, such as amperometric detection,[56] voltammetric detection,[57] potentiometric detection,[37,58] and photoelectrochemistry.[59]

1.4 Research Summary and Accomplishments

This dissertation focuses on combining and modifying the core design ideas mentioned in the section 1.3 and developing new PADs, especially ones that integrate with electrochemical systems, to tackle more specific problems in analytical chemistry, including multi-analyte separation, sample enrichment, and sensitive detection. These PADs are very easy to fabricate at low cost and do not require complicated instruments to run.

Specifically, Chapter 2 discusses the design of a 3D PAD (oPAD-Ep) for electrophoretic separation of serum proteins. The oPAD-Ep is fabricated based on the principle of origami to shorten the channel length. As a result, a high electric field that is required for electrophoresis can be achieved at with low voltage supply. Serum proteins can be separated onto different paper layers within a few minutes. This PAD design significantly lowers the high voltage requirement in conventional designs, thus making it more user-friendly and suitable for POC applications.

Chapter 3 presents a similar design as oPAD-Ep, however, focuses on the sample enrichment. The device (called oPAD-ITP) is also based on the origami design, and the electrolyte conditions in the channel are controlled so that isotachophoresis technique can be achieved. The oPAD-ITP is able to concentrate DNA with various lengths and

collect concentrated sample onto one of the paper folds for post-analysis. The PAD design can be integrated with other detection systems and lower the limit of detections by two orders of magnitude.

Chapter 4 discusses the faradaic ion concentration polarization experiments for sample enrichment on paper (hyPAD). The hyPAD uses faradaic electrochemistry to create a local electric field gradient in the paper channel and concentrate charged anlaytes with a counter-flow. The hyPAD can be tuned by electrochemical process and lower the limit of detection. The ability of the device is demonstrated with the enrichment of DNA, proteins, and nanoparticles.

Chapter 5 focuses on using electrochemical method for the detection of DNA hybridization assays on paper (oSlip-DNA). This electrochemical method integrates magnetic enrichment and electrochemical signal amplification via silver nanoparticles. The oSlip-DNA possesses a complicated 3D structure to enable microbead-based assay and timely control of the reagent transport. Sensitive detection of Hepatitis B Virus DNA to 85 pM is achieved on the device with a cost of 36 cents.

*Chapter 2: Low-Voltage Origami-Paper-Based Electrophoretic Device for Rapid Protein Separation**

2.1 SYNOPSIS

This chapter presents an origami paper-based electrophoretic device (oPAD-Ep), which achieves rapid (~5 min) separation of fluorescent molecules and proteins. Due to the innovative design, the required driving voltage is just ~10 V, which is more than 10 times lower than that used for conventional electrophoresis. The oPAD-Ep uses multiple, thin (180 μm/layer) folded paper layers as the supporting medium for electrophoresis. This approach significantly shortens the distance between the anode and cathode, and this, in turn, accounts for the high electric field (>1 kV/m) that can be achieved even with a low applied voltage. The multiple design of the oPAD-Ep enables convenient sample introduction by use of a slip layer as well as easy product analysis and reclamation after electrophoresis by unfolding the origami paper and cutting out desired layers. We demonstrate the use of oPAD-Ep for simple separation of proteins in bovine serum, which illustrates its potential applications for point-of-care diagnostic testing.

---

* *Chapter 2 is based on previous publication: L. Luo, X. Li and R. M. Crooks, Low-Voltage Origami-Paper-Based Electrophoretic Device for Rapid Protein Separation, Anal. Chem., 2014, 86, 12390-12397. LL and XL contributed equally to the work. RMC was the research advisor. LL and XL designed and performed the experiments. LL, XL, and RMC wrote the manuscript.*

2.2 Introduction

In this chapter, we introduce a new kind of electrophoretic (Ep) device, which is appropriate for integration into paper analytical devices (PADs),[3,60] and demonstrate separation of fluorescent molecules and proteins at very low voltages. The device, which we call an oPAD-Ep (the o stands for origami),[12] is very easy to construct (Illustration 2.1). Briefly, a piece of filter paper is folded into a multilayer structure that serves as the Ep medium. A slip layer is added to introduce the sample,[43] and this assembly is then sandwiched between two Ag/AgCl electrode assemblies. The important new finding is that an electric field of a few kilovolts per meter can be easily generated in an oPAD-Ep using an applied voltage of just 10 V due to the thinness of the folded paper (~2 mm thick for an 11-layer origami construct). In contrast, a much higher applied voltage (100-300 V) is required to achieve a similar field using a conventional Ep apparatus.[61] In addition, the multilayer structure of this device offers several important advantages. First, a separate slip layer is easily incorporated in oPAD-Ep for sample introduction.[43] The position of the slip layer determines the initial location of sample. Second, product analysis after Ep is easily

performed by unfolding the device, and the resolution of product distribution can be as high as the thickness of a single paper layer (~180 μm). Third, after Ep separation, the paper can be cut to reclaim one or multiple components from a complex mixture for further analysis. Finally, the oPAD-Ep provides an alternative means for controlled and rapid transport of charged molecules through wetted paper when normal capillary driven flow is absent or too slow. The simple construction, low voltage requirement, and other properties alluded to above may make oPAD-Ep suitable for point-of-care (POC) applications, for example, as a component of diagnostic devices.

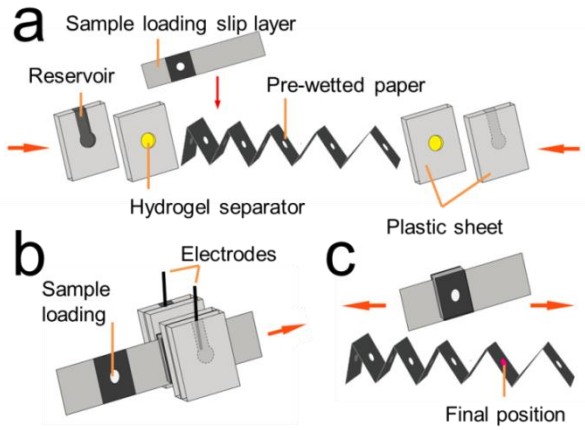

Illustration 2.1. *Scheme for the oPAD-Ep.*

In the 1930s, Tiselius developed the first Ep system, the Tiselius apparatus, for analysis of colloidal mixtures.[62] *This technique has evolved over time to take maximum advantage of physical and chemical differences*

between targets (usually proteins or DNA). For example, the supporting medium may be filter paper,[63] natural gels,[64-68] or synthetic gels,[69] and the apparatuses used to carry out these separations also vary widely (e.g., SDS-PAGE,[70,71] capillary Ep,[72] and isoelectric focusing[73,74]).

In recent years, simple forms of paper Ep have been developed that might eventually find their way into POC devices. For example, Ge et al. introduced a paper-based electrophoretic device for amino acid separation by imitating the design of conventional electrophoretic systems.[75] Using wax printing,[20] they patterned two reservoirs connected by a ~20 mm long channel on paper. A voltage of 330 V was applied across the channel, which achieved an electromigration speed of a few millimeters per minute for amino acids. Using an alternative design, Chen et al. achieved a similar electric field, but they avoided the necessary of using a high applied voltage by placing the anode and cathode in close proximity (~2 mm).[76] However, the device designs mentioned above involve either a high voltage, which is not suitable for POC applications, or challenging operational characteristics. Moreover, a constant pH was not maintained in either of these two devices, raising concerns about nonuniform Ep of amphoteric molecules, whose mobilities are strongly dependent on the

solution pH. The multilayer oPAD-Ep design we describe herein addresses these issues.

Three-dimentional (3D) PADs were first reported by Whitesides and co-workers in 2008.[19] In these devices, multiple paper layers were stacked and held together with double-sided tape. More recently, our group introduced a simpler method for achieving similar functionality by using the fabrication principles of origami, that is, folding a single piece of paper into a 3D geometry.[12] We call this family of sensors oPADs. Since their inception, a number of oPADs have been reported for various applications, including detection of biomolecules,[37,77,78] paper-based batteries,[76] and even a microscope.[79] In contrast to earlier systems, the oPADs-Ep takes advantage of the thinness of the paper used for device fabrication. This results in a very short distance between the anode and cathode, just a few millimeters, which leads to electric fields of ~2 kV/s with an input voltage of just 10 V. When subjected to this field, fluorescent molecules or proteins penetrate each paper layer at a speed of 1-3 layers/min. In this chapter, we discuss the fundamental characteristics of the oPADs-Ep design, demonstrate the separation of fluorescent molecules based on their different electrophoretic mobilities, and then show that bovine serum albumin (BSA) can be separated from calf serum within 5 min. We believe that these characteristics

are sufficiently desirable that the oPADs-Ep will eventually be incorporated into more sophisticated paper diagnostic devices when a separation step is required prior to analysis.

2.3 EXPERIMENTAL

2.3.1 Chemical and Materials

Tris-HCl buffer (1.0 M, pH = 8.0), phosphate buffered saline (PBS, pH = 7.4), and Whatman Grade 1 chromatography paper, were purchased from Fisher Scientific. Silver wire (2.0 mm in diameter), calf serum from formula-fed bovine calves, albumin (lyophilized powder, ≥ 95%, agarose gel Ep) and IgG (reagent grade, ≥ 95%, SDS-PAGE, essentially salt-free, lyophilized powder) from bovine serum, and FluoroProfile protein quantification kits were purchased from Sigma-Aldrich. The following fluorescent molecules were used as received: $Ru(bpy)_3Cl_2$ (Fluka), 4,4-difluoro-1,3,5,7,8-pentamethyl-4-bora-3a,4a-diaza-s-indacene ($BODIPY^{2-}$, Invitrogen), 8-methoxypyrene-1,3,6-trisulfonic acid trisodium salt ($MPTS^{3-}$, Anaspec), 1,3,6,8-pyrenetetrasulfonic acid tetrasodium salt (PTS^{4-}, Fisher Scientific), Rhodamine 6G (Acros), methylene blue (Sigma-Aldrich)and rhodamine B (Fluka). All solutions were prepared using deionized water having a resistivity of 18.2 MΩ•cm

from a Milli-Q Gradient System (Bedford, MA). Serum protein solutions were prepared with PBS.

2.3.2 Device Fabrication

oPAD-Eps were fabricated in three steps: (1) the slip layer and origami paper were patterned using wax printing,[20] (2) the plastic buffer reservoirs were fabricated using a laser cutter, and (3) the oPAD-Eps were assembled as shown in Illustration 2.1. Briefly, CorelDraw software was used to design wax patterns on the Whatman Grade 1 paper (the patterns used for the slip layers and origami sections are provided in the Illustration 2.2). After wax patterning using a Xerox 8570DN inkjet printer, the paper was placed in an oven at 120 ^{o}C for 45 s, and then cooled to 25 ± 2 ^{o}C. The unwaxed disk in the center of each section of the origami paper was ~3.5 mm in diameter.

As shown in Illustration 2.2, slip layers were partially laminated using Scotch self-sealing laminating pouches from 3M. There are two main reasons for this design. First and foremost, the plastic sheath reduces the friction between slip layer and wetted origami paper so that slipping does not cause serious damage to the paper. Second, it ensures alignment of the sample loading zone on the slip layer with the channel in the origami paper. Similarly, fabrication of buffer reservoirs begins with a design in

CorelDraw (Illustration 2.2). Each reservoir consists of three layers, which are aligned, stacked, and then bound by acrylic adhesive (Weld-On). Each layer was fabricated by cutting a clear 0.32 cm-thick acrylic sheet using an Epilog Zing 16 laser cutter (Epilog Laser, Golden, CO). The layer in direct contact with the origami paper has a 6.5 mm-diameter hole at its center, and this was filled with a 5.0% agar gel prepared with buffer solution. This gel serves as a separator between the origami paper and reservoir solution, and it prevents the paper from being damaged by long-term exposure to solution, undesirable pH changes, and the effects of pressure-driven flow. After all parts were fabricated, they were assembled into the final device (Illustration 2.1). Finally, the origami paper was pre-wetted with buffer solution, and the slip layer was placed in the desired position. The pressure holding the oPAD-Ep together is adjustable using four screws at the corners of the plastic sheets: finger-tight torque was found to be optimal.

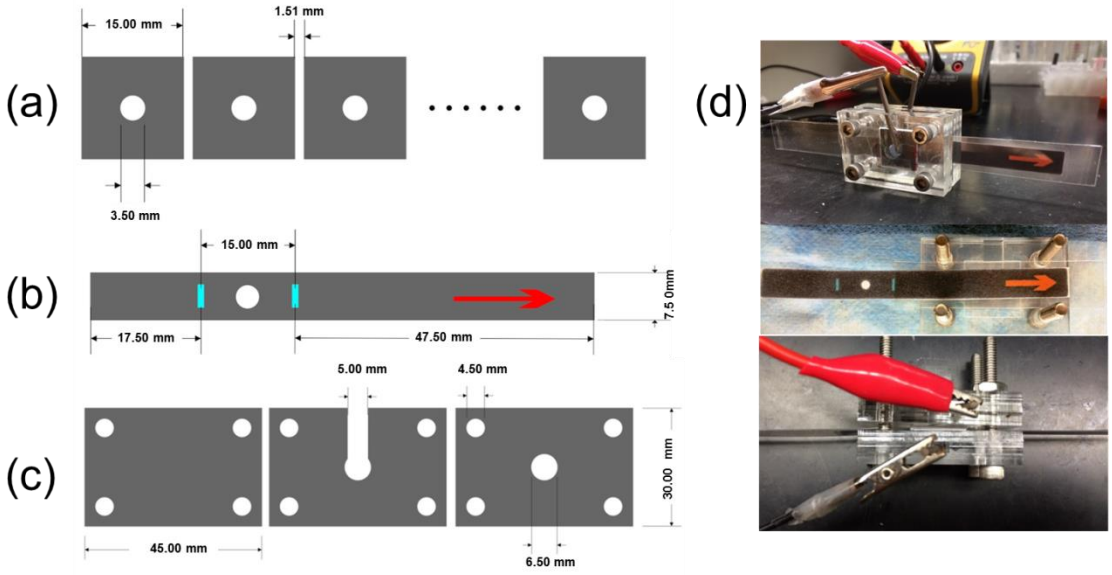

Illustration 2.2. *Designs of oPAD-Ep components. (a), (b), and (c) are the origami paper, slip layer, and plastic buffer reservoirs, respectively. (d) Photographs of the oPAD-Ep.*

2.3.3 Operation of the oPAD-Ep

Before use, the two reservoirs of the oPAD-Ep were filled with 300.0 μL of buffer and then a Ag/AgCl electrode was inserted into each of them. For fluorescent molecule Ep, 0.20 M Tris-HCl (pH = 8.0) was used, while PBS (pH = 7.4) was used for protein Ep. Ag/AgCl electrodes were prepared by immersing Ag wires in commercial bleach overnight,[80] and rinsed thoroughly with DI water before use. The surface of Ag wires turned dark brown after being oxidized to AgCl. A 0.50 μL aliquot of sample solution was loaded at the designated zone on the slip layer, and then introduced by pulling the slip layer into alignment with the origami

paper. A BK Precision DC regulated power supply (model 1621A) was used to apply a voltage between the two Ag/AgCl electrodes. After Ep, the buffer and electrodes were removed from the reservoirs, and the screws were loosened to unfold the origami paper for analysis.

2.3.4 Fluorescence Analysis

A Nikon AZ100 multi-purpose zoom fluorescence microscope was used to acquire fluorescent images of each oPAD-Ep layer, including the slip layer, and ImageJ software (NIH, Bethesda, MD) was used to analyze the fluorescence intensity. For protein analyses, we used the FluoroProfile protein quantification kit from Sigma-Aldrich to label proteins with a fluorescent tag.[12] Following Ep, 0.50 µL FluoroProfile fluorescent reagent solution was spotted onto the origami paper and slip layer, both of which were placed in a humidity chamber for 30.0 min and then taken out and dried for an additional 30.0 min in a dark room. During this time period, epicocconone in the stain solution fully reacts with primary amine groups on proteins, producing a fluorescent conjugate having two excitation maxima at ~400 and ~500 nm with emission at 610 nm.[81] An Omega XF204 filter (excitation: 540 nm and emission: 570-600 nm) was used to acquire the fluorescence images of stained proteins in the oPAD-Ep.

2.4 Results and Discussion

2.4.1 Electrophoresis of Individual Fluorescent Molecules.

In this section, we examine the Ep of single fluorescent molecules, and in the following sections we will show that oPAD-Eps are applicable to more complex tasks including separation of fluorescent molecules and proteins. The fluorescent molecules used for demonstration purposes are listed in Table 2.1, along with their excitation and emission wavelengths (fluorescence spectra are provided in the Figure 2.1) and the corresponding microscope filter sets used for analysis.

Fluorescent Molecules	Absorption Maximum Extinction (nm)	Fluorescence Maximum Emission (nm)	Excitation Filter (nm)	Emission Filter (nm)
$Ru(bpy)_3^{2+}$	455	622	420-490	510-700
$BODIPY^{2-}$	492	518	460-500	510-560
$MPTS^{3-}$	401	444	340-380	430-480
PTS^{4-}	374	384	340-380	430-480

Table 2.1: Spectral information about the fluorescence probes.

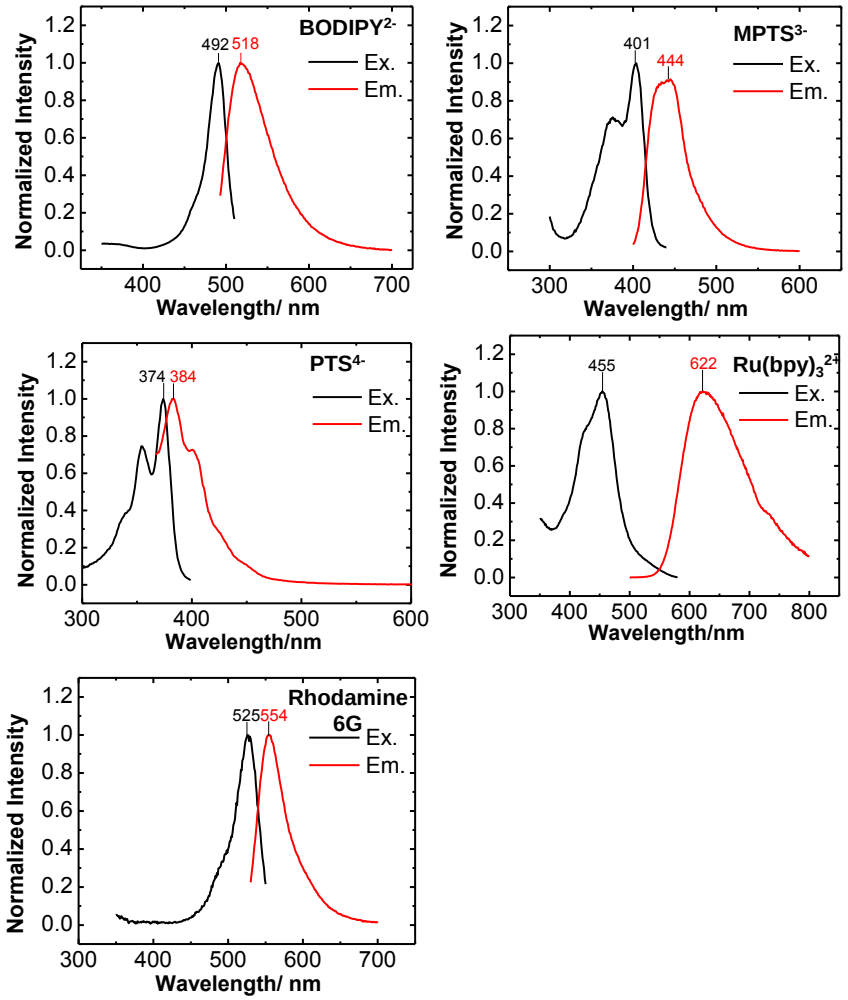

Figure 2.1. *Fluorescence spectra of $BODIPY^{2-}$, $MPTS^{3-}$. PTS^{4-}, $Ru(bpy)_3^{2+}$, and Rhodamine 6G.*

A detailed summary of the operation of the oPAD-Ep is provided in the Section 2.3.3. Briefly, however, the paper part of the device is folded, as shown in Illustration 2.1, and then compressed by plastic sheets. The two reservoirs are filled with buffer and a Ag/AgCl electrode is inserted into each of them. Next, an aliquot of sample solution is

loaded at the designated zone on the slip layer, and then it is introduced into the oPAD-Ep by pulling the slip layer into alignment with the origami paper. Finally, a voltage is applied to the electrodes until the separation is complete, as which time the origami paper is removed, unfolded, and analyzed.

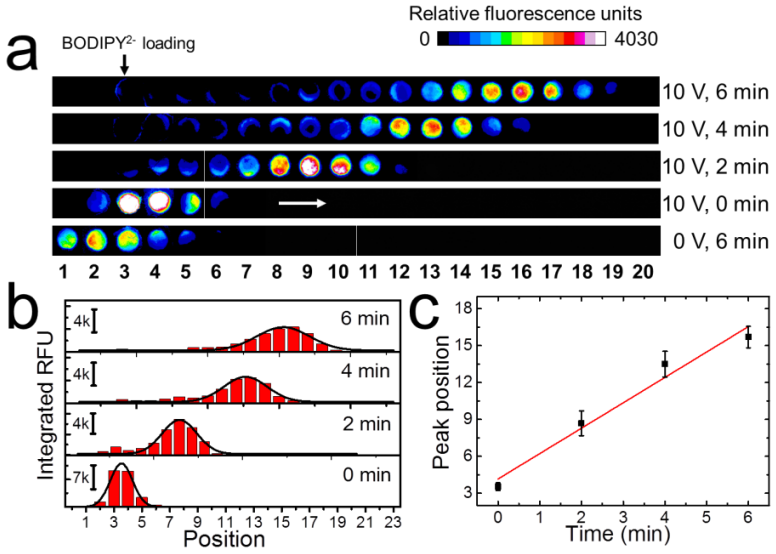

Figure 2.2. *Ep of $BODIPY^{2-}$ on oPAD-Ep.*
(a) Fluorescence micrographs of a 23-layer oPAD-Ep after Ep of $BODIPY^{2-}$ for run times ranging from 0 min to 6.0 min at 10.0 V and, in the bottom frame, after 6.0 min with no applied voltage. Fluorescence from just the first 20 layers is shown because the last three layers are at the background level. A 16-level color scale was used to differentiate the fluorescence intensities. $BODIPY^{2-}$ (0.50 µL, 1.0 mM) was initially spotted on the slip layer, which is located at Position 3. The white arrow in the fourth micrograph indicates the direction of $BODIPY^{2-}$ migration. (b) Integrated relative fluorescence unit (RFU) distributions, extracted from (a), as a function of Ep run time. The black line is a Gaussian fit to the histograms. (c) Peak positions derived from the Gaussian fittings in (b) as a function of time. The error bars represent the standard deviation of at least three independent tests at each time.

In the first series of experiments, a 23-layer paper device was used to study the migration of $BODIPY^{2-}$. This experiment was carried out by placing a 0.50 µL aliquot of 1.0 mM $BODIPY^{2-}$ onto the slip layer, which was in turn placed between the second and third layers of the oPAD-Ep, namely Position 3 in Figure 2.2. Upon application of 10.0 V, Figure 2.2 shows that $BODIPY^{2-}$ migrates from its initial location toward the cathode by penetrating each layer of the origami paper at a rate of ~2-3 layers per min. The results show that the distribution of $BODIPY^{2-}$ broadens as a function of separation time: the width of the band increases from ~2 layers at 0 min to ~5 layers at 6.0 min. In the absence of the electric field (bottom of Figure 2.2a), the initial $BODIPY^{2-}$ spot broadens by ~1 layer after 6.0 min. To demonstrate the importance of the origami construct, and particularly its modest thickness (~4 mm), we also carried out an Ep experiment in a 2.0 cm-long regular paper channel using the same applied voltage (details provided in the Figure 2.3) as a control. In this control experiment, the paper electrophoretic device comprises a ~2 cm-long straight paper channel with an electrode placed at each end. To rule out the interference of surface flow, the paper channel was embedded in a self-laminating pouch (blue part in Figure 2.3b). Sample was loaded at the midpoint of the buffer-wetted paper channel, and the applied voltage between the

two electrodes was varied from 4.0 V to 12.0 V to drive the electro-migration of $BODIPY^{2-}$. After 5.0 min, no Ep transport of the samples was observed under a UV lamp (Figure 2.3d) due to the weak electric field.

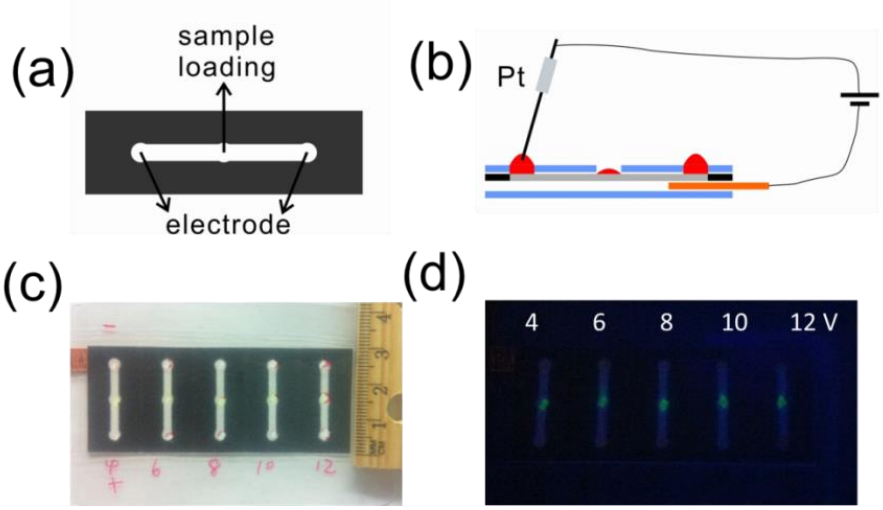

Figure 2.3. *Paper Ep control experiment. (a) Wax pattern of the device used in the control experiments: black, wax; white, paper. (b) Cross-sectional illustration of the device: orange, Cu cathode; blue, self-laminating pouch; grey, paper channel. (c) and (d) are photographs of the device in room light and under a UV lamp, respectively, after the application of the indicated voltages for 5.0 min.*

To provide a more quantitative analysis of the experiment in Figure 2.2, the fluorescence intensity (in terms of relative fluorescence units, RFU) of each layer of the oPAD-Ep was determined using ImageJ software and then plotted as a function of position in Figure 2.2b. The standard deviations (σ) and peak positions (μ_0) of the distribution were obtained by fitting the results to a Gaussian distribution. Assuming that diffusion is the major

cause of peak broadening, the diffusivity of BODIPY^{2-} in wet paper (D_{paper}) can be roughly estimated using the 1D Einstein diffusion equation (eq 2.1).

$$\Delta\sigma^2 = 2D_{paper}t \qquad (2.1)$$

Here, $\Delta\sigma^2$ is the mean square displacement at time t. A plot of $\Delta\sigma^2$ vs. t is provided in the Figure 2.4, and from its slope D_{paper} is calculated to be ~0.14 X 10^{-9} m^2/s, which is about one third of the diffusivity of BODIPY^{2-} in water (D_{water} = ~0.43 X 10^{-9} m^2/s).[82] This difference may be due to the presence of the network of cellulose fibers that hinders diffusion.[83] This suggests that the peak broadening exhibited by fluorescent molecules in the oPAD-Ep is mainly caused by stochastic motion. Two additional points should be mentioned. First, the initial peak broadening observed at 0 min is caused by the sample transfer from the slip layer to the two neighboring layers. Second, there is little or no capillary flow in the oPAD-Ep, because all layers of the paper are pre-wetted with the running buffer prior to application of the applied voltage.

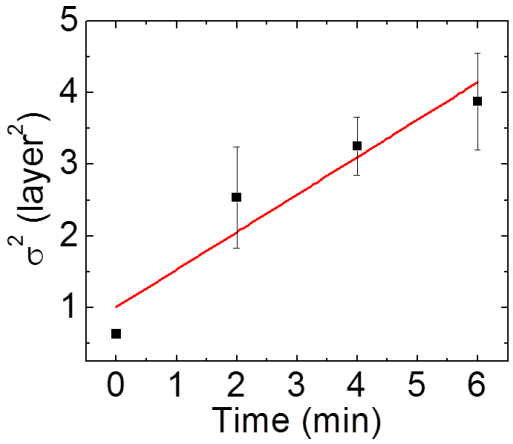

Figure 2.4. *σ^2 vs. time curve.*
The data were obtained from the Gaussian fits shown in Figure 2.2b.

Figure 2.2c shows that there is a linear correlation between the peak position (μ_0) and the time of Ep. The slope of this plot is 2.1 oPAD-Ep layers/min, which is equivalent to 6.0 μm/s. Using this value, it is possible to use eq 2.2 to estimate the Ep mobility (μ_{Ep}) of $BODIPY^{2-}$ in wetted paper (E is the local electric field inside the device). To do so, however, it is necessary to make the simplifying assumption that Ep dominates electroosmosis under the conditions used in our experiments.

It has been shown previously that the electroosmotic velocity of albumin in barbital buffer in a range of common papers ranges from ~30% to 170% of its Ep velocity at pH 8.8.[84] In addition, Posner and coworkers observed significant electroosmotic flow (EOF) in nitrocellulose paper during their paper-based isotachophoretic

preconcontration experiments. Specifically, they found that the fluorescent molecule AF488, which is focused between the leading and trailing electrolytes, moved faster (velocity increased from ~30 µm/s to 150 µm/s) after adding 3% polyvinylpyrrolidone (PVP) to the leading electrolyte to suppress the EOF.[85] Clearly, the EOF in paper varies over a wide range and is strongly dependent on experimental conditions such as paper structure and electrolyte. Therefore, we measured the electroosmotic velocity of Rhodamine B, which is neutral in the pH range between 6.0 and 10.8,[86] to evaluate the EOF in oPAD-Eps under our conditions (details provided in the Figure 2.5). The results show that the electroosmotic velocity is small (< 0.1 layer/min) compared to Ep, and therefore we ignore its contribution in the treatment that follows.

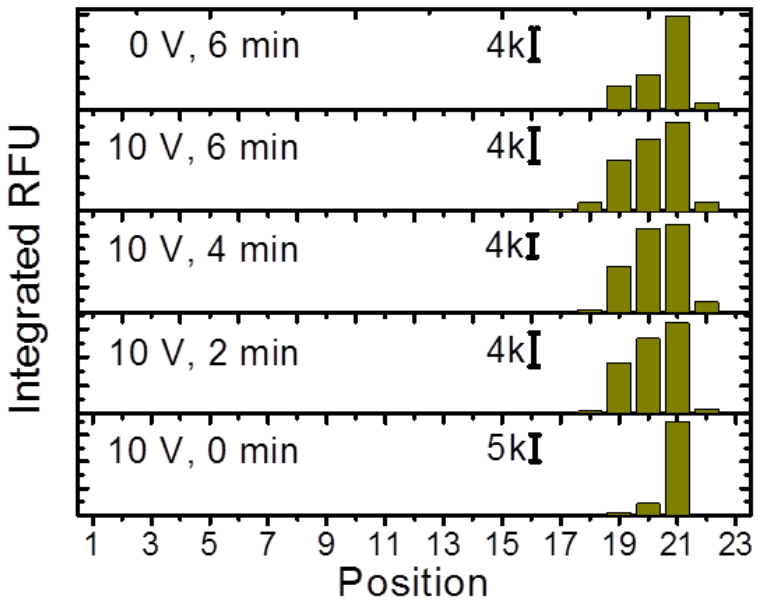

Figure 2.5. *Ep of Rhodamine B on a 23-layer oPAD-Ep. Rhodamine B (0.50 µL, 0.10 mM) was initially loaded onto the slip layer at Position 21, and the direction of applied electric field is from Position 23 toward Position 1. The running buffer was 0.20 M Tris-HCl (pH = 8.0).*

$$\mu_{Ep} = \frac{\Delta\mu_0}{E\Delta t} \qquad (2.2)$$

The following procedure was used to determine the value of E. A multimeter was connected in series with the power supply to measure the current flowing through the oPAD-Ep with and without origami paper present in the device. At an applied voltage of 10.0 V, the values of the two currents were ~1.7 mA and 6.0 mA, respectively. Using the difference between these currents and Ohm`s law, the calculated resistance of the origami paper is ~4.2 kΩ. By multiplying this resistance by the current at 10.0 V, the voltage drop

(ΔV) across the paper is determined to be ~7 V. The value of E in the oPAD-Ep (~1.7 kV/m at an applied voltage of 10.0 V) is then calculated by dividing ΔV by the total thickness (d = 4.1 mm) of the 23-layer origami paper. Finally, using eq 2.2, μ_{Ep} for $BODIPY^{2-}$ in the oPAD-Ep is calculated to be ~2.2 X 10^{-9} $m^2/(s \cdot V)$.

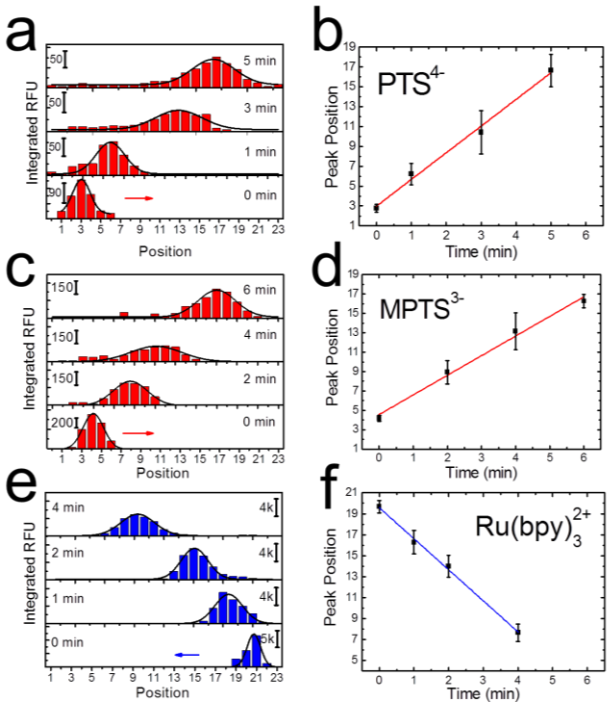

Figure 2.6. *Ep of PTS^{4-}, $MPTS^{3-}$ and $Ru(bpy)_3^{2+}$ on 23-layer oPAD-Eps.*
Applied voltage is 10.0 V. PTS^{4-} or $MPTS^{3-}$ (0.50 µL, 5.0 mM) were initially pipetted onto the slip layer which is located at Position 3. Due to the positive charge of $Ru(bpy)_3^{2+}$, its slip layer is at Position 21. (a), (c), and (e) show the integrated RFU distributions of these molecules in oPAD-Eps as a function of Ep run time. The black lines are Gaussian fits of the histograms. (b), (d), and (f) are the peak positions derived from the Gaussian fits in (a), (c), and (e) as a function of time.

Following the procedure described for $BODIPY^{2-}$, we evaluated the Ep properties of three other dyes in the oPAD-Ep: PTS^{4-}, $MPTS^{3-}$, and $Ru(bpy)_3^{2+}$. Plots of the position of these dyes as a function of time are shown in Figure 2.6. From these data, the Ep velocities were determined to be: PTS^{4-}, 2.7 layers/min; $MPTS^{3-}$, 2.0 layers/min; and $Ru(bpy)_3^{2+}$, 3.0 layers/min. The corresponding values of μ_{Ep} are 2.9 X 10^{-9} $m^2/(s \cdot V)$, 2.1 X 10^{-9} $m^2/(s \cdot V)$, and 3.2 X 10^{-9} $m^2/(s \cdot V)$, respectively. These mobilities are about one order of magnitude smaller than their counterparts in bulk solution.[87,88] There are several possible reasons for this: hindered migration by the cellulose matrix, specific interactions between the charged molecules and the paper, and small contributions arising from electroosmosis (the direction of EOF is opposite to the migrational direction of negatively charged dyes). Regardless of the underlying phenomena, the relative velocities are: $Ru(bpy)_3^{2+}$ > PTS^{4-} > $MPTS^{3-}$ ~ $BODPIY^{2-}$. Two other positively charged dyes, the characteristics of Rhodamine 6G (+1 charge between pH 4.0 and 10.0; see Figure 2.7)[89] and methylene blue were also tested, and both were found to migrate slowly (< 0.2 layer/min) under the same conditions used for the other dyes. This may be a consequence of a strong electrostatic interaction between the negatively charged paper and the

positively charged dyes, but why $Ru(bpy)_3^{2+}$ is an exception is still a mystery.

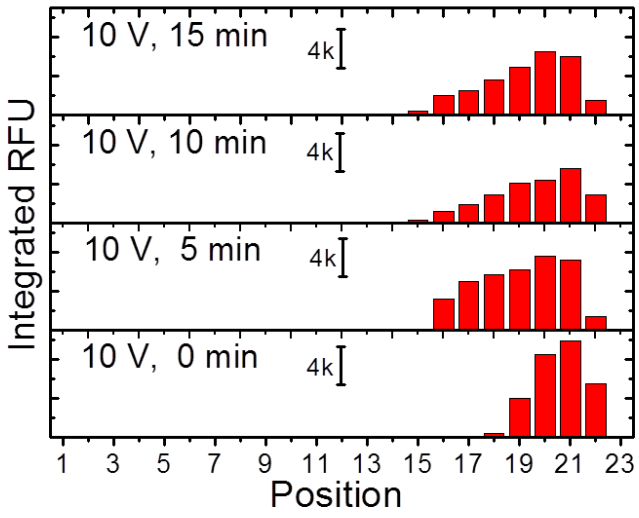

Figure 2.7. *Ep of Rhodamine 6G on a 23-layer oPAD-Ep. Rhodamine 6G (0.50 µL, 0.10 mM) was initially loaded at Position 21 and the direction of the applied electric field (10.0 V) is from Position 23 to 1.*

2.4.2 Simultaneous Separation of Multiple Fluorescent Molecules

In this section, two examples are presented that demonstrate separation of fluorescent molecules using the oPAD-Ep. The first utilizes a mixture of two oppositely charged molecules: $MPTS^{3-}$ and $Ru(bpy)_3^{2+}$, which migrate in opposite directions upon the application of an electric field. The second example demonstrates separation of $BODIPY^{2-}$ and PTS^{4-}, which have the same charge but μ_{Ep} values that differ by about 25%.

The separation of $MPTS^{3-}$ and $Ru(bpy)_3^{2+}$ was carried out as follows. A mixture containing 1.5 mM $MPTS^{3-}$ and 1.5 mM $Ru(bpy)_3^{2+}$ was prepared by mixing equal aliquots of 3.0 mM $MPTS^{3-}$ and 3.0 mM $Ru(bpy)_3^{2+}$, spotting 0.50 µL of the mixture onto the slip layer, and inserting the slip layer at Position 11 of the oPAD-Ep. All other conditions were the same as in the previously described single-analyte experiments. When 10.0 V was applied between the two Ag/AgCl driving electrodes, $MPTS^{3-}$ moved from its initial position towards the anode and $Ru(bpy)_3^{2+}$ migrated toward the cathode. After carrying out the separation, each layer of the oPAD-Ep was characterized spectroscopically using a different fluorescence filter (Table 2.1). Because the emission intensity is different for the two dyes, the results of this experiment, shown in Figure 2.8a, are normalized by setting the maximum RFU to 1. The key finding is that a near-quantitative separation is achieved in < 1 min. Figure 2.8b shows fluorescence images for the individual dyes (in the same oPAD-Ep) 3 min after the application of the voltage. Using the peak positions in Figure 2.8b, the electrophoretic velocities are ~2 and ~3 layers/min for $MPTS^{3-}$ and $Ru(bpy)_3^{2+}$, respectively. These values are the same as those measured for the individual dyes.

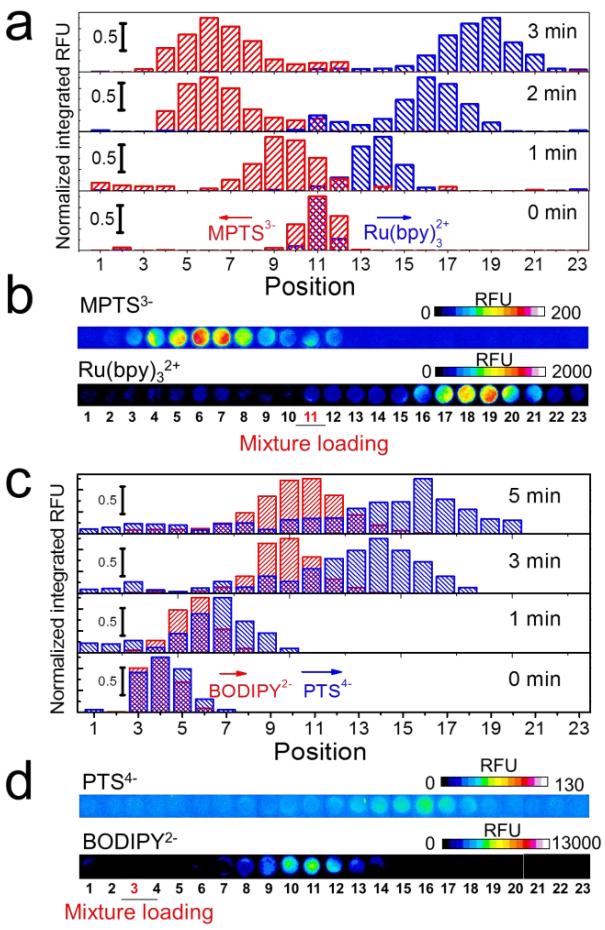

Figure 2.8. *Separation on oPAD-Eps. (a) Separation of a mixture of 1.5 mM $MPTS^{3-}$ and 1.5 mM $Ru(bpy)_3^{2+}$ using a 23-layer oPAD-Ep and an applied voltage of 10.0 V. A 0.50 µL aliquot of this mixture was initially spotted on the slip layer located at Position 11. The two arrows in the fourth histogram indicate the directions of $MPTS^{3-}$ and $Ru(bpy)_3^{2+}$ migration. The blue and red histograms correspond to the distributions of $Ru(bpy)_3^{2+}$ and $MPTS^{3-}$, respectively. (b) Fluorescence micrographs of $MPTS^{3-}$ and $Ru(bpy)_3^{2+}$ in the same oPAD-Ep as in (a) after a 3.0 min separation using an applied voltage of 10.0 V. (c) Similar experiment as in (a), but for a mixture of 1.5 mM PTS^{4-} and 0.50 mM $BODIPY^{2-}$. (d) Fluorescence micrographs of PTS^{4-} and $BODIPY^{2-}$ in the same oPAD-Ep as in (c) after 5.0 min Ep at an applied voltage of 10.0 V. Filter sets used to acquire the data are given in Table 2.1.*

The second demonstration of the oPAD-Ep involves the separation of two negatively charged dyes. In this case, a 0.50 µL aliquot of a mixture containing 1.5 mM PTS^{4-} and 0.50 mM $BODIPY^{2-}$ was initially situated at Position 3 (Figures 2.8c and 2.8d). Upon application of 10.0 V, both molecules are driven toward the anode and gradually separate (Figure 2.8c). The calculated Ep velocities of $BODIPY^{2-}$ and PTS^{4-} (Figures 2.2 and 2.6, respectively) are 2.1 and 2.7 layers/min. From these values, the predicted peak separation should be ~3-4 paper layers after 5.0 min, which is in good agreement with the value of ~5 layers found in the experiment (Figures 2.8c and 2.8d). Figure 2.8d shows fluorescence micrographs of $BODIPY^{2-}$ and PTS^{4-} obtained in the same oPAD-Ep. The relatively low fluorescence intensity for PTS^{4-} in these experiments is caused by the small Stokes shift of this molecule which does not match perfectly with the fluorescence filter set used (Table 2.1 and the Figure 2.1).

2.4.3 Electrophoresis of Serum Proteins

Ep is widely used to separate biomolecules such as DNA and proteins. One of the most common electrophoretic techniques is gel Ep, which uses a gel to suppress the thermal convection caused by Joule heating and to sieve biomolecules on the basis of their size. This method is

routinely used in clinical laboratories to test for abnormalities in a variety of biological matrices, including: serum, urine, blood, and cerebrospinal fluid.[90] *For example, in serum protein gel Ep, normal serum is separated into five different bands: (1) Albumin, which is approximately two-thirds of the total protein content (3-5 g/dL); (2) Alpha-1(0.1-0.3 g/dL) and (3) Alpha-2 (0.60-1.0 g/dL), which are two groups of globulins mainly including heptoglobin, ceruloplasmin, and macroglobin; (4) Beta (0.7-1.2 g/dL), composed of transferrin and lipoprotein; and (5) Gama (0.6-1.6 g/dL), which contains primarily immunogolublins such as IgG.*[91] *An excess or insufficiency in any of these bands may indicate a need for medical attention. Commercially available devices for separating serum proteins usually require a high voltage (200-300 V) and a long separation time (~1 h), both of which are impractical for POC applications. In this section, we will show that the oPAD-Ep is able to rapidly (5 min) separate serum proteins using a voltage of just 10 V.*

The Ep properties of bovine serum albumin (BSA) and IgG (also from bovine serum) were initially evaluated separately in the oPAD-Ep. In these experiments, an 11-layer oPAD-Ep was first wetted with 1 PBS buffer (ionic strength 163 mM, pH = 7.4). Next, 0.50 µL of a 0.1 PBS buffer (ionic strength 16.3 mM) containing either 5.0 g/dL BSA or 1.0 g/dL

IgG was loaded at Position 3 of the oPAD-Ep. These conditions are different from those used for separating the fluorescent molecules: the oPAD-Ep consists of fewer layers (this experimental design flexibility is a noteworthy characteristic of the oPAD-Ep) and the buffer concentration is lower, both of which serve to increase the electric field within the device.

Figure 2.9a shows fluorescence micrographs of BSA in the oPAD-Ep before and after the application of 10.0 V for 5.0 min, and after 5.0 min in the absence of an electric field. When no voltage is applied, BSA undergoes random diffusion, spreading out by ~1 layer from the initial position within 5.0 min. In contrast, when 10.0 V is applied, BSA migrates towards the cathode at a speed of ~1 layer/min (equal to a mobility of ~5 10^{-10} $m^2/(s \cdot V)$, details provided in the Figure 2.10). The mobility of BSA measured in the oPAD-Ep is an order of magnitude lower than the value reported in the literature using conventional paper Ep.[84] In the previously reported experiments, however, Ep was carried out for 14 h (150 times longer than in our experiments) to achieve a reasonable separation of serum proteins. This long immersion time causes deterioration of the paper structure, which may lead to faster migration of BSA. This contention is supported by the small difference (< 8%) between the measured mobility of BSA in paper and in

free solution noted in this prior report.[84] In addition, the type of paper and the pH used in our study is different, and the effects of electroosmosis were not considered in our calculation. After migration, remnants of BSA were observed on the paper (Positions 6-9, Figures 2.9a and 2.9b), which is expected as BSA is known as a nonspecific adsorption blocker in paper based devices.[77]

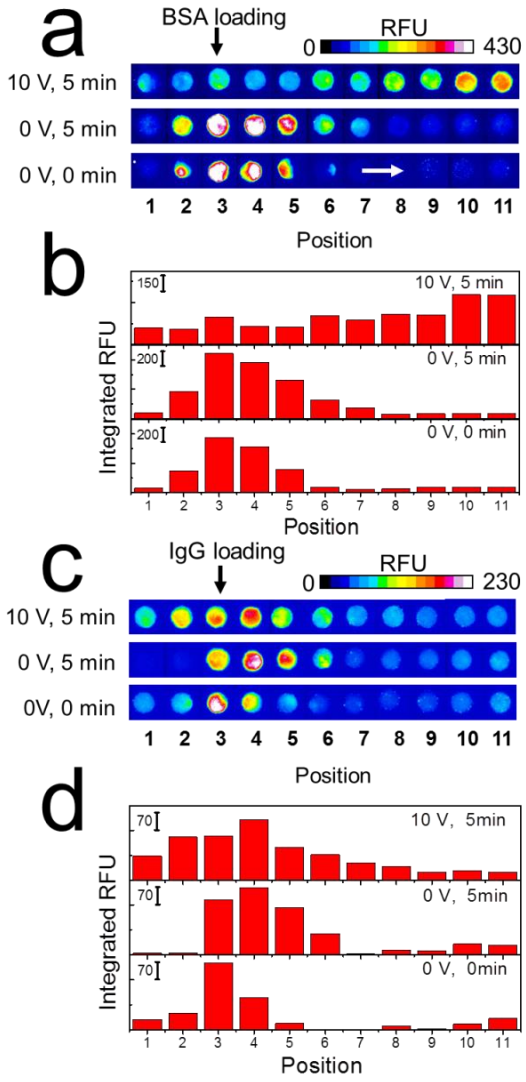

Figure 2.9. *Ep of BSA and IgG on 11-layer oPAD-Eps. Both BSA and IgG were stained with epicocconone to produce fluorescent conjugates (details provided in the Section 2.3.4). (a) Fluorescence micrographs of the oPAD-Ep after Ep of BSA for 5.0 min at 10.0 V and, in the second and third frames, after 5.0 min and at 0 min with no applied voltage. BSA (0.50 µL, 5.0 g/dL prepared in 0.1 PBS (ionic strength: 16.3 mM, pH = 7.4)) was initially loaded on the slip layer which is at Position 3. The same procedure was used for a 1.0 g/dL bovine IgG solution, and the fluorescence micrographs are shown in (c). (b) and (d) are the corresponding histograms of integrated RFU extracted from (a) and (c), respectively.*

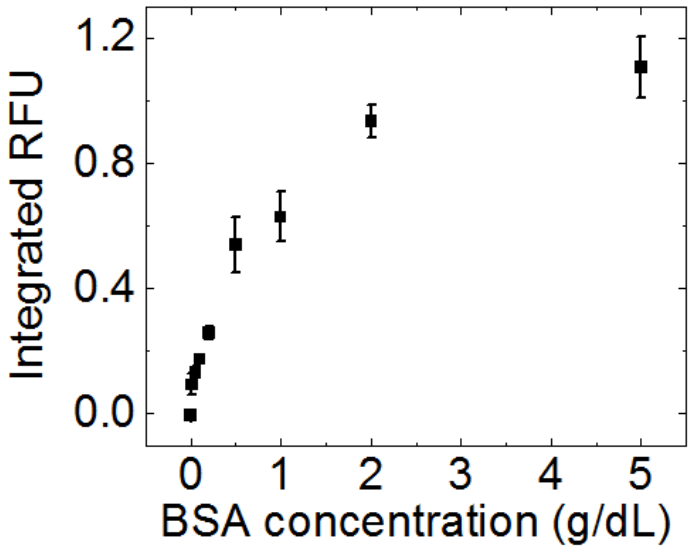

Figure 2.10. *BSA calibration curve.*
Paper zones with a diameter of 3.5 mm were used to obtain the BSA calibration curve. These paper zones were first wetted with 0.50 µL 0.1 PBS solution (ionic strength 16.3 mM), and then 0.50 µL of BSA solutions having different concentrations was spotted at the wet paper zone, followed by another 0.50 µL epicocconone to stain the protein. After that, the devices were kept in a humidity chamber for 30.0 min to allow epicocconone to fully react with BSA, and then moved to a dark room until they were dry (~30 min). After taking fluorescence micrographs, the RFU of each paper zone was integrated in ImageJ and plotted as a function of BSA concentration. Integrated RFU of stained BSA in 3.5-mm-diameter paper zones as a function of BSA concentration. Estimation of BSA mobility. At 10.0 V, the migrational velocity of BSA on wet paper is ~1 layer/min or 3 µm/s. The electric field is simply estimated as 10.0 V divided by the thickness of 10-layer origami paper which is ~1.8 mm, giving a value of ~5.5 kV/m. After that, using eq 2.2 in the main text, the mobility of BSA is calculated to be ~5 X 10^{-10} $m^2/(s \cdot V)$.

In contrast to BSA, the distribution of IgG shifted only slightly toward the anode after 5.0 min, as shown in Figures 2.9c and 2.9d. This is primarily because IgG has a different isoelectric point than BSA: 7.3 ± 1.0,[92] and 4.9 ± 0.1,[93,94] respectively (recall that the separation is carried out at pH 7.4). Additionally, IgG is a larger molecule (~150 kDa) than BSA (~66.5 kDa),[95] which also leads to a lower mobility.

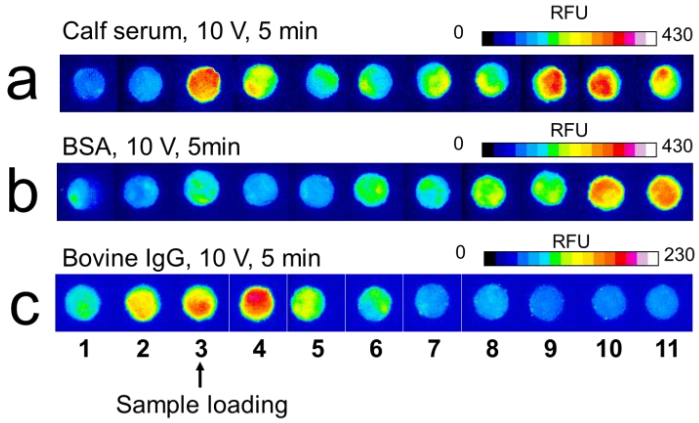

Figure 2.11. *Separation of calf serum on 11-layer oPAD-Eps. Applied voltage is 10.0 V. (a) Fluorescence micrographs obtained after Ep of calf serum at 10.0 V for 5.0 min. A 0.50 µL aliquot of serum was initially spotted onto the slip layer at Position 3. (b) and (c) are fluorescence micrographs of oPAD-Eps used for single-component control experiments: 5.0 g/dL BSA and 1.0 g/dL bovine IgG. Separation conditions were the same for all the data in this figure.*

Applying the same conditions used for the control experiments illustrated in Figure 2.9, we carried out a separation of the components of calf bovine serum. Figure 2.11a is a fluorescence micrograph of an oPAD-Ep after

separation of a 0.50 µL bovine serum sample for 5.0 min at 10.0 V. Two fluorescence maxima are apparent: one near the starting location of the separation (Position 3), which belongs to immunoglobulin proteins (including IgG), and the other near Positions 9-10, corresponding to BSA. By simple visual comparison with the fluorescence intensities of the control experiments shown in Figure 2.9, it is possible to obtain a quick semi-quantitative analysis. The total amount of BSA in the calf serum (Figure 2.11a) is close to that of the BSA control of 5.0 g/dL (Figure 2.11b), which lies in the normal range of 3-5 g/dL.[91] Comparison of Figures 2.11a and 2.11c reveal that the immunoglobulin protein concentration is higher than 1.0 g/dL IgG, but still in a reasonable range considering that immunoglobulin proteins other than IgG are also present in the serum sample. A more quantitative analysis is not possible, because the fluorescence intensity of protein starts to deviate from linearity at concentrations >~0.50 g/dL (a calibration curve is given in the Figure 2.10). Also, the other three weak bands, Alpha-1, Alpha-2 and Beta, which usually appear between the immunoglobulin proteins and albumin in conventional serum Ep, cannot be distinguished by the oPAD-Ep. This may be because of the strong background of non-specifically absorbed BSA.

2.5 Summary and Conclusions

In this chapter, we have described an innovative design for a low-cost separation system based on folded paper. This approach takes advantage of the thinness of origami paper (180 µm/layer) to achieve a high electric field strength (several kV/m) at a low applied voltage (~10 V). The voltage required for the oPAD-Ep is more than an order of magnitude lower than that used in conventional electrophoretic devices. The simple construction, low voltage requirement, and ease of use make the oPAD-Ep a good candidate for POC applications. Moreover, because it is able to separate fluorescent molecules and serum proteins within ~5 min, it can potentially be integrated into other types of paper-based devices for preseparation of, for example, blood components.

*Chapter 3: Low-Voltage Paper Isotachophoresis Device for DNA Focusing**

3.1 Synopsis

We present a new paper-based isotachophoresis (ITP) device design for focusing DNA samples having lengths ranging from 23 to at least 1517 bp. DNA is concentrated by more than two orders of magnitude within 4 min. The key component of this device is a 2 mm-long, 2 mm-wide circular paper channel formed by concertina folding a paper strip and aligning the circular paper zones on each layer. Due to the short channel length, a high electric field of ~16 kV/m is easily generated in the paper channel using two 9 V batteries. The multilayer architecture also enables convenient reclamation and analysis of the sample after ITP focusing by simply opening the origami paper and cutting out the desired layers. We profiled the electric field in the origami paper channel during ITP experiments using a nonfocusing fluorescent tracer. The result showed that focusing relies on formation and subsequent movement of a sharp electric field boundary between the leading and trailing electrolyte.

---

* *Chapter 3 is based on previous publication: X. Li, L. Luo and R. M. Crooks, Low-voltage paper isotachophoresis device for DNA focusing, Lab Chip, 2015, 15, 4090-4098. XL and LL contributed equally to the work. RMC was the research advisor. XL and LL designed and performed the experiments. XL, LL, and RMC wrote the manuscript.*

3.2 Introduction

Here we report a paper isotachophoresis (ITP)[96] platform fabricated using the principles of origami (Japanese paper folding). The device is very inexpensive, easy to assemble and operate, and is able to electrokinetically concentrate DNA. The design of this origami paper analytical device (oPAD)[12,97] is illustrated in Illustration 3.1. Briefly, a piece of wax-patterned paper[20] is folded into a concertina configuration, a plastic slip layer[43,98,99] is inserted into one of the folds, and then this assembly is sandwiched between reservoirs for the trailing electrolyte (TE) and leading electrolyte (LE). DNA, present at concentrations on the order of 10^{-9} M, is initially mixed with the TE solution and then added to the TE reservoir, followed by addition of the LE solution to its reservoir. These solutions flow spontaneously into the paper channel but are prevented from mixing by the slip layer. Next, a voltage bias is applied between electrodes in the reservoirs, and then the slip layer is removed. This results in accumulation of DNA (100-fold concentration amplification) at the interface of the two electrolytes within ~4 min.

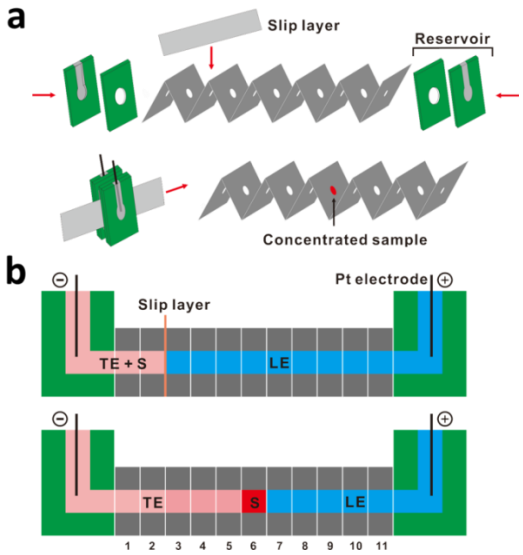

Illustration 3.1. *Scheme of the oPAD-ITP.*

Four important outcomes emerge from the experiments reported here. First, the power requirements of the oPAD-ITP are supplied by two 9 V batteries, which is a >20-fold lower voltage than previously reported, and therefore true point-of-care (POC) applications are accessible and complications due to Joule heating are minimized.[85,100,101] *Second, the origami paper channel is fully enclosed by wax, and therefore solvent (water) evaporation is minimized. Third, the plastic slip layer (Illustration 3.1) makes it very easy to establish a well-defined initial TE/LE boundary. Fourth, the oPAD-ITP is "digital" in the sense that the enriched product will be on individual paper layers and can be reclaimed by simply cutting off the desired layer(s). This opens up the possibility of coupling the oPAD-ITP with other*

detection systems to achieve lower limits of detection (LOD).

Our work builds on the original reports of two-[18] and three-dimensional[19] PADs introduced by the Whitesides group in 2007 and 2008, respectively. Due to their biocompatibility,[3] ease of fabrication,[20] and low-cost,[3,102] PADs provide a natural entry into the field of POC diagnostic devices and systems.[8] A number of detection methods have been developed for PADs, including: electrochemistry,[54,57,77] photography,[103,104] luminescence,[75,105-107] and others.[10,108] Nevertheless, it is still difficult to achieve sufficiently low LODs for some important applications, particularly those involving nucleic acid detection. One way around this problem is sample preconcentration, and although there are many ways to approach this for bulk solutions the number that have been reported for paper platforms is very limited.[10]

Isotachophoresis (ITP) is an electrophoretic technique that can effectively concentrate ionic samples with minimal sample pretreatment.[96,109,110] In a typical ITP experiment, the electric field profile across an electrophoretic channel is controlled by using electrolytes having different mobilities: a fast moving LE and a slow moving TE.[111] When a voltage is applied across the channel, sample ions, initially present in the TE solution, out-pace the TE and

accumulate at the TE/LE boundary resulting in a high local concentration. The ITP technique for nucleic acids[109] and proteins[112] is well-established for capillaries[113] and microfluidic devices.[114,115] For example, Bercovici et al. demonstrated that ITP in capillary can enable >10,000-fold increase in hybridization rates of nucleic acid.[116] Garcia-Schwarz and Santiago developed a microfluidic chip-based two-stage ITP assay to detect microRNA targets from only a few nanogram total RNA.[117]

In contrast to traditional fluidic platforms, there are only a few examples of ITP being implemented on PADs. For example, Moghadam et al. used a paper-based device for ITP focusing of the dye Alexa Fluor 488. The specific platform in this case was nitrocellulose paper strips, and they were able to demonstrate 900-fold enrichment using an applied voltage in the 250-350 V range.[85] Later, the same group integrated lateral flow immunoassays (LFA) into their paper-based ITP device demonstrated an LOD improvement of two orders of magnitude.[101] Rosenfeld and Bercovici developed an ITP microfluidic device made of wax-patterned filter paper and transparent tape. Their device enabled 1,000-fold enrichment of a fluorescent tracer using an applied voltage of ~400 V.[100]

Our group recently reported an oPAD design for electrophoretic separations that is intended to be simpler

and operate at much lower voltages than those that have been reported previously.[97] In the present chapter, we adapted this design for ITP, and specifically for ITP concentration of DNA. We report on four specific experiments. First, we discuss ITP of 23-mer single-stranded DNA labeled with Cyanine5 (ssDNA) using the oPAD-ITP and compare this result to a mathematical model reported by Rosenfeld and Bercovici.[100] Second, we show how ITP enrichment is affected by the initial concentration of sample DNA. Third, we report on some fundamental principles of the oPAD-ITP, and in particular the electric field profile during sample focusing. Finally, we demonstrate a specific application of the oPAD-ITP: ITP of a 100 bp dsDNA ladder, which is comprised of 100-1517 bp of double-stranded DNA (dsDNA). The results of these studies suggest that the oPAD-ITP will be able to provide additional functionality for a variety of paper-based detection platforms.

3.3 EXPERIMENTAL

3.3.1 Chemicals and Materials

Whatman Grade 1 cellulose paper, HCl, acetic acid, and agarose were purchased from Fisher Scientific (Walthman, MA). Single-stranded DNA (ssDNA, 5`-AGT CAG TGT GGA AAA TCT CTA GC-Cy5-3`) was ordered from Integrated DNA Technologies

(Coralville, IA) and purified by HPLC. The 100 bp dsDNA ladder was from New England BioLabs (Ipswich, MA). The following chemicals were from Sigma-Aldrich (St. Louis, MO) and used as received: 2-amino-2-(hydroxymethyl)-1,3-propanediol (tris base), 2-aminoethanesulfonic acid (taurine), $Ru(bpy)_3Cl_2$, ethidium bromide (EtBr) solution (10 mg/mL), and EDTA.

3.3.2 Device Fabrication

The fabrication of the oPAD-ITP is similar to that of a related electrophoretic device we have reported previously,[97] but there are some important differences. Whatman grade 1 cellulose paper (~180 µm thick) was patterned with wax (CorelDRAW designs shown in Illustration 3.2) using a Xerox ColorQube 8750DN inkjet printer. The key feature of the patterning is the presence of a ~2 mm-diameter wax-free region in the center of each section of the device. The patterned paper was placed in an oven at 120 °C for 45 s to allow the wax to penetrate through the thickness of paper[20] and then cooled to 25 ± 2 °C. After folding the paper into an 11-layer origami structure (Illustration 3.1), a piece of plastic sheet (photo laminating sheets from 3M: 0.5 mm thick, 4.0 cm long, and 1.0 cm in wide) was inserted between the second and third layers. This slip layer is used to form the initial TE/LE

boundary and also serves as a switch to initiate the ITP process. The TE and LE reservoirs were fabricated from acrylonitrile butadiene styrene (Illustration 3.2b) using a Flashforge Pro XL 3D printer. The assembled oPAD-ITP was then sandwiched between the two reservoirs. The degree of compression of the concertina fold was controlled using four screws situated at the corners of the reservoirs (Illustration 3.2c).

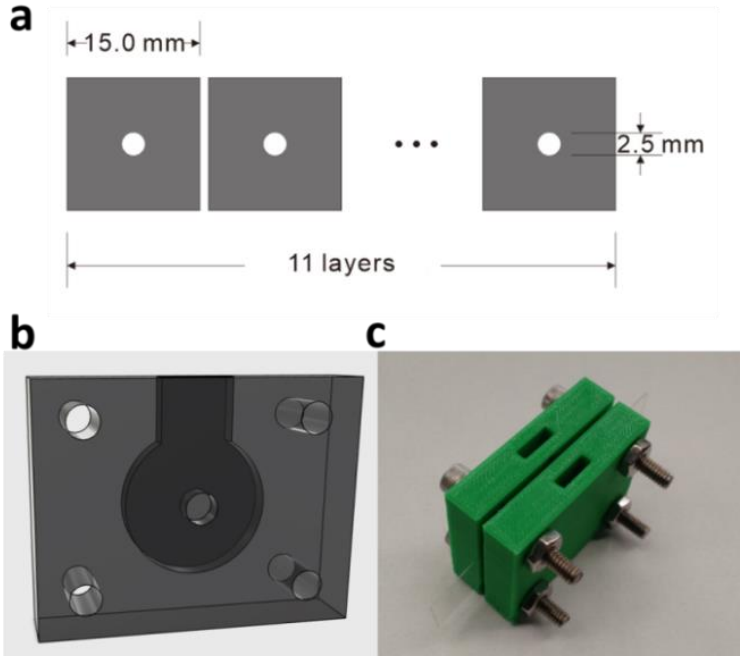

Illustration 3.2. *Design and photographs of the oPAD-ITP. (a) A CorelDRAW drawing of the origami paper device. The white parts represent unmodified paper and the gray areas are impregnated with wax. (b) A drawing (Autodesk 123D Design) of the 3D-printed reservoirs. (c) A photograph of an actual device. The origami paper is sandwiched between the two green reservoirs using four screws at the corners. Electrodes are inserted into the top holes on the reservoirs.*

3.3.3 Device Operation

The TE and LE solutions used in these experiments were 2.0 mM tris-taurine (pH 8.7) and 1.0 M tris-HCl (pH 7.3), respectively. After assembling the oPAD-ITP (origami paper, slip layer and reservoirs), the reservoirs were filled with 1.0 mL of the TE or LE buffer as shown in Illustration 3.1. The circular paper channel was completely wetted within 1 min. A Pt wire was inserted into each reservoir, and then two 9 V batteries were connected in series and used as the power supply (18 V in total).

For the ssDNA concentration experiments, 40.0 nM of the ssDNA was initially present in the TE solution. For the dsDNA ladder experiments, 0.50 µg/mL of the dsDNA ladder was initially mixed in the TE solution. In the electric field profiling experiment, 30.0 µM $Ru(bpy)_3^{2+}$ was initially mixed in the LE solution. For these latter experiments, home-made Ag/AgCl electrodes,[80] rather than Pt, were used to avoid generation Cl_2 arising from the low resistance and high current level (~17 mA). After ITP experiments, the solutions in both reservoirs were removed and the device was disassembled to analyze the content of each paper layer.

3.3.4 Fluorescence Microscopic Analysis

A Nikon AZ100 multi-purpose zoom fluorescence microscope with Nikon filters (ssDNA: 590-650 nm excitation and 663-738 nm emission; $Ru(bpy)_3^{2+}$: 420-490 nm excitation

and 510-700 nm emission) was used to acquire fluorescence images of each fold of the oPAD-ITP device. All images were then processed with ImageJ software to obtain integrated relative fluorescence unit (RFU) intensity for quantification of fluorescent molecules on each layer.

3.3.5 Gel Electrophoresis analysis

Gel electrophoresis was used to quantify the dsDNA content on each paper layer after ITP of the dsDNA ladder. Gel electrophoresis was chosen for two reasons. First, most common dsDNA stains, such as SYBR gold or EtBr, exhibit a high background on cellulose paper, and this makes it difficult to visualize and quantify the amount of dsDNA. Second, the dsDNA ladder is comprised of twelve dsDNA components having lengths ranging from 100 to 1517 bp. Gel electrophoresis can separate them and provides quantitative information for each component of the ladder.

The gel electrophoresis analyses were conducted as follows. First, each fold of the paper was cut off, dried, and then inserted into a 1.3% agarose gel containing 10 µg/mL EtBr (Illustration 3.3). Control samples were prepared by drying 1.0 µL of the 500 µg/mL dsDNA ladder stock solution in the paper zone. Gel electrophoresis was run using 1x TAE (containing 40.0 mM tris, 20.0 mM acetic acid, and 1.0 mM EDTA) buffer for 50 min at 100 V (Lambda LLS9120

DC Power Supply). A Typhoon Trio fluorescence scanner (GE Healthcare, Piscataway, NJ) was used to image the gel, followed by ImageJ software analysis.

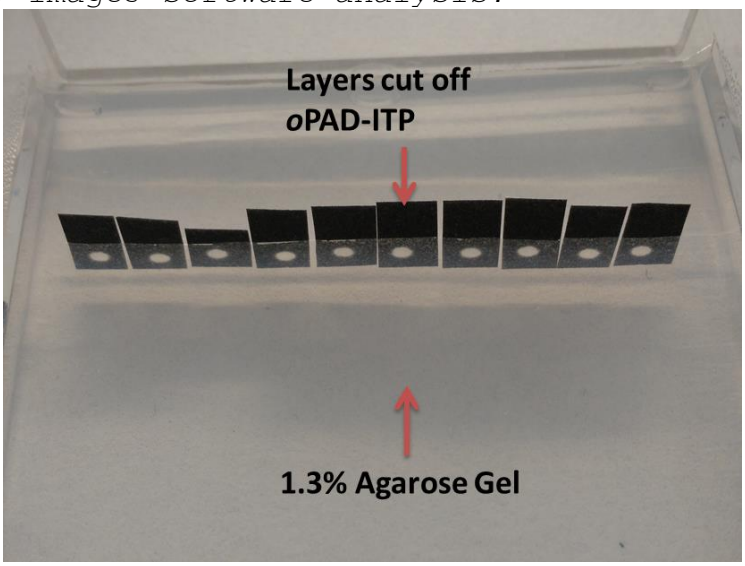

Illustration 3.3. *Photograph of the gel electrophoresis arrangement.*
After ITP, each paper layer of the oPAD-ITP was cut off, dried, and inserted into a 1.3% agarose gel containing 10 µg/mL EtBr for analysis by gel electrophoresis. This photograph shows the individual folds inserted into the gel. A fluorescence scanner was used to image the gel after gel electrophoresis.

3.4 Results and Discussion

3.4.1 Design and Operation of the oPAD-ITP for ssDNA Focusing

Complete details regarding the design and operation of the oPAD-ITP are provided in the Section 3.3. Briefly, however, ssDNA focusing experiments were carried out as follows. An 11-layer oPAD-ITP was assembled as shown in Illustration 3.1, with the insulating slip layer initially

placed between the second and third paper folds. Next, two 3D-printed reservoirs were filled with 1.0 mL of 2.0 mM tris-taurine (TE) containing 40.0 nM ssDNA and 1.0 M tris-HCl (LE), respectively. Electrodes were placed into the reservoirs, an 18 V bias was applied, and the slip layer was removed.

Figure 3.1a shows fluorescence micrographs of each paper layer as a function of time during ITP focusing of ssDNA. The fluorescence intensities increase with time, indicating successful accumulation of ssDNA from the buffer. The majority of the concentrated ssDNA is distributed between 2 to 4 paper layers, which correspond to a width of ~0.4 - 0.7 mm (the average thickness of a single layer of paper is ~180 µm).[20] *The precise concentration of ssDNA in each layer is determined by integrating the fluorescence intensity and then comparing it to a standard calibration curve (Figure 3.2). Typical concentration histograms of ssDNA as a function of position and time are shown in Figure 3.3. Figure 3.1b shows that the peak (maximum) concentration of ssDNA ($C_{DNA,\ peak}$) grows linearly at a rate of ~1 µM/min until it reaches a plateau of ~4 µM at ~4 min. This corresponds to a ~100-fold enrichment of ssDNA from the initial 40.0 nM concentration. This enrichment factor is smaller than previously reported values (~several hundred to 1000) using other paper-based ITP devices.*[8-10] *The main*

reason is that the value of C_{DNA}, peak here is averaged over a thickness of 180 µm, and so it does not represent a true peak concentration. In other words, the oPAD-ITP is a digital device, with each paper fold representing one bin.

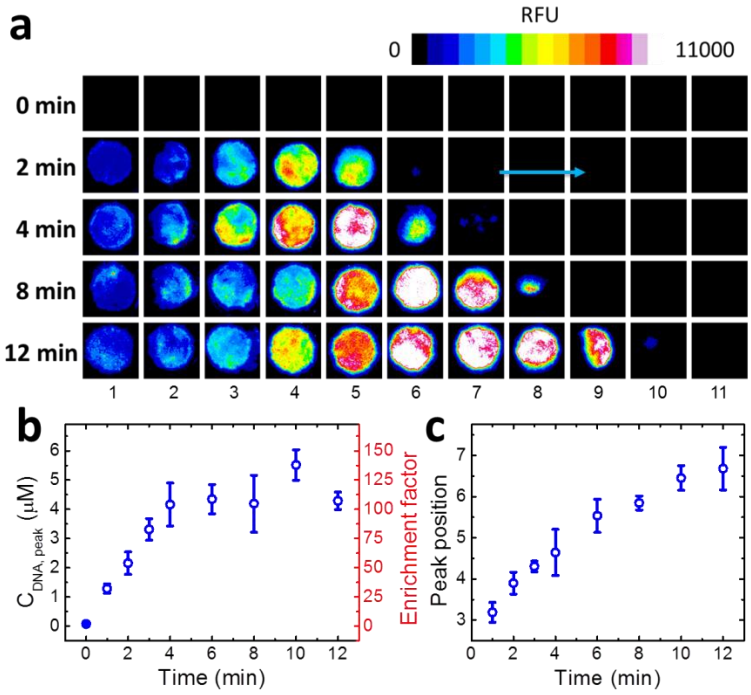

Figure 3.1. *ITP focusing of ssDNA using an 11-layer oPAD-ITP.*
(a) Time-resolved fluorescence micrographs of ssDNA during focusing at 18 V. The TE and LE were 2.0 mM tris-taurine (pH 8.7) and 1.0 M tris-HCl (pH 7.3), respectively, and the initial TE/LE boundary was between Layers 2 and 3. The initial ssDNA concentration in the TE solution was 40.0 nM. (b) Plot of the ssDNA peak concentration as a function of time. The peak concentrations were calculated from the images in (a). (c) Plot of peak position (in terms of layer number) as a function of time. The peak positions were obtained by Gaussian fitting of the ssDNA distributions shown in Figure 4.3. The error bars in (b) and (c) represent the standard deviation for three independent replicates.

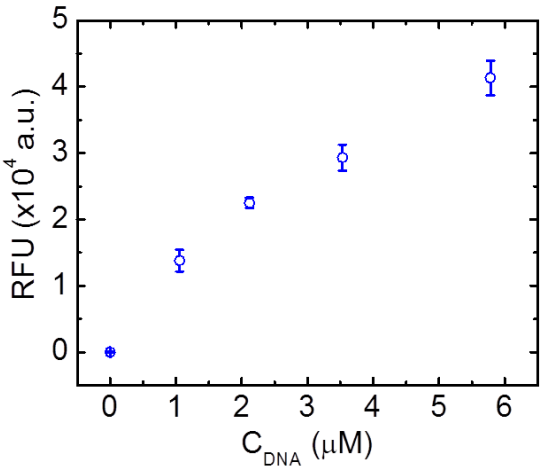

Figure 3.2. *ssDNA calibration curve.*
For each data point, an 11-layer origami paper (same as the oPAD-ITP) was prepared, and 15.0 μL ssDNA solution having the indicated concentrations was added to the inlet and allowed to wet all 11 layers. Excess liquid was removed, the paper was dried in the dark, and then the fluorescence image of each layer was obtained. The average RFU intensity of all layers is plotted as a function of the ssDNA concentration.

In microfluidic ITP experiments, sample ions are focused at the TE/LE boundary, where there is a sharp change in the magnitude of the electric field. As the experiment progresses, this boundary migrates toward the LE reservoir. Figure 3.1a shows that this behavior is qualitatively replicated in the oPAD-ITP. That is, the location of maximum ssDNA concentration migrates from left to right, mirroring the location of the TE/LE boundary. This result is quantified in Figure 3.1c. Here, the peak positions were determined by Gaussian fitting of the ssDNA distributions (Figure 3.3), and then plotted as a function of time. This relationship is nearly linear, and the slope of this plot

(~0.3 layers/min) represents the velocity of the TE/LE boundary. The mobility of the TE/LE boundary (μ_{ITP}) can be estimated using eq 3.1.

$$\mu_{ITP} = \frac{a \times d}{E} \qquad (3.1)$$

Here, a is the slope of the linear fit in Figure 3.1c, d is the thickness of one paper layer (~180 μm), and E is the electric field strength. E can be estimated by dividing the applied voltage (18 V) by the total thickness of the 11-layer origami paper. This assumes that the majority of the potential drop occurs in the paper channel rather than the reservoirs, which given the higher resistance of the paper is reasonable. The calculated value of μ_{ITP} is 1.08 10^{-10} $m^2/s \cdot V$, one order of magnitude smaller than its counterpart in conventional microfluidic channels or other paper ITP devices (~10^{-9} $m^2/s \cdot V$).[96,100] A possible explanation is that all ions are forced to travel through the three-dimensional cellulose matrix in the oPAD-ITP. This might increase the true migrational distance (tortuous path), and in addition could result in specific interactions between the ions and the cellulose fibers. This view is consistent with our previously reported finding that the mobilities of ions through paper are about one order of magnitude smaller than in free solution.[97] In other paper-based ITP devices, ions migrate laterally across the paper (rather than normal to

it, which is the case for the oPAD-ITP), which can lead to different migrational pathways.[85,100]

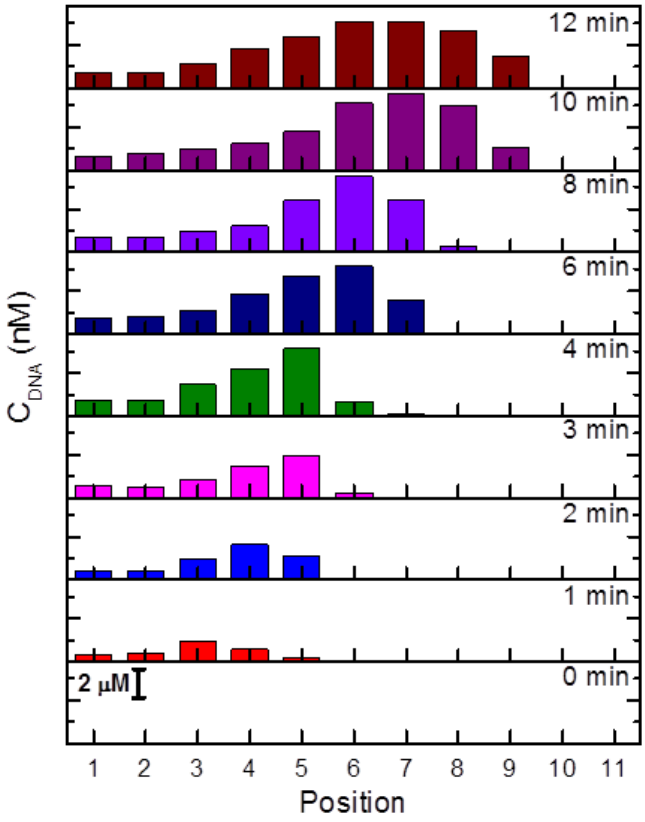

Figure 3.3. *Distributions of ssDNA in the oPAD-ITP as a function of time.*
A 1.0 mL solution containing 40.0 nM ssDNA and TE buffer was added to the TE reservoir, and 1.0 mL of the LE buffer was added to the LE reservoir. After applying a voltage of 18 V for different lengths of time, the oPAD-ITP was unassembled, the individual paper layers were cut out, dried in the dark, and then imaged using fluorescence microscopy. The integrated fluorescence intensities are plotted here.

3.4.2 Collection and Extraction Efficiency

In ITP, the collection efficiency (C%) is defined as the percentage of the original sample that is accumulated by an ITP device during a defined period of time. We calculated C% for the oPAD-ITP using eq 3.2.[109]

$$C\% = \frac{\sum_{j=1}^{11} C_j V_j}{C_0 V_{TE}} \qquad (3.2)$$

Here, C_j is the concentration of ssDNA on the j_{th} layer and V_j is the liquid capacity of one paper layer, ~0.5 µL. C_0 and V_{TE} are the original sample concentration and the volume of the TE solution, respectively. The calculated value of C% is plotted as a function of time in Figure 3.4a. Between 0 and 4 min, C% increases linearly with time at a rate of ~4%/min. At longer times, however, C% increases at a lower rate. The maximum value of C% is ~30%, which is obtained after 12 min. The main reason for the slower accumulation rate at long times is probably related to the lowering of the ssDNA concentration in the reservoir as the experiment progresses. Another possible reason is that the broadened distribution of the focused ssDNA after 4 min (Figures 3.1a and 3.3) affects the ion concentration profile near the TE/LE boundary, thus disrupting the local electric field.

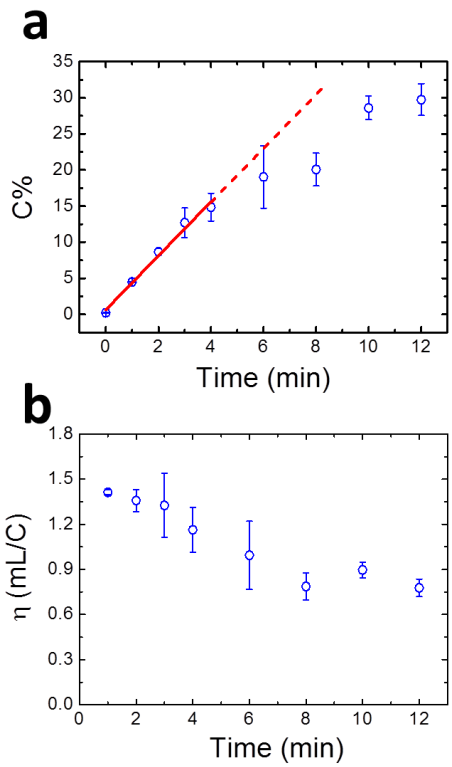

Figure 3.4. *Focusing data for ssDNA using an 11-layer oPAD-ITP.*
(a) Plot of collection efficiency (C%) as a function of time. C% was calculated by comparing the amount of ssDNA injected into the device with the sum of the amount of ssDNA present on each paper layer following ITP. (b) Plot of extraction efficiency (η) as a function of time. The definition of η is given in eq 3.3. The raw data used to generate the plots in (a) and (b) are shown in Figures 3.4 and 3.6. The error bars represent the standard deviation for three independent replicates.

In ITP, the extraction efficiency is the ability of the device to concentrate a defined sample volume per unit electrical charge consumed. Rosenfeld and Bercovici used a descriptor, η, to represent the extraction efficiency during focusing of small fluorescent molecules by their paper-based ITP device.[100] The value of η is calculated using eq 3.3. A

high value of η *means less energy is required to concentrate a sample.*

$$\eta = \frac{N_{DNA}(t)}{C_0 \int_0^t i(t)dt} \qquad (3.3)$$

Here, $N_{DNA}(t)$ *is the total moles of ssDNA focused by the oPAD-ITP after t min. In our experiments, the current, i(t), remained almost constant at ~0.53 mA during the focusing process (Figure 3.5), and* $N_{DNA}(t)$ *is linearly correlated with time for the first 4 min of the experiment (Figure 3.4a). Therefore,* η *is 0.9-1.5 mL/C (Figure 3.4b), which is 3-5 times higher than the value reported by Bercovici (0.3 mL/C).*[100] *The higher* η *value observed in our experiments is caused primarily by the lower TE concentration (2.0 mM taurine/2.0 mM tris), required for operation of the oPAD-ITP, compared to that used by Rosenfeld and Bercovici (10 mM tricine/20 mM bistris). Specifically, when lower concentrations of TE are used, the sample ions carry a higher percentage of the total current, and this leads to better extraction efficiencies.*

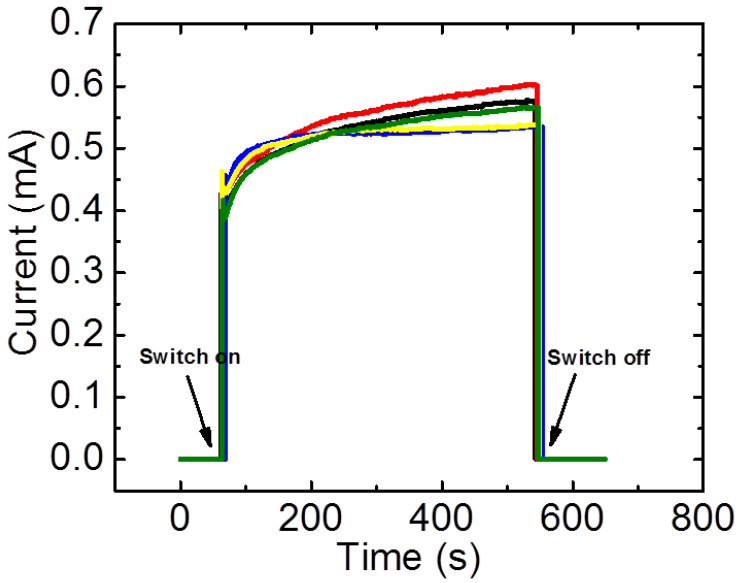

Figure 3.5. *Current vs time curve for a typical ITP experiment.*
In this case, the ITP voltage (18 V) was applied using a CHI 650C potentiostat (CH Instrument, Austin, TX) so that the current could be recorded. Five replicates are shown in the figure.

3.4.3 Effect of Initial Sample Concentration on Enrichment

According to classical peak-mode ITP theory, when the sample concentration is negligible compared with the concentration of either electrolyte (TE and LE), the maximum peak sample concentration ($C_{sample,peak}$) depends solely on the TE and LE composition and is independent of the initial sample concentration (C_0).[96] *Therefore, the enrichment factor (EF), defined as the value of $C_{sample,peak}$ divided by C_0, will be inversely proportional to the value of C_0. Accordingly, we examined the oPAD-ITP performance using*

different initial ssDNA concentrations ($C_{DNA,0}$), but otherwise the same experimental procedure described in the previous section.

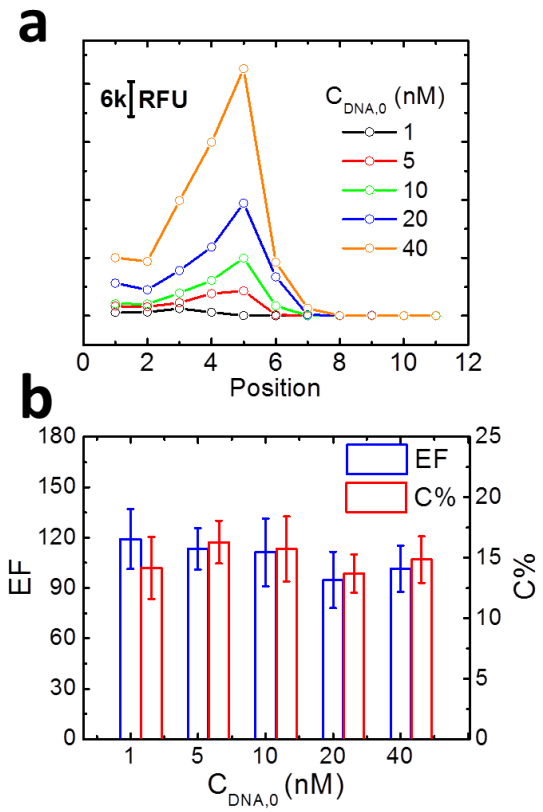

Figure 3.6. *Focusing data as a function of the initial concentration of ssDNA for an 11-layer oPAD-ITP. (a) Distribution of ssDNA as a function of position (paper layer number) and initial ssDNA concentration after 4.0 min of ITP at 18 V. Each data point was calculated by integrating the RFU of the fluorescence image of each paper layer. (b) Enrichment factor (EF) and collection efficiency (C%) as a function of the initial ssDNA concentration. The ssDNA concentration was calculated by comparing integrated RFU value with the calibration curve shown in Figure 3.2. The error bars represent the standard deviation for three independent replicates.*

Figure 3.6a shows the distribution of accumulated ssDNA as a function of its position within the oPAD-ITP and $C_{DNA,0}$ after 4 min of ITP focusing. The concentration profiles shown in this figure are similar in shape, indicating that the electric field in the devices is not a strong function of $C_{DNA,0}$. EFs and C%s as a function of $C_{DNA,0}$ are presented in Figure 3.6b. Surprisingly, both quantities have roughly constant values of ~100 and 15%, respectively, as $C_{DNA,0}$ varies from 1.0 nM to 40.0 nM. This finding is in contrast to the expectation that both quantities should be inversely related to $C_{DNA,0}$. There are several possible explanations for this observation. First, and most likely, the accumulation process during the first 4 min was limited by the migration of ssDNA within the cellulose matrix and did not reach the theoretical maximum accumulation. Therefore, ssDNA accumulates in the channel at a constant rate regardless of the initial concentration $C_{DNA,0}$, leading to constant EF and C% values. Second, as mentioned before, the value of EF is calculated from $C_{DNA,peak}$, which is averaged over the thickness of a 180 µm paper fold. This introduces some uncertainty into the determination of EFs. Third, electroosmotic flow (EOF) may play a role in ITP focusing by generating a counter flow in the paper channel. This would slow ssDNA migration and broaden the peak. However, a control experiment shown in Figure 3.7 does not support this

idea, because the EF is unchanged in presence and absence of EOF.

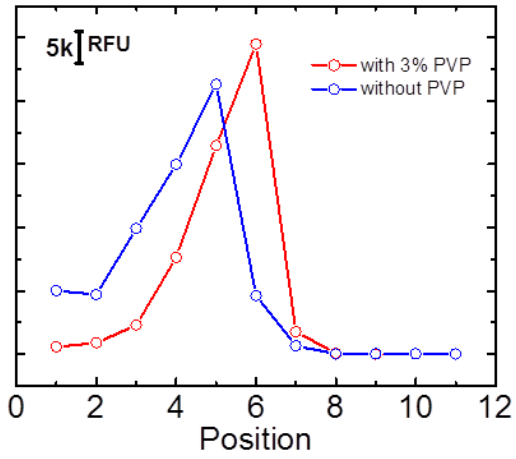

Figure 3.7. *Electroosmotic flow control experiment. The red trace presents the distribution of ssDNA when there was 3.0% polyvinylpyrrolidone (PVP) initially present in the LE to suppress EOF. The blue trace is same experiment without PVP. Both ITP experiments were run at 18 V for 4.0 min. The results show that EOF did not significantly affect the value of EF and C% in the oPAD-ITP.*

3.4.4 Electric Field in the oPAD-ITP

In microfluidic devices, focusing of analyte at the TE/LE boundary results from a sharp transition of the electric field between the TE and LE.[118] *We assume that the same is true for the oPAD-ITP, but to be certain we measured the electric field profile during ITP focusing. For this study, we adopted an approach reported by Santiago and coworkers.*[118] *Specifically, we added* $Ru(bpy)_3^{2+}$, *a nonfocusing fluorescent tracer (NFT),*[118] *to the LE solution, and then determined its distribution across the paper folds*

in the oPAD-ITP after focusing. In principle, the NFT will migrate through the channel during ITP and leave behind a concentration distribution that is inversely proportional to the local electric field strength.

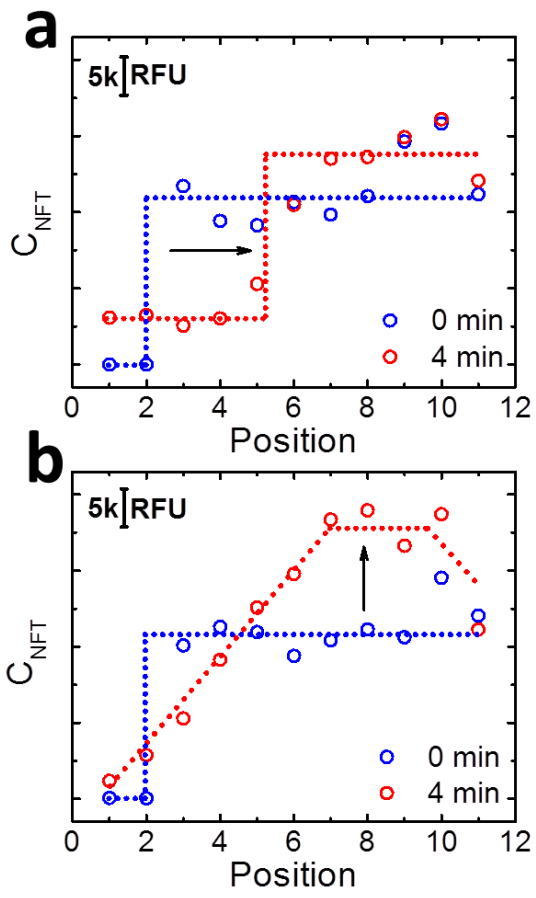

Figure 3.8. *Electric field profiles in an oPAD-ITP obtained using* $Ru(bpy)_3^{2+}$ *as a NFT.*
Each data point represents the integrated RFU value of the fluorescence image of each paper layer. The dash lines represent the guidelines for the NFT distributions, which corresponding to electric field strength in the channel. (a) Distributions of the NFT before application of the voltage and at t = 4 min. Initially, the LE solution contained 30.0 μM $Ru(bpy)_3^{2+}$*. (b) Distribution of the NFT before application of the voltage and at t = 4 min. For this experiment both reservoirs were filled with LE solution, but the NFT was only present in the anodic reservoir adjacent to Layer 11. To avoid oxidation of* Cl^- *at the anode, Ag/AgCl wire electrodes replaced the Pt wire electrodes used in (a). For all experiments the applied voltage was 18 V.*

Figure 3.8a shows the distribution of the NFT concentration (C_{NFT}) in an oPAD-ITP at t = 0 and 4 min. These data were obtained using the same experimental conditions used for the ssDNA focusing experiments (e.g., Figure 3.1). At t = 0 min, the NFT is only present in the LE zone (Layers 3 to 11), and there is a concentration step between Layer 2 and 3. This step represents the TE/LE boundary where the slip layer was initially located. At t = 4 min, the concentration step is still present, but it has moved three positions to the right. This is the same location where ssDNA accumulated after 4 min of ITP (Figure 4.1a), thereby confirming that ssDNA accumulation occurs at the TE/LE boundary. Based on the value of C_{NFT} in the channel, the electric field strength in the LE and TE zones can be approximated as 3 and 14 kV/m, respectively.

There is a small possibility that the step-shaped distribution of NFT shown in Figure 3.8a (t = 4 min) could arise from slow migration of NFT in the paper matrix. Accordingly, we carried out a control experiment to rule out this possibility. Specifically, instead of using two different electrolytes (TE and LE), the same electrolyte (1.0 M tris-HCl) was loaded into both reservoirs, though the NFT is only placed in the LE reservoir. This condition should result in a uniform electric field across the entire channel, and therefore we expected the NFT concentration

step to disappear after applying the voltage. Figure 3.8b shows the result of this experiment. At t =0 min, a step-shaped concentration profile is observed, just as in Figure 3.8a. After 4 min, however, the NFT concentration step is replaced by a trapezoidal distribution: a linear increase from Layer 1 to 7, a plateau from Layer 7 to 10, and finally a decrease at Layer 11. This unusual distribution is mainly caused by the mobility differences of the NFT in the paper medium and in free solution,[97] which determines the value of C_{NFT} near the paper/reservoir boundary (boundary effect). As shown in Figure 3.8b, accumulation of NFT is observed near the right paper/reservoir boundary, due to larger influx of NFT from that reservoir into the paper. In the contrast, depletion of NFT near the left paper/reservoir boundary results from larger out-flow of NFT from paper into that reservoir.

Based on the results in this section, we conclude that ssDNA focusing is caused primarily by the electric field transition at the TE/LE boundary, and to a much lesser extent by boundary effect.

3.4.5 ITP Focusing of a dsDNA ladder

Even though short DNA strands (usually several tens of bases) are widely used as model targets for developing DNA

sensing technologies, real-world DNA, for example in viruses or bacteria, is usually composed of thousands of base pairs.[119,120] *Accordingly, it is essential for an ITP device to be capable of focusing DNA strands longer 100 bp. In this section, we demonstrate the use of the oPAD-ITPs for focusing a 100 bp dsDNA ladder containing 100-1517 bp dsDNA. The same experimental setup and buffer conditions used in the previous section were used for these experiments. That is, the dsDNA ladder was loaded into the TE buffer, and the voltage was switched on for 10 min.*

After ITP, each fold of paper was removed from the channel, and gel electrophoresis was used to elute its dsDNA content (Illustration 3.3). The dsDNA on the gel was stained by EtBr and then imaged using a fluorescence scanner. A raw fluorescence image of a typical gel is shown in Figure 3.9a. Here, each lane represents one paper layer. The right-most lane was used as a standard (the dsDNA ladder solution was dropcast onto a single paper fold, but it was not exposed to ITP). Clearly, the concentrations for the different dsDNA lengths achieve their maximum values at Layers 5 and 6. Recall that the peak position for the shorter ssDNA was at Layer 7 (Figure 3.3). The slightly reduced mobility of the longer dsDNA ladder is probably due to its stronger affinity for the cellulose matrix.[121]

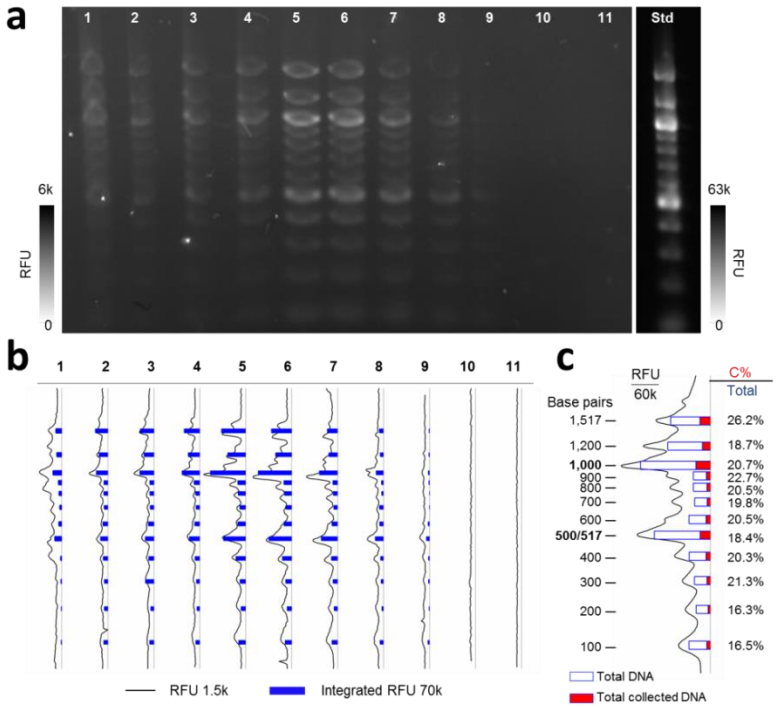

Figure 3.9. *ITP focusing of a 100 bp dsDNA ladder. Initially, 1.0 µL of a 500 µg/mL solution of the 100 bp dsDNA ladder was dissolved in 1.0 mL of the TE solution (final dsDNA concentration: 0.5 µg/mL). Following 10 min of ITP of this solution at 18 V, each fold of the 11-layer oPAD-ITP was cut from the device, and gel electrophoresis was used to elute the dsDNA in that layer (Illustration 3.3). (a) The left panel is a fluorescence micrograph of the gel after electrophoresis and staining with 10 µg/mL EtBr. The numbers under the lanes of the gel correspond to the Layer numbers of the oPAD-ITP. The right panel is a control experiment showing the result of gel electrophoresis of a paper fold onto which 1.0 µL of a 500 µg/mL dsDNA ladder solution was dispensed (no ITP). The gel electrophoresis conditions for all paper folds were: 1.3% agarose gel, 100 V, and 50 min. (b) The black lines are fluorescence line profiles of the stained gels in each lane of the left panel in (a). The integral of the profiles is represented by the blue bar. (c) The black line is the fluorescence line scan of the gel in the right panel in (a). The blue hollow and red solid bars represent the total dsDNA placed in the reservoir prior to ITP and the total collected dsDNA on the oPAD-ITP, respectively. The calculated C% values for each dsDNA length are shown in the right-most column.*

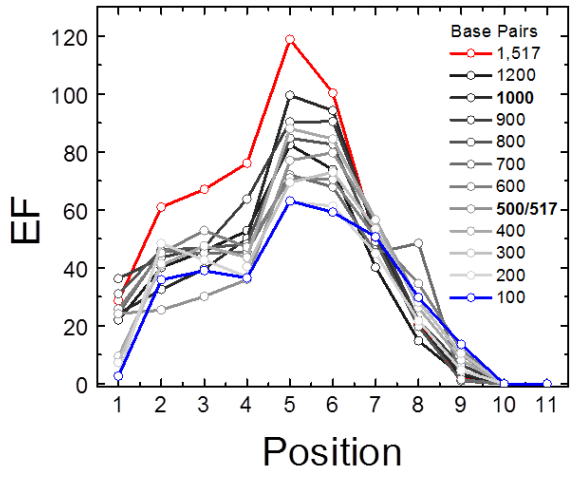

Figure 3.10. *EF analysis of the ITP of a dsDNA ladder. Same experiment setup and buffer conditions were used as Figure 3.1. The dsDNA ladder was loaded into TE buffer. After ITP at 18 V for 10 min, the oPAD-ITP was unfolded and each paper layer was cut off and inserted in gel as Illustration 3.3 for gel electrophoresis. The gel electrophoresis image of each DNA band in each lane was analyzed using ImageJ software. The EF plotted here was calculated as the area of filled blue bars in Figure 3.9b divided by the area of corresponding hollow blue bars in Figure 3.9c.*

Figure 3.9b presents line profiles (black lines) of the RFU corresponding to the dsDNA bands in Figure 3.9a. The integrated RFU values of each dsDNA band, representing the dsDNA amount, are shown as filled blue bars aligned with the line profiles. Figure 3.9c is the same analysis for the ladder standard (right side of Figure 3.9a): the black lines present the RFU line profiles, the hollow blue bars show the integrated RFU value of each dsDNA band, and filled red bars equal the sum of the dsDNA amount on individual paper folds (equivalent to the filled blue bars in Figure 3.9b). The EF

for each dsDNA length was calculated as the area of filled blue bars in Figure 3.9b divided by the area of hollow blue bars in Figure 3.9c. Figure 3.10 is a plot of the EF as a function of the layer number for different dsDNA lengths. The maximum EFs are found at Layer 5 and they vary from 60 to 120, which is consistent with the ssDNA results. The C% values of each dsDNA length are obtained as the area of filled red bars divided by the area of hollow blue bars in Figure 3.9c. The right column of Figure 3.9c shows that C% for all dsDNA lengths ranges from ~15-20%. These results support our conclusion that focusing of dsDNA having different lengths (up to 1517 bp) in the oPAD-ITP yields a consistent C% of ~20% and EF of ~100.

3.5 Summary and Conclusions

In this chapter we presented a novel origami paper-based device, the oPAD-ITP, suitable for carrying out low-voltage ITP focusing of DNA. Our approach resolves several issues inherent to previously reported paper-based ITP designs, including high operating voltage, solvent evaporation, and difficult sample reclamation. Using the oPAD-ITP, we demonstrated >100-fold enrichment of ssDNA and dsDNA having lengths of up to 1517 bps. The time required for enrichment is ~10 min, the paper device can accommodate

solution volumes of up to 1.0 mL, and it is battery operated (18 V). The collection efficiency ranges from ~15-20%. The electric field profiling experiments, using $Ru(bpy)_3^{2+}$ *as a tracer, clearly show that the focusing mechanism in the oPAD-ITP is the same as in bulk liquid solutions: accumulation of sample at the boundary between the TE and LE.*

*Chapter 4: Faradaic Ion Concentration Polarization on a Paper Fluidic Platform**

4.1 Synopsis

We describe the design and characteristics of a paper-based analytical device for analyte concentration enrichment. The device, called a hyPAD, uses faradaic electrochemistry to create an ion depletion zone (IDZ), and hence a local electric field, within a nitrocellulose flow channel. Charged analytes are concentrated near the IDZ when their electrophoretic and electroosmotic velocities balance. This process is called faradaic ion concentration polarization (fICP). The hyPAD is simple to construct and uses only low-cost materials. The hyPAD can be tuned for optimal performance by adjusting the applied voltage or changing the electrode design. Moreover, the throughput of hyPAD is two orders of magnitude higher than that of conventional, micron-scale microfluidic devices. The hyPAD is able to concentrate a range of analytes, including small molecules, DNA, proteins, and nanoparticles, in the range of 200-500-fold within 5 min.

---

* *Chapter 4 is based on a manuscript: X. Li, L. Luo and R. M. Crooks, Faradaic ion concentration polarization on a paper fluidic platform, submitted to Anal. Chem. XL and LL designed the experiments. RMC was the research advisor. XL performed and analyzed the experiments. XL and RMC wrote the manuscript.*

4.2 Introduction

In this paper, we report integration of the method of faradaic ion concentration polarization (fICP) with paper-based analytical devices (PADs).[18,122] The results show that this new family of PADs provides an inexpensive means for enriching the concentration of fluorescent molecules, nucleic acids, proteins, and nanoparticles by factors ranging from 200-500 within 5 min. Because they are fabricated using both nitrocellulose and cellulose paper, we call them hybrid PADs or simply hyPADs (Illustration 4.1a). There are several desirable characteristics of the hyPAD design. First, hyPADs are easy to fabricate using low-cost materials. Complicated channel modifications, such as membrane patterning,[123,124] which are usually required for non-faradaic ICP, are not necessary for fICP. Second, the fICP process can be tuned for optimal performance by adjusting the applied voltage. Third, the use of a bipolar electrode (BPE)[125-129] to drive faradaic reactions eliminates the need for an external circuit connection and a second power supply. Finally, the throughput of hyPAD is significantly larger (two-orders of magnitude) than conventional microfluidic channels. All of these points will be discussed in more detail later.

Two- and three-dimensional PADs were first introduced by the Whitesides group in 2007 and 2008, respectively.[18,19]

Since that time, a number of means for detection of analytes on paper platforms have been reported.[2,130] However, improving the limit of detection (LOD) of PADs remains important in several fields, particularly for point-of-care (POC) applications in medicine.[10,60,130,131] On-chip sample preconcentration is one attractive solution to this problem because it can be implemented with existing detection strategies but still lower LODs. A variety of creative approaches for preconcentration have been reported for use with conventional glass and plastic microfluidic devices,[132,133] but analogous reports for use with paper-based devices are more limited.[85,97,134-136]

Conventional ICP, which is an electrokinetic molecular trapping technique,[137,138] has previously been adapted to paper platforms for preconcentrating analytes. For example, in 2014, Gong et al. patterned a nitrocellulose paper channel with a selectively permeable membrane (Nafion) to create a micro/nanochannel junction.[139] Upon application of an electric field across the channel, permselective charge transport through Nafion led to formation of ion depletion zone (IDZ) and ion enrichment zone (IEZ) at opposite sides of the membrane. Due to reduction of the charge carrier (e.g., ion) concentration in the IDZ, the local electric field strength increased and blocked ions from entering this region of the channel. For example, negatively charged DNA,

transported by electroosmotic flow (EOF) into the vicinity of the IDZ, concentrated at the IDZ boundary where the EOF and electromigration velocities balanced. More recently, there have been additional publications[140-144] demonstrating the ICP phenomena using PADs having designs similar to that of Gong et al.[139]

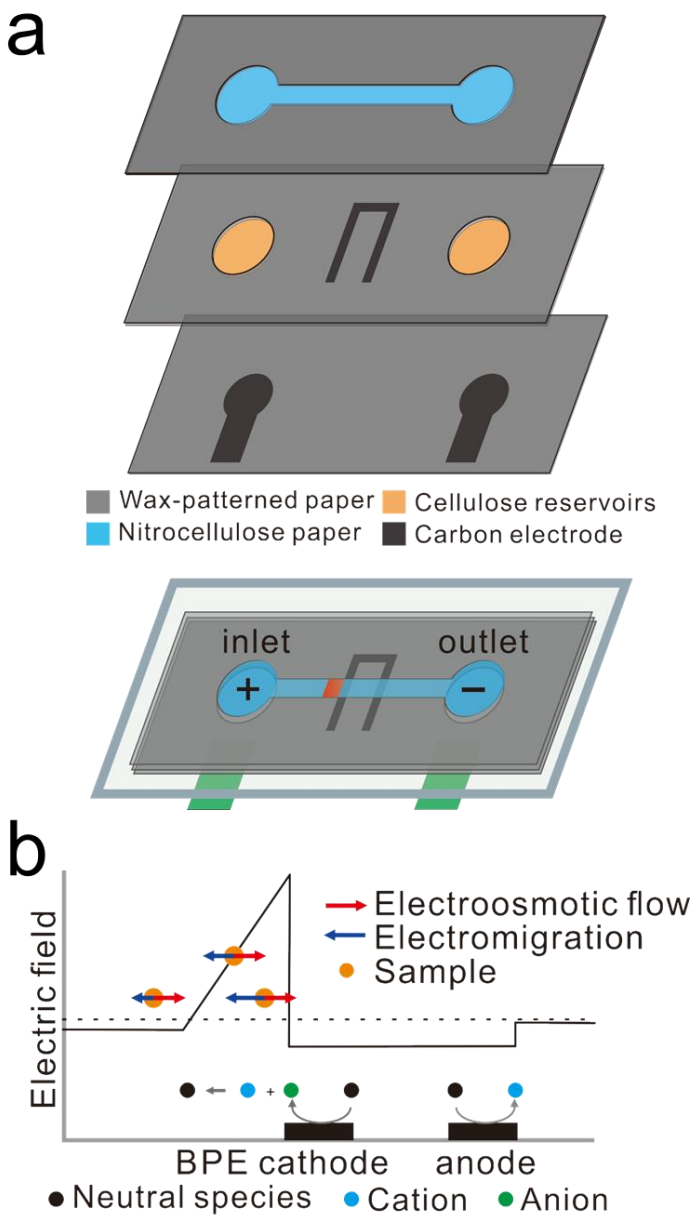

Illustration 4.1. *Scheme of the hyPAD.*

The technique of fICP, which we report here, is similar to conventional ICP with two major exceptions.[122,127] *First,*

instead of a micro/nanochannel junction, the IDZ is created by an electrode (a BPE in this case) patterned within the channel. Second, instead of selective charge transport, the IDZ in fICP is formed as a result of faradaic processes at the electrode surface. These points are illustrated in Illustration 4.1b. The external voltage applied to the channel via the two carbon paste electrodes shown in Illustration 4.1a is sufficient to drive simultaneous water oxidation (eq 4.1) and reduction (eq 4.2) reactions at opposite ends of the BPE.[122,126]

BPE anode: $2H_2O \rightarrow 4H^+ + O_2 + 4e^-$ *(4.1)*

BPE cathode: $2H_2O + 2e^- \rightarrow 2OH^- + H_2$ *(4.2)*

$OH^- + TrisH^+ \rightarrow Tris + H_2O$ *(4.3)*

The faradaic reaction (eq 4.2) at the BPE cathode generates OH^-, which can neutralize cations ($TrisH^+$) present in the buffer (eq 4.3), resulting in uncharged products (H_2, Tris, and H_2O).[122] *The local loss of charge carrying ions results in formation of an IDZ. Charged analytes, such as DNA, will then be concentrated at the IDZ boundary by the same principles operative in conventional ICP.*

In the present article, we show that the hyPAD is capable of concentrating a fluorescent molecule ($BODIPY^{2-}$) up to 513-fold within 5 min. The throughput of hyPAD is ~600 fold higher than conventional microfluidic devices. Furthermore, we demonstrate the ability of hyPADs to

concentrate DNA, proteins, and gold nanoparticles (AuNPs), which illustrates the potential application of hyPADs for detecting biological molecules and integrating with nanoparticle-based colorimetric assays.

4.3 EXPERIMENTAL

4.3.1 Chemicals and Materials

A stock solution of 0.5 M Tris-$HClO_4$ (pH 8.1) was prepared from Tris(hydroxymethyl)aminomethane (Sigma-Aldrich, St. Louis, MO) dissolved in water and titrated with perchloric acid (70%, Fisher Scientific, Walthman, MA). 4,4-Difluoro-1,3,5,7,8-pentamethyl-4-bora-3a,4a-diaza-s-indacene-2,6-disulfonic acid ($BODIPY^{2-}$) and albumin from bovine serum (BSA-AF, modified with Alexa Fluor 488) were obtained from Invitrogen (Carlsbad, CA). DNA (DNA-Cy5, 5`-GGA GTA AAT GTT GGA GAA CAG TAT CAA CAA-Cy5-3`; DNA-SH, 5`-SH-C6-AAA AAA AAA ATA CCA CAT CAT CCA T-3`) were ordered from Integrated DNA Technologies (Coralville, IA) and purified by HPLC. AuNPs (20 nm diam.) were purchased from Sigma-Aldrich (St. Louis, MO). All solutions were prepared using deionized water (> 18.0 MΩ·cm) purified by a Milli-Q Gradient System (Bedford, MA).

4.3.2 Device Fabrication

The hyPAD comprises three layers and is constructed from both nitrocellulose and cellulose paper (Illustration 4.1a). Whatman Grade 1 cellulose paper (~180 μm thick, Fisher Scientific) was patterned with wax using a Xerox ColorQube 8750DN inkjet printer.[20] All three layers of paper were fully covered by wax except for two hydrophilic, cellulose reservoirs present on the second layer (more detailed information about the hyPAD design is provided in the Illustration 4.2). The wax-patterned paper was placed in an oven at 120 ^{o}C for 45 s to melt the wax through the thickness of paper. Next, two driving electrodes and a BPE were stencil-printed on the first and second layers, respectively, using conductive carbon paste (Engineered Conductive Materials, Delaware, OH).[145] The third layer of cellulose paper and an unpatterned piece of nitrocellulose paper (0.45 μm pore size, Thermo Scientific) were then cut to the same size using an Epilog laser engraving system (Zing 16). The nitrocellulose paper was then placed inside the cut-out of the third layer of cellulose paper.[44] Finally, the driving electrodes were connected with copper tape and the entire paper device was laminated with plastic (3M) that contained two holes as inlet and outlet for the solution.

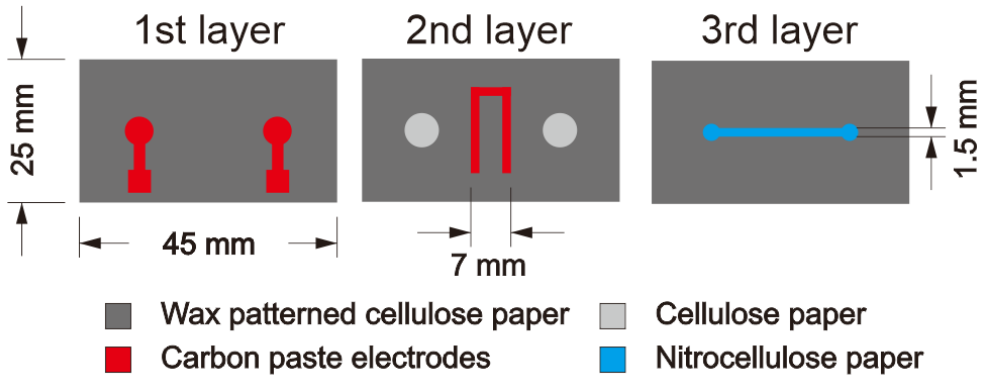

Illustration 4.2. *Details of the hyPAD configuration. The hyPAD was designed using CorelDraw 12 software. Cellulose paper was patterned with wax using a Xerox ColorQube 8750DN inkjet printer. The third layer was assembled using both cellulose and nitrocellulose paper. The hollow-channel in the cellulose paper and the replacement nitrocellulose channel were the same size and shape, and both were cut using an Epilog laser engraving system.*

4.3.3 Device Operation and Microscopic Analysis

The hyPAD operates as follows. First, 80 µL of the analyte dissolved in 100 mM Tris-$HClO_4$ (pH 8.1) is added at the inlet to pre-wet the nitrocellulose channel. Second, a potential bias of 100 V is applied between the two driving electrodes using a Lambda LLS9120 DC power supply. As soon as the voltage is applied, faradaic reactions occur at the BPE, and, as we will show later, an IDZ begins to develop near the BPE cathode. This initiates formation of a concentrated band of analyte.

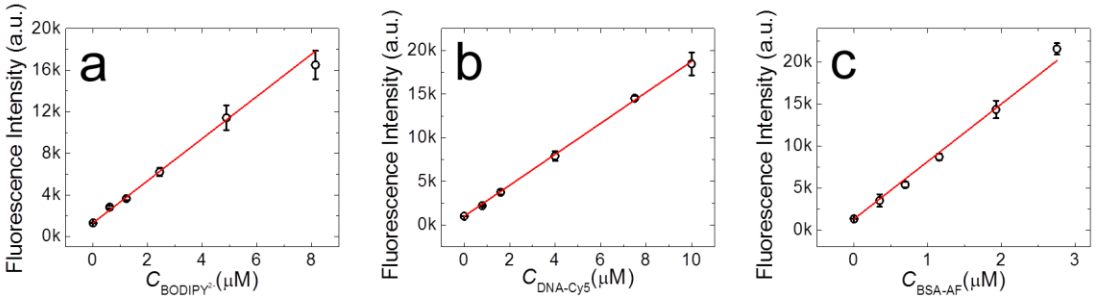

Figure 4.1. *Calibration curves for $BODIPY^{2-}$, DNA-Cy5, and BSA-AF.*
The experiments were performed in following steps. A series of solutions containing different concentrations of the analytes were placed onto individual nitrocellulose paper strips. These strips were then imaged using fluorescence microscopy. The lighting conditions used to obtain the calibration curves were as similar as possible to those used for the hyPAD experiments. The fluorescence micrographs were then analyzed using ImageJ software to obtain the average fluorescence intensities for each concentration. Error bars in the figure indicate the standard deviations obtained from three independent replicates. The red lines are the best linear fits to the data.

The enrichment process was visualized using a Nikon AZ100 fluorescence microscope. Micrographs were obtained every 1 s using a 100 ms exposure time. The following Nikon filters were used for each analyte: $BODIPY^{2-}$ and BSA-AF, 460-500 nm excitation and 510-560 nm emission; DNA-Cy5, 590-650 nm excitation and 663-738 nm emission. For the AuNP enrichment experiment, a cell phone (Huawei Honor 5X) was used to take photos of the hyPAD at different times under nearly identical lighting conditions. All images were processed using ImageJ software (NIH, Bethesda, MD) to obtain the maximum and integrated fluorescence intensities. These intensity values were then compared to calibration

curves of fluorescence intensity vs. analyte concentration (Figure 4.1) to obtain analyte concentrations. The hyPADs are disposable, and therefore a different device was used for each experiment.

4.4 Results and Discussion

4.4.1 Enrichment of the Fluorescent Tracer $BODIPY^{2-}$ Using hyPADs

In this section, we examine the performance of hyPADs for the enrichment of the fluorescent tracer $BODIPY^{2-}$.[88,146,147] In subsequent sections we will discuss the mechanism of fICP on hyPADs and show that hyPADs are capable of enriching DNA, proteins, and AuNPs.

A detailed description of hyPAD operation is provided in the Section 4.3. Briefly, 80 μL of a solution containing 100 mM Tris-$HClO_4$ and 20 nM $BODIPY^{2-}$ are added to the hyPAD inlet (Illustration 4.1a) to wet the channel. Next, a voltage of E_{tot} = 100 V is applied between the two driving electrodes. The evolution of $BODIPY^{2-}$ enrichment can then followed by fluorescence imaging.

Figure 4.2a shows representative fluorescence micrographs obtained using a single hyPAD at different times following application of E_{tot}. The thin, vertical, gray lines overlayed onto the image represent the edges of the BPE cathode. This series of images demonstrates,

qualitatively, that the fluorescence intensity increases with time after application of E_{tot}, indicating successful accumulation of BODIPY^{2-} near the BPE cathode. Moreover, the concentrated BODIPY^{2-} plug remains in a nearly constant position just above one edge of the BPE cathode throughout the entire experiment.

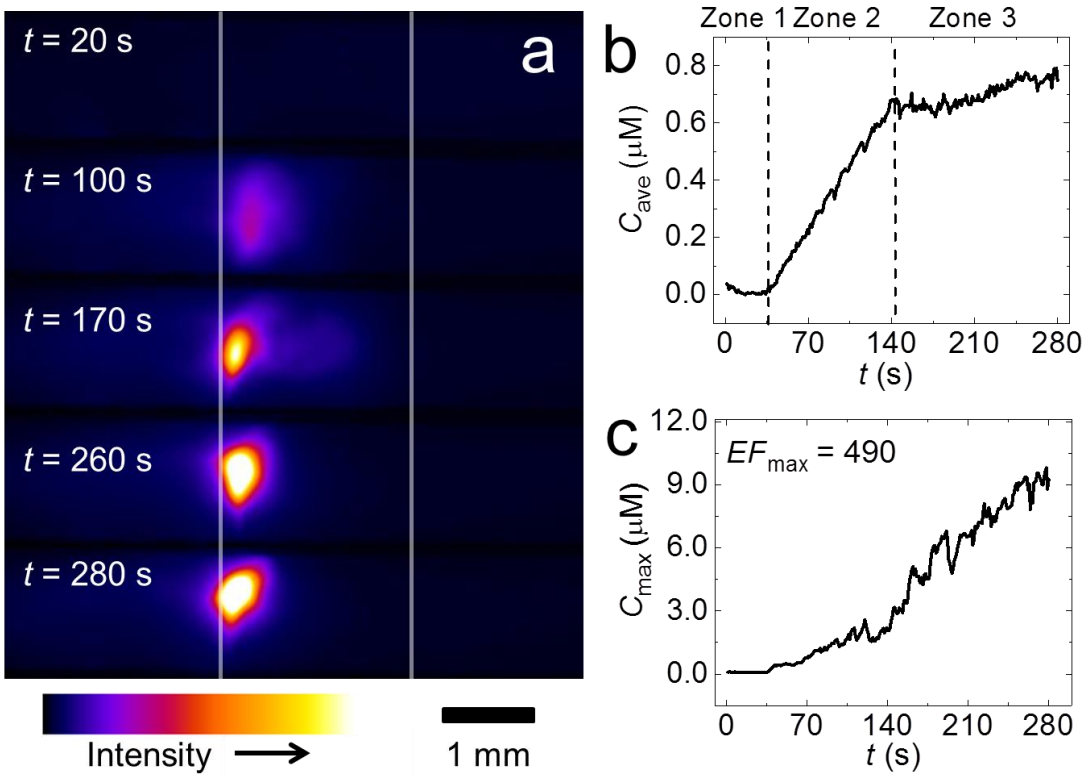

Figure 4.2. *Enrichment of $BODIPY^{2-}$ using hyPADs. (a) Fluorescence micrographs of enriched $BODIPY^{2-}$ in a hyPAD. A solution containing 100 mM Tris-$HClO_4$ and 20 nM $BODIPY^{2-}$ was added at the inlet of hyPAD. A potential bias (E_{tot} = 100 V) was applied at t = 0 s. The gray vertical lines indicate the edges of BPE cathode. (b) Plot of the average $BODIPY^{2-}$ concentration (C_{ave}) vs. t. The value of C_{ave} was obtained by integrating the $BODIPY^{2-}$ fluorescence intensity near the BPE cathode of each micrograph in (a) and comparing it to a $BODIPY^{2-}$ fluorescence intensity calibration curve (Figure 4.1). The curve is divided into three distinct zones by dashed lines. (c) Plot of the maximum $BODIPY^{2-}$ concentration (C_{max}) vs. t. C_{max} is determined by comparing the highest intensity camera pixel (micrographs in (a)) to the $BODIPY^{2-}$ calibration curve in Figure 4.1. The maximum enrichment factor (EF_{max}) was calculated using the maximum value of C_{max} (C_{max}^{m}) divided by initial $BODIPY^{2-}$ concentration.*

The extent of $BODIPY^{2-}$ enrichment can be quantified by plotting the average $BODIPY^{2-}$ concentration (C_{ave}, Figure 4.2b) and the maximum $BODIPY^{2-}$ concentration (C_{max}, Figure 4.2c) as a function of time (t). The value of C_{ave} was obtained by integrating the $BODIPY^{2-}$ fluorescence intensity near the BPE cathode, and then comparing that value to a $BODIPY^{2-}$ fluorescence intensity calibration curve (Figure 4.2). Figure 4.2b shows that the C_{ave} vs. t curve can be divided into three zones. In Zone 1 (t = 0-50 s), C_{ave} is very close to the background value (below the detection limit of the imaging instrument). In Zone 2 (t = 50-140 s), Cave increases linearly with time, and in Zone 3 (t = 140-280 s) it begins to plateau. The average enrichment factor (EF_{ave}) is obtained by dividing C_{ave} by the initial $BODIPY^{2-}$ concentration (C_{init} = 20 nM). At the end of the experiment (t = 280 s), EF_{ave} = 40.

C_{max} is determined by comparing the fluorescence intensity recorded at the camera pixel yielding the highest signal to the $BODIPY^{2-}$ calibration curve (Figure 4.1). The C_{max} data (Figure 4.2c) increases monotonically with t and exhibits more noise than the analogous C_{ave} plot. The higher noise arises primarily from the stochastic nature of measurements recorded from the single brightest pixel (compared to the averaged data in Figure 4.2b). As will be discussed later, however, a fraction of this noise is also

due to gas bubble formation at the BPE cathode which disrupts BODIPY^{2-} enrichment. The maximum enrichment factor (EF_{max}) for BODIPY^{2-} can be determined from Figure 4.2c using maximum C_{max} value (C_{max}^{m}) divided by C_{init} (20 nM). This results in EF_{max} = 490.

4.4.2 Characterization of the Enrichment Process

To better understand the time-dependent behavior of C_{ave} and C_{max}, a set of C_{init} -dependent experiments was carried out. The conditions for these experiments were the same as in Figure 4.2, except that C_{init} was varied from 1 to 20 nM.

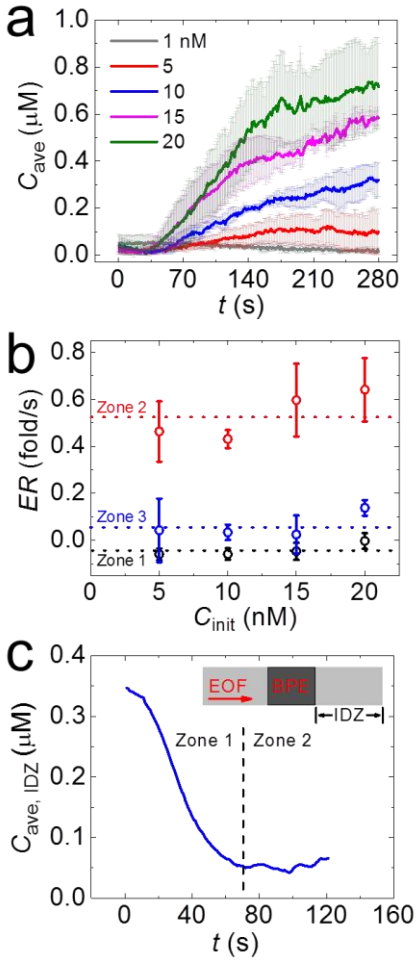

Figure 4.3. *C_{ave} analysis.*
(a) Plots of C_{ave} vs. t for hyPAD enrichment experiments as a function of the initial BODIPY^{2-} concentrations (C_{init}). The solid lines represent the average C_{ave} obtained from three independent measurement. The error bars (shadowing) indicate the standard deviations. (b) Enrichment rate (ER) vs. C_{init} for the three zones defined in Figure 4.2b. The ER is the slope ($\Delta C_{ave}/\Delta t$), obtained from the plots in (a) divided by C_{init}. The error bars represent the standard deviations of three independent measurements. The dashed lines indicate the average ER values for the different C_{init}. (c) Plot of C_{ave} in the IDZ ($C_{ave,IDZ}$) vs. t. The initial BODIPY^{2-} concentration was 350 nM, but other experimental conditions were the same as in Figure 4.2. The inset indicates the IDZ region from which the data are derived. The dashed line indicates the boundary between Zones 1 and 2.

Figure 4.3a shows a family of plots of C_{ave} as a function of t for the indicated values of C_{init}. The error bars (shadowing) correspond to the standard deviations for three replicates (three different hyPADs) for each value of C_{init}. The general trends of these curves are similar to the data shown in Figure 4.2b in that they can be divided into the same three zones: Zone 1 (t = 0-50 s), Zone 2 (t = 50-160 s), and Zone 3 (t = 160-280 s). The enrichment rate (ER) is defined as the slope ($\Delta C_{ave}/\Delta t$) of each curve, in each of the three zones shown in Figure 4.3a, divided by C_{init}. The ER is a representation of how quickly $BODIPY^{2-}$ enriches in each zone. The value of ER is plotted as a function of C_{init} in Figure 4.3b, where the dashed lines represent the average values. The main finding is that ER is independent of C_{init}. The numerical values of ER are: Zone 1: -0.04 fold/s; Zone 2: 0.52 fold/s; and Zone 3: 0.05 fold/s.

In Zone 1 ER is slightly negative (-0.04 fold/s) and independent of C_{init}, which means $BODIPY^{2-}$ is depleted near the BPE cathode at the start of the experiment. We hypothesized that the slightly lower $BODIPY^{2-}$ concentration in Zone 1 at t < 50 s results from formation of the IDZ and designed the following experiment to verify this idea. A detectable concentration of $BODIPY^{2-}$ (350 nM) was introduced into a hyPAD prior to enrichment so that the formation of the IDZ would be revealed by a local decrease in the

$BODIPY^{2-}$ concentration. As shown in Figure 4.3c, the average $BODIPY^{2-}$ concentration in the region of the channel where we expect the IDZ to form ($C_{ave,IDZ}$, indicated by the inset) does indeed decrease immediately after application of E_{tot} = 100 V. The value of $C_{ave,IDZ}$ continues decreasing for ~70 s, and then it reaches a plateau indicating that the IDZ is fully formed. At t = 70 s, the concentration of $BODIPY^{2-}$ in the IDZ drops to only 86% of the original concentration. This result proves our hypothesis that the IDZ forms during the initial stage of the experiment, and it accounts for the ~50 s delay in the onset of $BODIPY^{2-}$ enrichment shown Figures 4.2b and 4.3a.

In Zone 2, $BODIPY^{2-}$ accumulates linearly as a function of t at a rate of 0.52 fold/s (Figure 4.3b). Because both capillary flow and pressure-driven flow are absent in the hyPAD, we believe that enrichment arises from EOF of $BODIPY^{2-}$ from the reservoir toward the vicinity of the IDZ. If this is true, then the EOF velocity (u_{EOF}) in the hyPAD can be calculated from the value of ER: the result is u_{EOF} = 0.78 mm/s. This value is in agreement with literature reports under similar conditions (u_{EOF} ~0.5 mm/s).[100] The ER values achieved using the hyPAD are comparable to those obtained using well-defined, conventional channels (ER = 0.4 to 1.5 fold/s),[146] but importantly the throughput of hyPAD is ~600 times higher due to the much larger channel

dimensions (~20 times taller and ~30 times wider than conventional microfluidic devices).

The value of C_{ave} reaches its maximum value in Zone 3, and the ER drops to 0.05 fold/s (Figure 4.3b). We attribute this behavior to the limited amount of $BODIPY^{2-}$ available in the device (i.e., the limited sample volume).

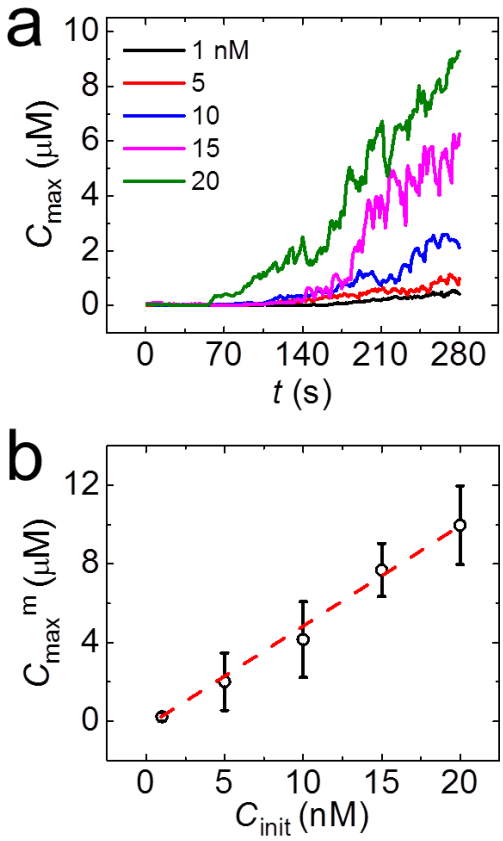

Figure 4.4. *C_{max} analysis.*
(a) Plots of C_{max} vs. t for the indicated values of C_{init}. The experimental conditions were the same as in Figure 4.3. (b) Plot of C_{max}^{m} vs. C_{init}. The values of C_{max}^{m} were obtained from (a) and Figure 4.5. Error bars indicate the standard deviation from three independent measurements. The dashed line represents the best linear fit to the data points.

Figure 4.4a shows how the C_{max} vs. t curves change for different values of C_{init}. These concentration-dependent data are consistent with the results shown in Figure 4.2c for a single BODIPY^{2-} concentration (20 nM) in that they rise monotonically with t. Note, however, that we have occasionally observed cases in which C_{max} reaches a maximum value and then decreases (Figure 4.5). This precipitous drop in C_{max} before the end of the experiment is a consequence of gas bubbles that occasionally form within the channel of the hyPAD and disrupt enrichment (Figure 4.6).

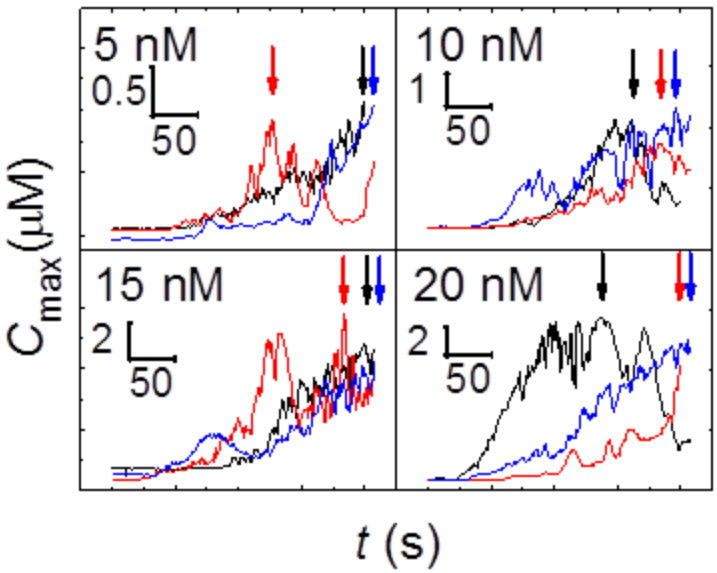

Figure 4.5. *Plots of C_{max} vs. t for different C_{init}. The experimental conditions are same as in Figure 4.4. The values of C_{max}^{m} are highlighted by arrows, and the values of C_{init} are shown in each frame.*

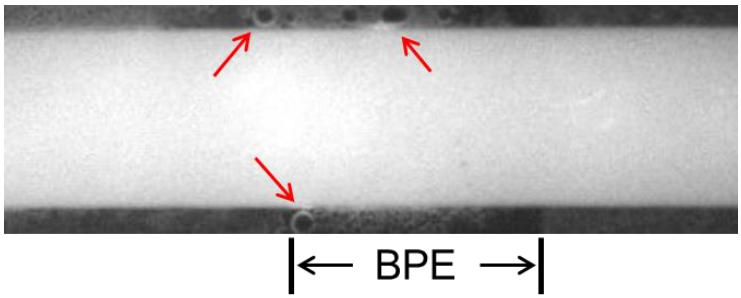

Figure 4.6. *A photograph of the hyPAD channel during an fICP experiment.*
The experimental conditions are the same as in Figure 4.2. Gas bubbles can be observed along the walls (highlighted with red arrows).

Despite the high level of noise and occasional drop in the C_{max} vs. t curves, C_{max}^{m} (the maximum value of C_{max} determined from Figures 4.4a and 4.5) is linearly correlated to C_{init} (Figure 4.4b). The slope of this plot is 513, which represents the average EF_{max} for the different values of C_{init}.

4.4.3 Understanding the fICP Mechanism in hyPADs

In an effort to better understand the fICP mechanism, we examined a number of parameters associated with its performance. Because faradaic reactions occurring at the BPE are essential for establishing the IDZ, this part of the study began with measurements of the current passing through BPE. It has previously been reported that as much as ~80% of the total current is diverted through the BPE in a conventional microfluidic channel.[147] To compare these earlier results to the hyPAD, ammeters were used to track

the current passing through the BPE and the total current through the channel (Illustration 4.3).

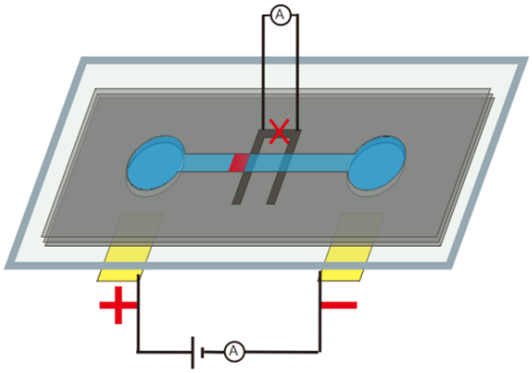

Illustration 4.3. *Schematic illustration of BPE current measurement.*
Current through the BPE is measured by cutting the connection between the two poles of the BPE (red X) and inserting an ammeter to complete the circuit. Current through the channel is measured by inserting an ammeter in series with the power supply.

The results of this experiment (Figure 4.7a) indicate that 91 ± 1 % of the total current passes through BPE, which corresponds to a current density of ~10 mA/cm^2. This is a sufficiently high current density that gas bubbles could be produced at the BPE.[148] This is consistent with the visual observation of bubbles in Figure 4.6 and our contention that these bubbles play a role in the occasional unusual enrichment profiles shown in Figure 4.5.

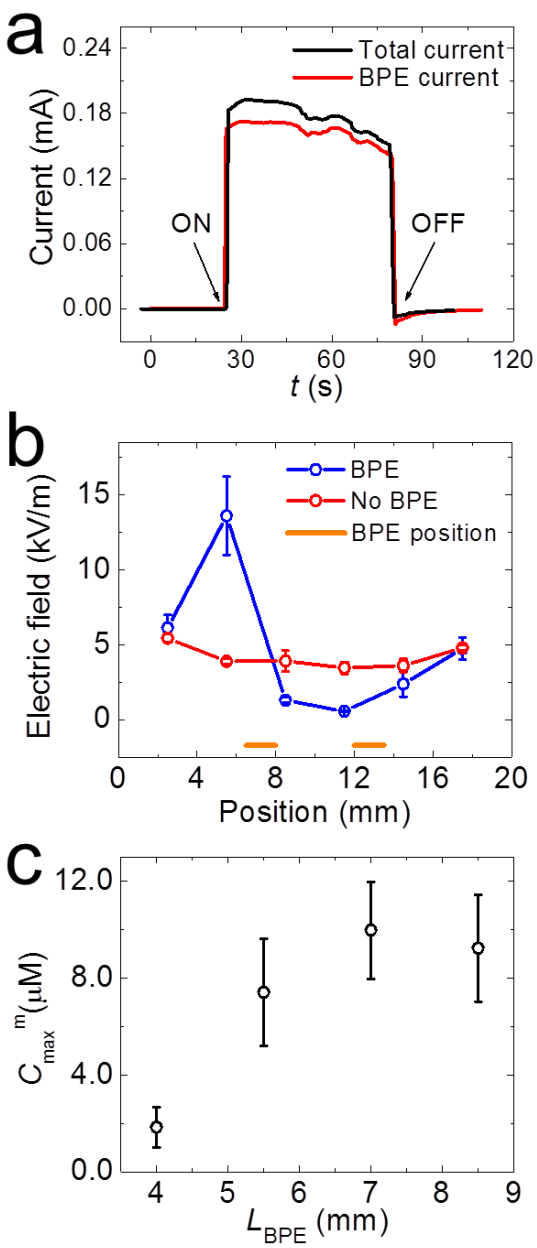

Figure 4.7. *Results obtained during BODIPY^{2-} enrichment experiments.*

(a) Plots of total current and BPE current vs. time obtained using experimental arrangement shown in Illustration 4.3. The driving voltage (E_{tot} = 100 V) was turned on and off at the times indicated by black arrows. Other experimental conditions are same as in Figure 4.2. (b) Electric field measurements obtained using the modified four-layer hyPAD illustrated in Illustration 4.4. Other experimental conditions are same as in Figure 4.2. The blue and red traces shows the electric field distribution when BPE is present and absent, respectively. The orange bars at the bottom of the figure indicate the locations of BPE cathode and anode. (c) Plot of C_{max}^{m} vs. BPE length (L_{BPE}). The data were obtained using hyPADs with L_{BPE} ranging from 4.0 mm to 8.5 mm. Other experimental conditions are the same as in Figure 4.2. The value of C_{max}^{m} was analyzed as in Figure 4.4. The error bars in (b) and (c) represent standard deviations obtained from three independent measurements like the one shown in (a).

Figure 4.7. continued.

A fundamental requirement for analyte enrichment by fICP is generation of a local electric field gradient within the fluidic channel.[127] The existence of this field is strongly suggested by the presence of the IDZ discussed in the context of Figure 4.3c, but we wanted to confirm it directly. Accordingly, a modified version of the hyPAD was used to measure this field during enrichment. This device, shown in Illustration 4.4, incorporates a fourth paper layer patterned with multiple electrodes evenly distributed above the channel. The local electric field strength along the channel can then be obtained by measuring the voltage difference between pairs of these electrodes during operation. When the BPE is absent, the results indicate that the electric field is uniformly distributed across the channel (~5 kV/m, Figure 4.7b). In contrast, when a BPE is present, a ~3-fold increase in the local electric field (~15 kV/m) is observed near the edge of the BPE cathode where analyte enrichment is observed (Figure 4.2a). In other words, the locations of the IDZ, the local electric field gradient, and the enrichment zone are more-or-less co-located. Another interesting observation from Figure 4.7b is that the electric field in the area between the poles of the BPE is close to zero. Recall that the current flowing through the channel accounts for only ~9% of the total current, which accounts for this observation.

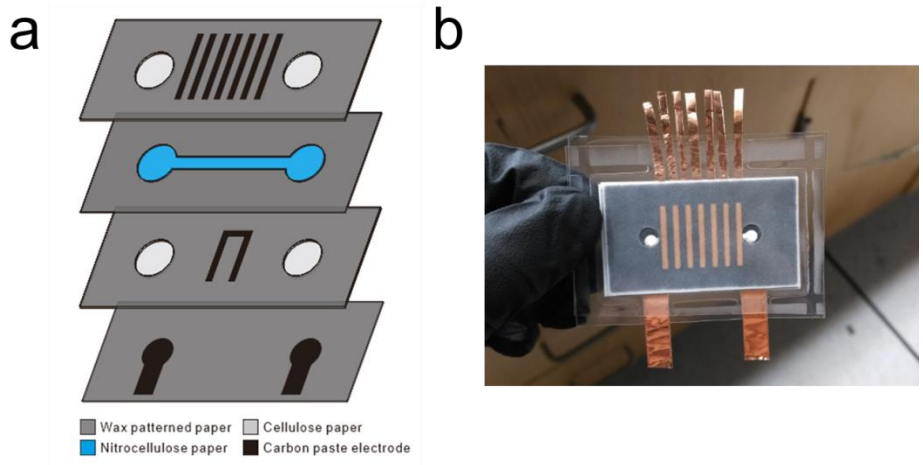

Illustration 4.4. *Design of the hyPAD for electric field measurement.*
(a) A schematic illustration of the hyPAD design for electric field measurement. Note that a fourth paper layer that is patterned with seven evenly distributed 1 mm-wide carbon electrode bands has been added. The center-to-center distance between the electrodes is 3 mm. During operation of the hyPAD, the voltage differences between pairs of bands, measured with a digital multimeter, indicate the electric field in the corresponding region of the channel (voltage difference divided by the distance between electrodes). (b) A photograph of the hyPAD. The device was laminated with clear plastic and the electrode bands were attached to copper tape.

We also examined the effect of the length of the BPE (L_{BPE}) on the performance of the hyPAD. This is an important parameter, because the potential difference between the two poles of the BPE (E_{BPE}), and hence the rate of the faradaic reaction, depends approximately on L_{BPE} and E_{tot} according to eq 4.4, where $L_{channel}$ is the length of the channel.[128]

$$E_{BPE} = E_{tot} \times \frac{L_{BPE}}{L_{channel}} \qquad (4.4)$$

Eq 4.4 indicates that if E_{tot} and $L_{channel}$ are held constant, then a larger value of L_{BPE} results in higher E_{BPE}.[147]

Therefore, by fabricating hyPADs with L_{BPE} ranging from 4.0 mm to 8.5 mm, it is possible to determine the effect of E_{BPE} on enrichment. Specifically, we determined the effect of L_{BPE} on C_{max}^{m}, and found that there is a positive correlation (Figure 4.7c): BPEs having longer lengths, up to 7 mm, lead to higher C_{max}^{m}. The increase in C_{max}^{m} is likely caused by an increased rate of water reduction, leading to faster formation of the IDZ. C_{max}^{m} does not continue to increase when L_{BPE} > 7.0 mm (which corresponds to E_{BPE} > 26 V), possibly due to bubble generation. Accordingly, we settled on L_{BPE} = 7.0 mm as the optimum BPE length for the experiments described in the next section.

4.4.4 Enrichment of DNA, Proteins, and AuNPs Using hyPADs

To demonstrate the scope of hyPAD applications, we examined the enrichment of DNA, proteins, and AuNPs. For the enrichment of DNA, a solution containing 20 nM DNA-Cy5 was placed into the inlet of a hyPAD, E_{tot} = 100 V was applied, and then the enrichment process was imaged by fluorescence microscopy. The resulting images are shown in Figure 4.8a. As for $BODIPY^{2-}$, DNA-Cy5 enriches just above the BPE cathode. A quantitative analysis of these results is provided in Figure 4.9a, where C_{ave} and C_{max} are plotted as a function of t. As discussed for $BODIPY^{2-}$ (Figure 4.2b), the

C_{ave} vs. t curve remains close to zero for the first 50 s, then increases nearly linearly, and finally plateaus. The C_{max} vs. t curve is somewhat noisy (probably due to bubble formation), but from the value of C_{max}^{m} we easily calculate that EF_{max} = 264.

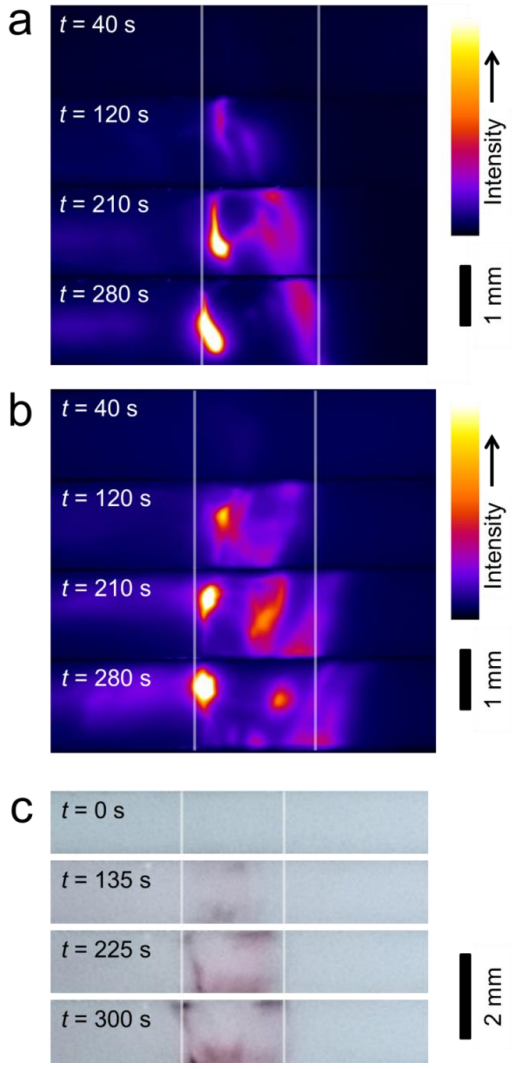

Figure 4.8. *Enrichment of DNA-Cy5, BSA-AF, and AuNPs using hyPADs.*
(a) Fluorescence micrographs obtained for DNA-Cy5 enrichment as a function of time. The initial DNA-Cy5 concentration was 20 nM, but the other experimental conditions were the same as in Figure 4.2. (b) Fluorescence micrographs obtained for BSA-AF enrichment as a function of time. The initial BSA-AF concentration was 10 nM, but the other experimental conditions were the same as in Figure 4.2. (c) Cell phone photographs obtained for AuNP enrichment as a function of time. The initial concentration of DNA-stabilized AuNPs was 1.0 nM, but other experimental conditions were the same as in Figure 4.2. In all three frames, the horizontal gray lines represent the edges of BPE cathode.

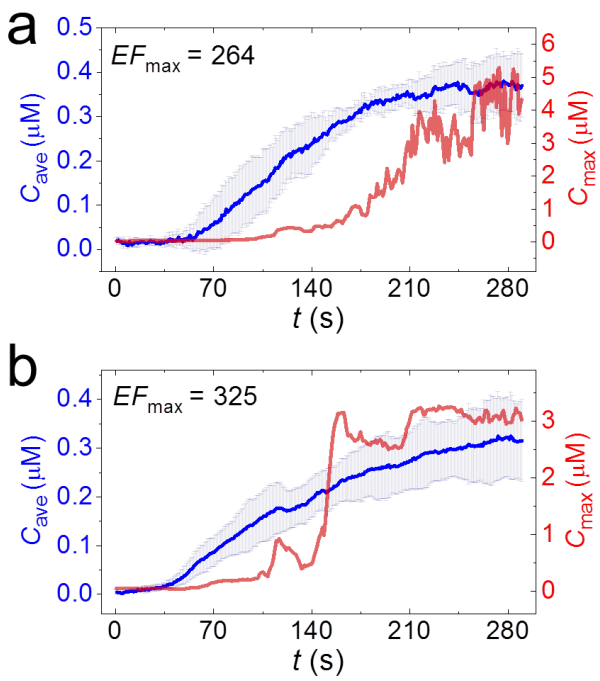

Figure 4.9. *Quantification of DNA-Cy5 and BSA-AF enrichment on hyPADs.*
(a) C_{ave} *and* C_{max} *vs.* t *traces for DNA-Cy5 enrichment. The concentration data were obtained using fluorescence micrographs like those shown in Figure 4.8a and comparing intensities to the DNA-Cy5 calibration curve in Figure 4.1b. The error bars represent the standard deviation of data obtained from three independent experiments.* EF_{max} *= 264 at* t *= 5 min. (b)* C_{ave} *and* C_{max} *vs.* t *traces for BSA-AF enrichment. The concentration data were obtained using fluorescence micrographs like those shown in Figure 4.8b and comparing intensities to DNA-Cy5 calibration curve in Figure 4.1c. The error bars represent the standard deviation of data obtained from three independent experiments.* EF_{max} *= 325 at* t *= 5 min.*

The enrichment of a 10 nM solution of BSA-AF is represented by the fluorescence micrographs shown in Figure 4.8b. The experimental conditions for this experiment were the same as for DNA-Cy5 enrichment. As for $BODIPY^{2-}$ *and DNA-Cy5, BSA-AF is enriched at a location just above the BPE*

cathode. Plots of C_{ave} and C_{max} as a function of t for this experiment are shown in Figure 4.9b. The characteristics of these data are similar to those of DNA-Cy5, but the value of EF_{max} is a little higher (325 vs. 264).

Interestingly, both DNA-Cy5 and BSA-AF are enriched at a location similar to that of $BODIPY^{2-}$, even though the three molecules have different electrophoretic mobilities.[97,135] This behavior is different from results in conventional ICP or fICP, where molecules having different electrophoretic mobilities concentrate at different locations.[88,137] This unique behavior is probably a result of the large channel dimensions of the hyPAD.

One final point regarding the fluorescence micrographs shown for DNA-Cy5 and BSA-AF: The region of the channel over which these analytes are enriched is significantly larger than for $BODIPY^{2-}$. We suspect this is because the electrophoretic mobilities of DNA-Cy5 and BSA-AF are lower than $BODIPY^{2-}$.[97,135] As a result, electromigration in the IDZ, which is proportional to electrophoretic mobility, may be insufficiently strong to completely stop the movement of DNA-Cy5 or BSA-AF (i.e., imperfect counter-flow forces). Therefore, some DNA-Cy5 and BSA-AF passes through IDZ and spreads over the BPE cathode.

Colorimetric assays based on AuNP labels are becoming commonplace due to their low cost and ability to be observed

by simple visual inspection.[21] However, the electrokinetic enrichment of nanoparticles on paper is challenging, because in paper matrixes electrophoretic transport of nanoparticles is usually much slower than small molecules.[149] However, the EOF of hyPADs can be strong enough to transport AuNPs efficiently in the paper channel. Herein, we tested the ability of hyPADs to concentrate AuNPs and imaged the enrichment process using a cell phone camera.

For this experiment, the sample solution contained 1.0 nM AuNPs, but otherwise the experimental conditions were the same as for Figure 4.2. To avoid aggregation in the relatively high salt solutions required for fICP, the AuNPs were functionalized with DNA using a pH-assisted method reported elsewhere.[145,150] These materials were prepared by mixing 500 μL of a solution containing 20 nm-diameter AuNPs with thiolated ssDNA (ssDNA-SH) at a molar ratio of 1:1000. The mixture was vortexed for 3 min, and then 50 μL of 100 mM citrate-HCl buffer (pH 3.0) was added. This mixture was vortexed for 3 min, and then 500 μL of a solution containing 100 mM HEPES (4-(2-hydroxyethyl)-1-piperazineethanesulfonic acid) buffer (pH 7.6) was added to bring the solution pH back to neutral. The AuNPs were washed with 100 mM Tris-HClO4 buffer (pH 8.1) three times, with centrifugation between washings, to obtain the final product. A cell phone

was used to track enrichment of AuNPs as a function of time under nearly identical lighting conditions.

Figure 4.8c presents photographs of AuNPs concentrating on a hyPAD as a function of time. Even with this primitive imaging technology, it is obvious that AuNPs, like the other analytes, accumulate near the BPE cathode. The purple color of the AuNPs does not change during the experiment, indicating they are stable (no aggregation) throughout the enrichment process. As for DNA-Cy5 and BSA-AF, the enriched AuNP region is broader than for $BODIPY^{2-}$. This finding is consistent with the hypothesis discussed earlier that electromigration in the IDZ may be not strong enough to completely slow down the movement of AuNPs due to their low electrophoretic mobility.[149]

4.5 Summary and Conclusions

To summarize, we have demonstrated enrichment of four analytes, $BODIPY^{2-}$, DNA-Cy5, BSA-AF, and AuNPs, using fICP implemented on a hybrid (cellulose and nitrocellulose) paper analytical device. The hyPAD is inexpensive and easy to fabricate, and the throughput is two-orders of magnitude higher than that of conventional microfluidic devices.

We carried out several experiments to provide insights into the performance and operating characteristics of the

hyPAD performance. Specifically, time-dependent enrichment studies indicated that no analyte accumulation occurs until ~50 s after application of the driving voltage. During this period, substantial current (91 ± 1 % of the total) is driven through the BPE, rather than the channel, resulting in formation of the IDZ. Electric field mapping reveals that enrichment is driven by the IDZ and the corresponding local electric field gradient at the edge of BPE cathode. Finally, we demonstrated the versatility of hyPADs by concentrating BODIPY^{2-} (EF_{max} = 490), DNA (EF_{max} = 264 fold), proteins (EF_{max} = 325 fold), and AuNPs (naked eye detection). This broad scope of analytes suggests that the hyPAD is a good candidate for coupling to conventional PADs to lower limits of detection.

*Chapter 5: Detection of Hepatitis B Virus DNA with a Paper Electrochemical Sensor**

5.1 Synopsis

Here we show that a simple paper-based electrochemical sensor, fabricated by paper folding, is able to detect a 30-base nucleotide sequence characteristic of DNA from the hepatitis B virus (HBV) with a detection limit of 85 pM. This device is based on design principles we have reported previously for detecting proteins via a metalloimmunoassay. It has four desirable attributes. First, its design combines simple origami (paper folding) assembly, the open structure of a hollow-channel paper analytical device to accommodate micron-scale particles, and a convenient slip layer for timing incubation steps. Second, two stages of amplification are achieved: silver nanoparticle labels provide a maximum amplification factor of 250,000 and magnetic microbeads, which are mobile solid-phase supports for the capture probes, are concentrated at a detection electrode and provide an additional ~25-fold amplification. Third, there are no enzymes or antibodies used in the assay, thereby increasing its speed, stability, and robustness. Fourth,

---

* *Chapter 5 is based on previous publication: X. Li, K. Scida and R. M. Crooks, Detection of Hepatitis B Virus DNA with a Paper Electrochemical Sensor, Anal. Chem., 2015, 87, 9009-9015. XL and RMC designed the experiments. RMC was the research advisor. XL performed and analyzed the experiments. KS provided suggestions. XL and RMC wrote the manuscript.*

only a single sample incubation step is required before detection is initiated.

5.2 Introduction

In this paper we show that a simple paper-based electrochemical sensor, fabricated by paper folding, is able to detect DNA from the hepatitis B virus (HBV) with a detection limit of 85 pM. This device, which we called oSlip-DNA (o stands for origami,[12] slip indicates that it incorporates a slip layer,[43,98] and DNA means that it is configured for DNA detection)[57], is based on design principles we have reported previously for detecting proteins via a metalloimmunoassay.[57,151] The oSlip-DNA has four desirable attributes. First, its design combines simple origami (paper folding) assembly,[12] the open structure of a hollow-channel paper analytical device to accommodate micron-scale particles,[44] and a convenient component (the slip layer) for timing incubation steps.[43,152] Second, two stages of amplification are achieved in the oSlip-DNA: (1) silver nanoparticle labels (AgNPs, 20 nm diameter, ~250,000 atoms per AgNP) provide a maximum amplification factor of 250,000; and (2) magnetic microbeads (MμBs), which are mobile solid-phase supports for the capture probes, are concentrated at a detection electrode, lead to an additional

~25-fold amplification. Third, there are no enzymes or antibodies used in the assay, thereby increasing its speed, stability, and robustness. Fourth, only a single sample incubation step is required before detection is initiated, thereby simplifying sample preparation. Here, we illustrate these basic concepts by demonstrating detection of a 30-base nucleotide sequence characteristic of HBV.[153]

HBV infection is one of the most important chronic virus infections with more than 350 million people infected worldwide.[154] *It can result in many clinical problems, including liver cirrhosis and hepatocellular carcinoma.*[155,156] *The DNA from HBV, which is an important biomarker for HBV infection, can vary from a few to more than 109 copies/mL in serum, and it is usually detected in serum*[157] *or dried blood spots*[158] *by tests based on polymerase chain reaction (PCR).*[159,160] *These PCR assays are usually performed in centralized laboratory settings due to the specialized nature of the required equipment and personnel.*[161] *More recently, several types of biosensors have been developed to detect the HBV DNA, including patterned nanoarrays with surface-enhanced Raman scattering detection*[162] *and a gold nanorod-based fluorescence resonance energy transfer system.*[163] *However, these sensors suffer from either a long testing time (>30 min) or cost, which makes them less than ideal for point-of-care (POC)*

applications. The device we report here is intended to fill the need for a cheaper, more portable detection system.

Paper-based analytical devices (PADs) for POC applications were popularized as early as the mid-1960s.[164] For example, one of the most familiar applications of PADs that emerged from these early studies is the pregnancy test strip, which is based on a lateral flow immunoassay.[165] In the mid-2000s, the Whitesides group disrupted the lateral flow assay technology by introducing 2D and 3D PADs.[3,18,19] These were fabricated on filter paper using photoresist[18,102] or wax[20] to create fluidic channels. Capillary flow in such sensors is driven by the cellulose matrix,[166] and therefore no pump or external power supply is required. The low cost and ease of remediating filter paper makes it a good candidate for POC applications.[3,130,167] Finally, a number of detection methods, including colorimetry,[104,168] electrochemistry,[54,56,57,169] UV-vis,[103] Raman,[170,171] fluorescence,[77,97] electrochemiluminescence,[105,107] and mass spectrometry[172] have been successfully applied to PAD assays. Of these detection methods, electrochemical methods are perhaps the most useful,[51,60] because they are quantitative, lend themselves to miniaturization, have low power requirements, and require only simple detection instrumentation. Accordingly, we have focused on electrochemical detection in our sensor technologies.

Microbeads, particularly those having a magnetic core, are a mainstay of bioassay systems for three reasons. First, they generally have much higher total surface areas than macroscopic planar surfaces, and therefore they can support more receptors. Second, their mobility in solution decreases assay times by increasing the likelihood of encounters between targets and receptors. Third, washing steps are faster and easier because the beads can be separated from solution by a magnetic force. For these reasons, it seems natural that microbeads would be integrated into PADs as mobile solid-phase supports. However, there is a size incompatibility: the limited pore size of the cellulose matrix is poorly matched with the unhindered flow of micron-scale microbeads. We recently resolved this problem by introducing hollow-channel PADs,[44-46] in which the cellulose channel is physically removed. Because the thickness of the paper we use is about 180 µm, this leads to unhindered flow of microbeads.

Another key step in bioassays is precise timing of incubation and washing steps. For PADs, a number of strategies have been introduced for enabling these operations. These include: dissolvable barriers,[11] magnetic valves,[42] programmed disconnection,[173] and sequential reagent loading using multiple pathways.[40] We contributed to this functionality by introducing the SlipPAD, which is a device

that incorporates a moveable piece of paper that can be used to initiate on-chip chemical reactions at a defined times.[43,98] The SlipPAD is simply a paper version of the SlipChip concept first reported by the Ismagilov group.[98,152]

In the present chapter we combine hollow channels, the SlipPAD methodology, and electrochemical detection to provide a one-step, full sandwich, quantitative DNA assay for HBV. The limit of detection (LOD) is 85 pM, which is remarkable for a device having a cost of US$ 0.19 (not including reagents or a plastic holder). Moreover, the performance metrics (LOD, time-to-answer, and linear range) of the oSlip-DNA compare favorably with the same assay carried out in a conventional electrochemical cell. Importantly, the results reported here also demonstrate the ease with which the oSlip platform can be reconfigured. That is, our recently reported biotin/streptavidin assay[57] is converted into an oligonucleotide assay simply by changing the receptor and label recognition elements.

5.3 EXPERIMENTAL

5.3.1 Chemicals and Materials

Phosphate buffered saline (PBS) solution (containing 10.0 mM phosphate, 138.0 mM NaCl and 2.7 mM KCl, pH 7.4) and $KMnO_4$ were purchased from Sigma-Aldrich (St. Louis, MO).

Label DNA (5` thiol-modified C6-S-S-A10-TACCACATCATCCAT 3`), the HBV DNA target (5` TTGGCTTTCAGTTATATGGATGATGTGGTA 3`), and capture DNA (5` ATAACTGAAAGCCAA-A10-Biotin 3`) were from Integrated DNA Technologies (Coralville, IA) and purified by HPLC. HCl, sodium citrate dihydrate, 4-(2-hydroxyethyl)-1-piperazineethanesulfonic acid (HEPES), NaOH, and Whatman grade 1 chromatography paper (180 µm thick) were obtained from Fisher Scientific (Walthman, MA). AgNPs (20 nm diam.) were from Ted Pella (Redding, CA). Streptavidin-coated MµBs (2.8 µm diam.) were from Bangs Laboratories (Fishers, IN). Erioglaucine disodium salt was acquired from Acros Organics (Pittsburgh, PA). Carbon ink for the screen-printed electrodes (SPEs) was from Engineered Conductive Materials (Delaware, OH). The neodymium cylindrical magnet (N48, 1/16 in. X 1/2 in.) was purchased from Apex Magnets (Petersburg, WV). All solutions were prepared using deionized water (DI, >18.0 MΩ•cm) purified by a Milli-Q Gradient System (Bedford, MA).

5.3.2 Device Fabrication

The oSlip fabrication method has been reported previously, and to demonstrate its ease of reconfigurability we used the same approach for the oSlip-DNA.[57] *Briefly, as shown in the Illustrations 5.1 and 5.2, the oSlip-DNA device pattern was designed in CorelDRAW software and printed on*

Whatman grade 1 chromatography paper using a wax printer (Xerox ColorQube 8570DN). The patterned paper sheet was placed in an oven at 120 ^{o}C for 45 s to melt the wax so that it penetrated through the thickness of the paper. After cooling to 25 ± 2 ^{o}C, the hollow channel was cut into the paper using a razor blade. The three electrodes were then added by stencil printing.[169] A binder clip with copper tape on it (Illustration 5.2) was used to connect the screen-printed electrodes to a potentiostat. Before use, 1.0 µL of 1.0 mM erioglaucine solution was drop-cast onto the outlet on the second layer of the device. As discussed later, this makes it possible to know when flow through the channel stops. Finally, the oSlip-DNA was sandwiched between two acrylic plates (Evonik Industries) and secured with binder clips to reproducibly compress the device and ensure uniform thickness of the hollow channel.

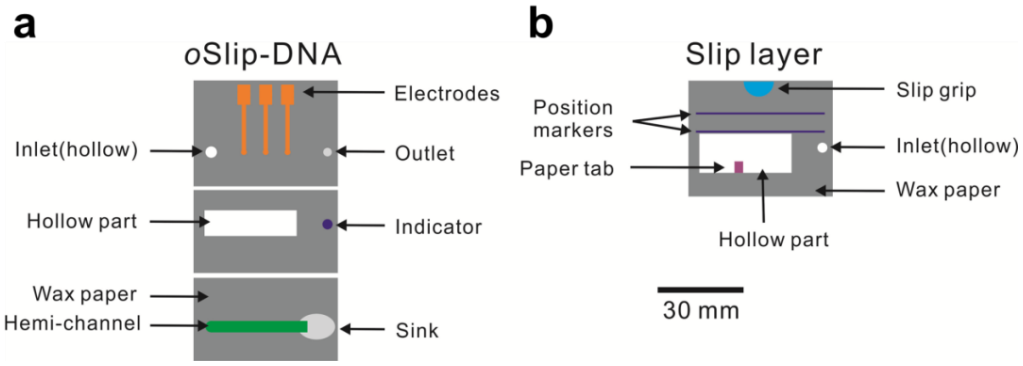

Illustration 5.1. *Design of the oSlip-DNA device. (a) The oSlip part of the device. (b) The slip layer part of the device. The scale bar applies to both figures. The hollow part of the device was cut out using a razor blade. Position markers in (b) mark the two slip position shown in Figures 5.2b and 5.2c.*

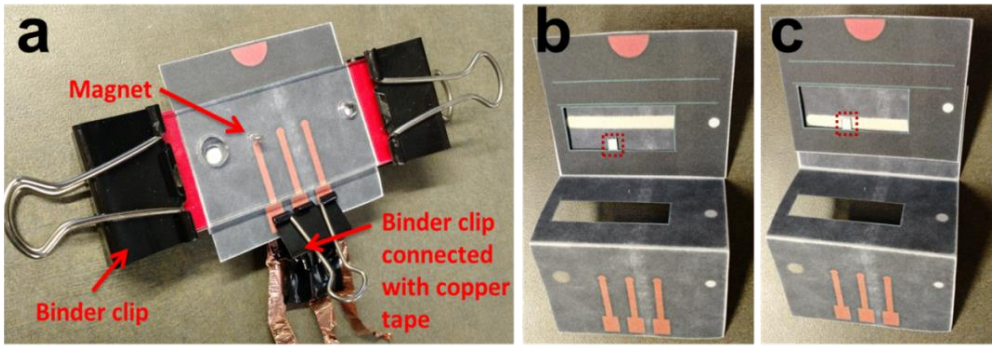

Illustration 5.2. *Photographs of the oSlip-DNA device. (a) The assembled oSlip-DNA device. (b) An open view of the device showing the slip-layer in its position prior to introduction of $KMnO_4$ to the hollow channel. The tab impregnated with $KMnO_4$ is highlighted by the dashed red square. (c) An open view of the device after moving the slip layer into its functional position with the tab in the hollow channel.*

5.3.3 Modification of AgNPs and MμBs with DNA

AgNPs modified with label DNA were synthesized using a fast pH-assisted functionalization method first reported by Liu and coworkers.[174,175] A 500.0 μL stock solution of AgNPs (565.0 pM in DI H_2O) was mixed with thiolated DNA at a molar ratio of 1:1000. The mixture was placed on a vortexer for 5.0 min. Next, 26.5 μL of 100.0 mM pH 3.0 citrate-HCl buffer was added to the solution to bring the salt concentration up to 5.0 mM. The solution was vortexed for an additional 5.0 min before adding another 27.8 μL of citrate-HCl buffer to reach a final salt concentration of 10.0 mM. After 25.0 min, 500.0 μL of 100.0 mM pH 7.6 HEPES buffer was added to bring the solution pH back to neutral pH. The label DNA-modified AgNPs were then centrifuged (20.0 min at 16,000 g) and washed three times with 1x PBS buffer (pH 7.4) to obtain the final product. The resulting AgNPs were characterized by UV-vis spectroscopy (Hewlett-Packard HP 8453 spectrometer), zeta potential measurements (Nanosight NS500), and transmission electron microscopy (JEOL 2010F TEM).

Capture DNA immobilization on MμBs takes advantage of biotin/streptavidin conjugation. Briefly, surfactant was removed from a stock solution containing 1.1 pM streptavidin-coated MμBs by washing twice with 1x PBS buffer, and then the MμBs were mixed with biotinylated DNA at a molar ratio of 1:106. After reaction at 25 ± 2 ^{o}C for

1.0 h, the resulting DNA-modified MμBs were washed with 1x PBS buffer three times to remove unbound DNA.

5.3.4 Electrochemistry

All electrochemical measurements were performed using a CHI 650C potentiostat from CH Instruments (Austin, TX). A glassy carbon working electrode (GCE, 1.0 mm diam.), Ag/AgCl reference electrode, and Pt wire counter electrode were used for testing the DNA assay in a conventional electrochemical cell (Illustration 5.3). For the oSlip-DNA device, all three electrodes were 2.0 mm in diameter and fabricated by stencil printing. The reference electrode was, therefore, a carbon quasi-reference electrodes (CQRE), which holds a surprisingly stable potential for the duration of oSlip-DNA. assays.

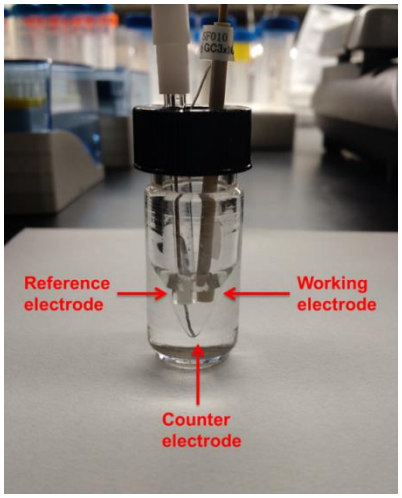

Illustration 5.3. *Photograph of the conventional electrochemical cell.*
A glassy carbon working electrode (GCE, 1.0 mm diam.), Ag/AgCl reference electrode, and Pt wire counter electrode were used for electrochemical measurements. The volume of solution in the cell was 250.0 µL.

5.4 Results and Discussion

5.4.1 Operation of the oSlip-DNA

In this section we explain the operation of the oSlip-DNA, including the one-step sample incubation procedure and anodic stripping voltammetry (ASV) detection method.

The three-strand DNA sandwich, which links together the AgNP labels and MµB solid supports, was carried out in a vial (i.e., off chip). Specifically, 50.0 µL of the HBV DNA target, present at different concentrations in 1x PBS buffer, was mixed with 10.0 µL of a 700 fM solution of the MµBs functionalized with the capture DNA and 10.0 µL of a

210.0 pM solution of AgNPs modified with the label DNA. After vortexing for 30.0 min, the mixture was washed twice using a magnet to retain the MμB-bound DNA sandwich. The DNA sandwich was then resuspended in 1x PBS buffer.

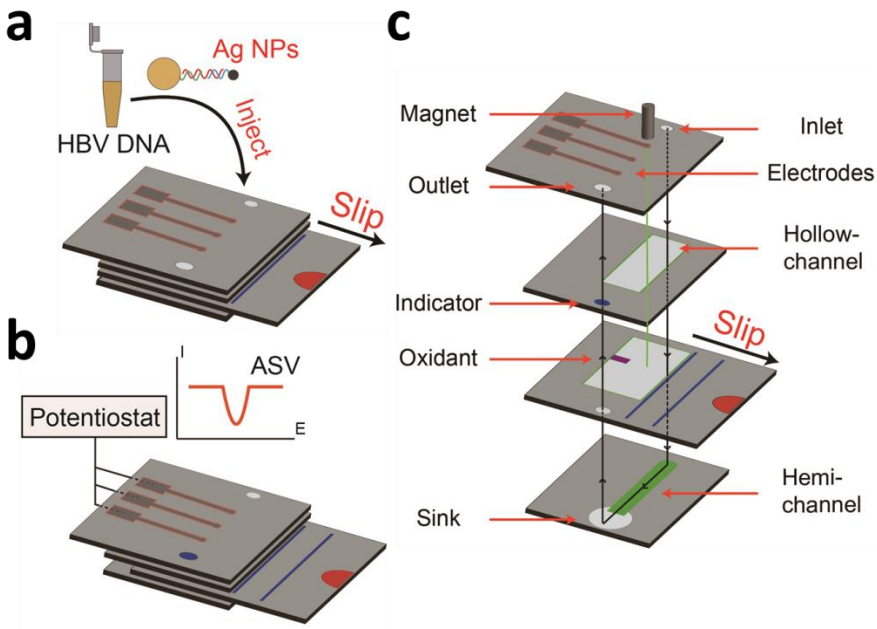

Illustration 5.4. *Scheme of the oSlip-DNA.*

The assay begins by injecting the DNA sandwich into the inlet of the oSlip-DNA (Illustration 5.4a). The bottom of the main channel is rendered hydrophilic (the green hemi-channel shown at the bottom of Illustration 5.4c),[45] *so the MμBs will flow through the hollow channel due to capillary pressure. A small rare-earth magnet is positioned just above the working electrode and held in place by a plastic holder (Illustration 5.2). Therefore, as the DNA sandwich moves down the channel, the MμBs are captured directly at the*

working electrode. This is an important preconcentration step that is, in part, responsible for the low LOD that characterizes the oSlip-DNA.

The channel and the sink at the end of the channel become saturated with solution within 15 s and flow stops. This results in upward flow of the solution toward the outlet, and this in turn leads to resolvation of the predispensed erioglaucine dye and the appearance of a blue color at the outlet of the oSlip-DNA. The appearance of the blue indicator means that flow has stopped and that the user should move the slip layer (the third layer) into its functional position (Illustration 5.4b). This results in 3.7 nmol of the oxidant ($KMnO_4$), which was predispensed onto a paper tab attached to the slip layer, being carried into the region of the channel directly below the working electrode. The solid $KMnO_4$ resolvates and diffuses through the ~180 µm thickness of the quiescent solution in the hollow channel within 20 s. This results in rapid oxidation of the AgNP labels by MnO_4^- to yield soluble Ag^+.

The final step in the assay is to electrodeposit the free Ag^+ onto the working electrode, and then quantify the amount of zerovalent Ag by ASV. Because Ag^+ is confined within the narrow channel, the majority of it can be deposited onto the working electrode within 200 s. Each AgNP contains ~250,000 Ag atoms, and so this is the second source

of chemical amplification that leads to low picomolar LODs. The entire analysis takes <5 min.

5.4.2 Characterization of DNA-modified AgNPs and MμBs

It is not possible to directly measure the average number of oligonucleotides per AgNP using UV-vis spectroscopy, because the large AgNP plasmon peak at 400 nm overlaps the much smaller DNA absorbance at 260 nm (which is typically used for quantitation). However, using a very similar synthetic method, Liu and coworkers used fluorescently labeled DNA to estimate that there are ~220 DNA strands per 20 nm AgNP.[174]

Although it is difficult to know the average number of DNA molecules per AgNP, we have abundant circumstantial evidence for its presence. For example, the stability of the AgNPs is enhanced after DNA modification. This is demonstrated by the UV-vis spectra of AgNPs before and after modification with DNA (Figure 5.1). Before DNA modification, the AgNPs (diluted in DI H_2O) exhibit a large absorption peak at 400 nm, which is characteristic of the plasmon of individual AgNPs.[176,177] *After washing the AgNPs and dispersing in 1x PBS buffer, however, the 400 nm absorption peak disappears, indicating agglomeration and precipitation.*[178] *In contrast, after the AgNPs are modified with DNA, the 400 nm plasmon peak is still evident after*

washing and dispersing in the same buffer. This enhanced stability in the high-salt buffer is a consequence of the stabilizing influence of the DNA shell.[179]

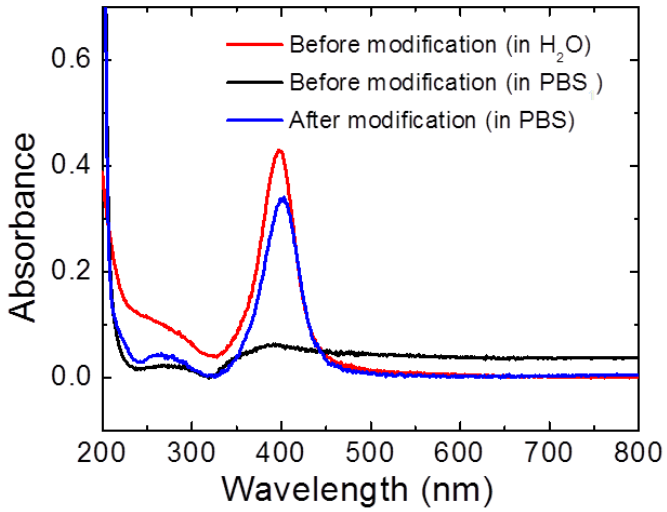

Figure 5.1. *UV-vis spectra of AgNPs.*
The red trace is the spectrum of unmodified AgNPs dispersed in DI H_2O. The peak at ~400 nm arises from the plasmon absorbance. The black trace is the spectrum after centrifuging the AgNPs (20.0 min at 16,000 g) and resuspending in 1x PBS buffer. In this case, the AgNPs agglomerate and precipitate, so no plasmon peak is observed. The blue trace is the spectrum of AgNPs in 1x PBS buffer after DNA modification. In this case, the AgNPs remain soluble due to the presence of the polyelectrolyte DNA shell. Taken together, these data provide circumstantial evidence for the presence of surface-bound DNA.

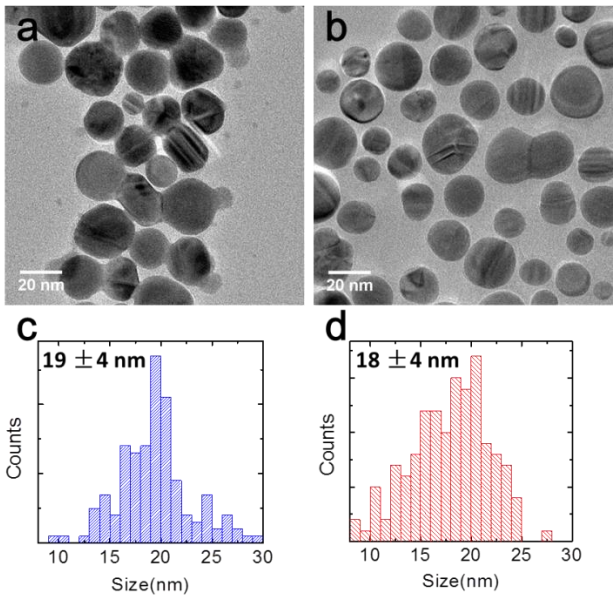

Figure 5.2. *AgNPs size analysis.*
Transmission electron micrographs and size distributions of AgNPs (a & c) before and (b & d) after surface modification with DNA.

Additional evidence for the DNA shell comes from nanoparticle tracking analysis. Specifically, the zeta potential of the AgNPs decreases from -19.69 mV to -40.19 mV after modification with DNA. The negative zeta potential before DNA modification is probably due to the citrate capping reagent used during the initial synthesis of the AgNPs. The transmission electron micrographs in Figure 5.2 show that the size of AgNPs does not change during DNA modification, but the dispersion of particles is better due to DNA-DNA repulsion between particles. These results are consistent with the zeta potential measurements and the

enhanced stability in salt solution, and together they strongly suggest the presence of DNA on the AgNPs.

It is easier to determine the amount of DNA on the 2.8 µm diam. MµBs than on the AgNPs. Specifically, we used UV-vis spectroscopy to determine the difference in DNA concentration in the supernatant before and after reaction with streptavidin coated MµBs, which corresponds to the amount of DNA strands present on MµBs. The results show that there are 4.1 ± 0.7 x 10^5 DNA strands per MµB.

5.4.3 DNA Sandwich Assay in a Conventional Electrochemical Cell

To benchmark the performance of the oSlip-DNA, the HBV DNA sandwich assay was carried out using a conventional electrochemical cell first. These experiments also provided us with an opportunity to optimize some parameters that could transferred to the operation of the paper device.

Experiments in the conventional electrochemical cell were carried out as follows. Different concentrations of a 100.0 µL solution of the HBV DNA sandwich (see legend, Figure 5.3a), synthesized as described earlier, were added to a conventional electrochemical cell. Next, 1x PBS buffer (supporting electrolyte) and MnO_4^- (oxidant, 41.6 µM final concentration)[57] were added to yield a total volume of 250.0 µL. After 20 s, which is sufficient time for MnO_4^- to

completely oxidize the AgNPs, three electrodes were inserted into the cell. Finally, the potential of the carbon working electrode was set to 0.30 V for 200 s, to electrodeposit Ag, and then ASV was initiated by scanning from -0.06 V to 0.30 V at 10 mV/s. As shown in Figure 5.3a, Ag oxidation occurs at ~0.13 V.

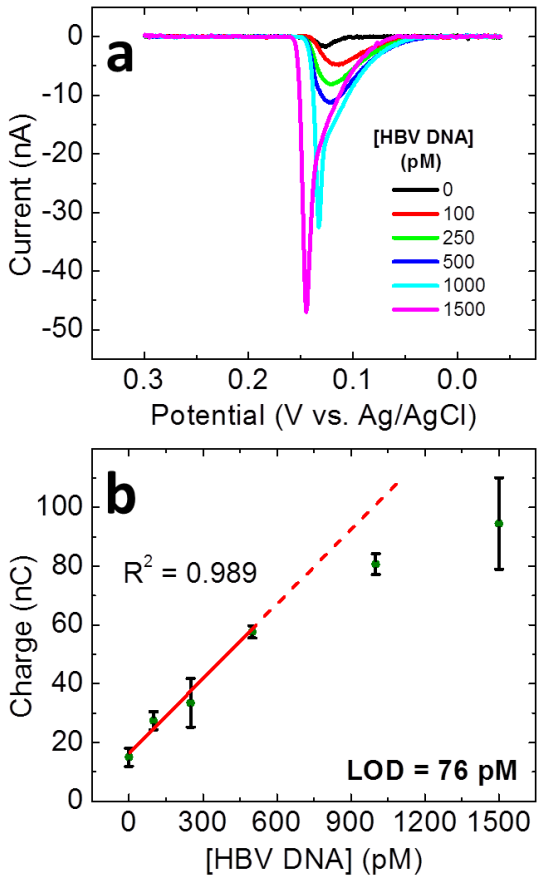

Figure 5.3. *DNA assay in a conventional electrochemical cell.*
(a) ASVs obtained for the HBV DNA sandwich assay in a conventional electrochemical cell. Different concentrations of the HBV DNA target were mixed with 100 fM MμBs and 30.0 pM AgNPs in 1x PBS buffer for 30.0 min to form the DNA sandwich. Next, the DNA sandwich was added to a 1x PBS solution containing 41.6 μM $KMnO_4$. The ASVs of this solution were obtained by holding the potential of the working electrode at -0.30 V (vs. Ag/AgCl) for 200 s, and then scanning from -0.06 V to 0.30 V at 10 mV/s. The data shown here has been baseline corrected. (b) Plot of charge under the ASVs shown in (a) as a function of the concentration of the HBV DNA target. The red line represents the best linear fit of the experimental data. The error bars reflect the standard deviations for replicate measurements carried out in three independently fabricated devices.

The areas under the voltammograms in Figure 5.3a were integrated to determine the charge corresponding to Ag electrodeposited on the working electrode, and the resulting dose-response curve is plotted in Figure 5.3b. The plot is linear between target DNA concentrations ranging from 0 to 500 pM, but at higher concentrations the total charge collected is lower than predicted by the red line. This is probably due to the high-dose Hook effect, which is common in this type of one-step sandwich assay.[180] The non-zero intercept in the plot is a consequence of non-specific absorption of AgNPs on the MμBs. The LOD of the HBV DNA assay is 76 pM (i.e., 4.5 x 10^{10} DNA copies per mL), which is comparable to HBV DNA levels in the serum of patients before seroconversion.[181] This LOD is defined as three times the standard deviation of the blank signal, divided by the slope of dose-response curve in Figure 5.3b. Note that a control experiment was carried out using a target consisting of all T base single-stranded DNA (dT30). The result (Figure 5.4) indicates a 4-fold higher signal for the correct target compared to dT30. The signal for dT30 is 2-fold higher than for the control experiment (no target present, Figure 5.3a).

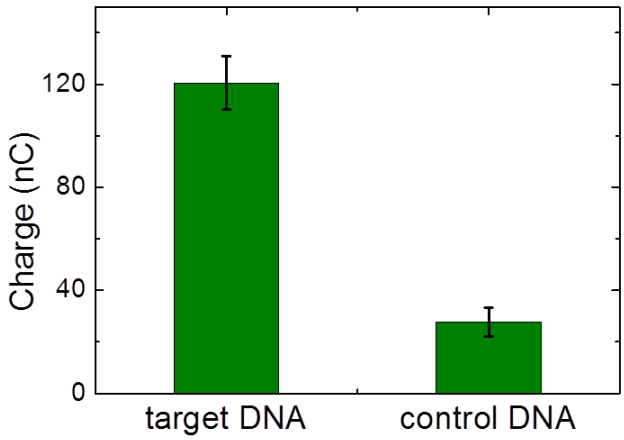

Figure 5.4. *Specificity test. Experiments for DNA assay was carried out in the conventional electrochemical cell. In both experiments, 1.0 nM DNA (target or control) was used. The concentrations of MμBs and AgNPs were 100 fM and 30.0 pM, respectively, and the allotted hybridization time was 3.0 h. Control DNA is all T base single-stranded DNA (dT30, Integrated DNA Technologies). The electrochemistry parameters are same as in Figure 5.3. Values of the charge shown in the figure come from integration of the Ag oxidation peak in the ASVs.*

After demonstrating the functionality of the sandwich assay, we turned our attention to optimizing three important experimental parameters to ensure the lowest possible LOD and efficient use of reagents. All of these experiments were carried out in the conventional electrochemical cell using the just-described procedure. First, the time required for DNA sandwich hybridization was studied. As shown in Figure 5.5a, the one-step sandwich reaction reached ~80% of its maximum signal at 30.0 min and plateaued thereafter, which is consistent with DNA binding kinetics under similar

conditions.[182] Accordingly, 30.0 min was chosen as the optimal DNA hybridization time. Second, the effect of the MμB concentration on the Ag oxidation signal was tested while maintaining a 30.0 min DNA sandwich incubation time. The results in Figure 5.5b show that a MμB concentration of 100 fM is sufficient to capture most of the HBV DNA target strands. Beyond this point, no signal enhancement is observed. Third, the effect of the concentration of DNA-modified AgNPs was examined using a 30.0 min incubation time and 100 fM MμB concentration. Figure 5.5c shows that the signal increases with increasing AgNP concentration, but no limiting value is achieved. The reason for this behavior goes back to the Hook effect. That is, there is an excess of capture DNA strands (on the MμBs) but limited label strands (on the AgNPs), and therefore target DNA can only form a half-sandwich by binding to available capture strands. The higher the concentration of AgNP (modified with label strands), the higher the chance of forming a complete sandwich and hence higher charge is observed. This argues for the use of higher AgNP concentrations, but to minimize non-specific absorption of the AgNPs onto the MμBs, and to minimize cost, a AgNP concentration of 30.0 pM was chosen for the oSlip-DNA experiments.

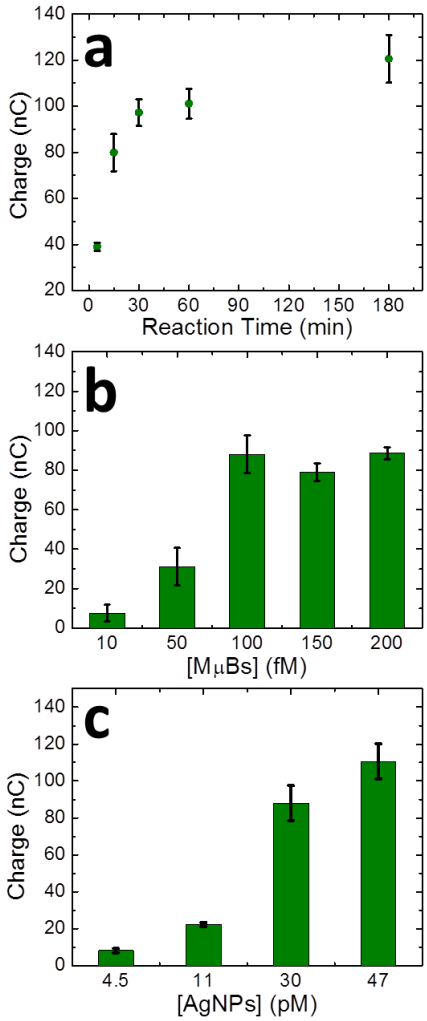

Figure 5.5. *Optimization of reaction time and reagent concentrations.*
All experiments were performed in 1x PBS buffer and the concentration of the HBV DNA target used was 1.0 nM. Electrochemical measurements were carried out as in Figure 5.3. (a) Plot of charge under the ASV peaks as a function of reaction time. The HBV DNA target was mixed with 200 fM MμBs and 47.0 pM AgNPs for the indicated times. (b) Plot of charge under the ASV peaks as a function of MμB concentration. The HBV DNA target was mixed with 47.0 pM AgNPs and the indicated concentrations of MμBs for 30.0 min. (c) Plot of charge under the ASV peaks as a function of AgNP concentration. The HBV DNA target was mixed with 100 fM MμBs and the indicated concentrations of AgNPs for 30.0 min.

5.4.4 DNA Sandwich Assay in the oSlip-DNA

Using the optimized parameters discussed in the previous section, we carried out a series of HBV DNA sandwich assays in the oSlip-DNA paper device. As for the experiments performed in the conventional electrochemical cell, 50.0 µL of the pre-synthesized DNA sandwich was injected into an oSlip-DNA device. As we have shown previously,[57] the magnet (Illustration 5.4c) concentrates the MµB-conjugated DNA sandwich on the surface of the working electrode. After ~12 s flow stops due to saturation of the paper sink, which is indicated by the appearance of the blue dye at the outlet. At this point the slip layer is pulled to expose the AgNPs to the oxidant for 20 s. Finally, electrochemical detection is initiated by electrodepositing Ag^+ at -0.3 V for 200 s, and carrying out ASV from -0.3 V to 0.3 V at 10 mV/s (in a preliminary report of the oSlip, we showed that these are the optimal values).[57]

The ASVs resulting from the foregoing procedure are shown in Figure 5.6a. Compared to the results obtained in the conventional electrochemical cell (Figure 5.3), there are two significant differences here. First, the potential range on the horizontal axis is different. This is because the oSlip uses a CQRE, which has a different potential than the Ag/AgCl reference electrode used to obtain the data in Figure 5.3a. Second, there is more variation in the Ag

oxidation peak position in Figure 5.6a than in Figure 5.3a. This is also a consequence of the different reference electrodes used in the two experiments. Specifically, each ASV shown in Figure 5.6a was obtained using an independently fabricated oSlip, and there is some device-to-device variation in the potentials of the CQREs. Although somewhat annoying, this is not too big of a problem because it is still easy to integrate the peaks due to the absence of other electrochemical processes in this potential range.

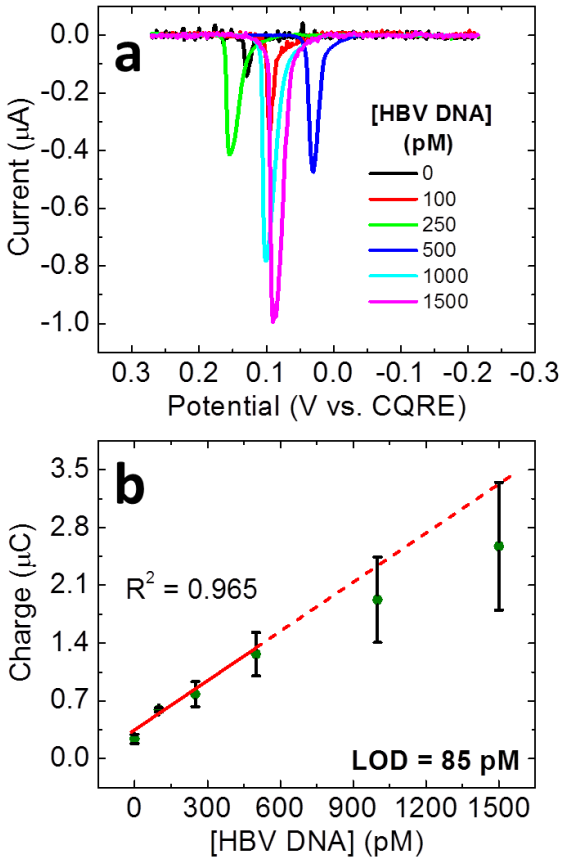

Figure 5.6. *DNA assay on oSlip-DNA devices. (a) ASVs obtained for the HBV DNA sandwich assay. The indicated concentrations of the HBV DNA target were mixed with 100 fM MμBs and 30.0 pM AgNPs in 1x PBS buffer for 30.0 min. The electrochemical data were obtained by electrodepositing Ag at a potential of -0.30 V for 200 s, and then scanning the potential from -0.30 V to 0.30 V at 10 mV/s. The data shown here has been baseline corrected. (b) Plot of charge under the ASVs shown in (a) as a function of the concentration of the HBV DNA target. The red line represents the best linear fit of the experimental data. The error bars reflect the standard deviations for replicate measurements carried out in three independently fabricated devices.*

Another important difference between the ASV results obtained in the conventional electrochemical cell (Figure 5.3a) and the oSlip-DNA (Figure 5.6a) is that the current is ~25 times higher in the paper device even though the experimental conditions are the same. We ascribe this difference primarily to the presence of the magnet above the working electrode (not present in the conventional electrochemical cell) and the concomitant accumulation of the MμB-bound AgNP labels. Additionally, there is an advantage to carrying out the Ag electrodeposition step in the oSlip due to its thinness and geometric corresponding confinement of Ag^+ near the working electrode.[57,183] *These factors represents the second level of amplification in the oSlip-DNA, the first being the 250,000-fold amplification of the sandwich due to oxidation of the AgNP labels. Note that in a preliminary report,*[57] *we showed that ~84% of the MμBs introduced into the inlet of the oSlip-DNA are captured by the magnetic field in the vicinity of the working electrode.*

Figure 5.6b is a plot of the charge under the ASV peaks in Figure 5.6a as a function of the concentration of HBV DNA. It exhibits a trend similar to that observed in the conventional electrochemical cell. That is, the ASV signal changes linearly with the HBV DNA concentrations ranging from 0 to 500 pM and presents a slight Hook effect at concentrations higher than 1.0 nM. As mentioned above, the

charge under ASV peaks are ~25 times larger than that in the conventional electrochemical cell. However, the effect of AgNP non-specific absorption on the MμBs also leads to a higher signal when no target is present. The LOD for the HBV DNA in the oSlip-DNA is 85 pM; about the same as in the conventional electrochemical cell (76 pM).

5.5 Summary and Conclusion

In conclusion, we have demonstrated the functionality of the oSlip-DNA for the detection of the HBV DNA using a one-step sandwich assay. The oSlip-DNA is user-friendly, capable of handling assays that employ MμBs, and its two-stage amplification makes it possible to detect picomolar levels of the HBV DNA target. The dynamic range and linear range are 0 - 1.5 nM and 0 - 500 pM, respectively, with a LOD of 85 pM. Each sensor costs < US$ 0.19 to fabricate at lab scale, the assay is fast (< 5 min) and robust compared to enzymatic amplification methods, making it a candidate for POC applications.

Still, there are some problems with the approach we described here. First, the DNA sandwich must be prepared ex situ, which for POC applications is not desirable. Accordingly, we are currently studying the feasibility of predispensing the MμBs functionalized with the capture

sequences and the DNA-functionalized AgNP labels in the inlet of the device. This introduces a new set of problems, including reagent resolvation, controlling the timing of the hybridization step, and issues related to non-specific adsorption. We are also interested in more realistic matrices (here we focused exclusively on buffer) and of course that introduces yet another set of challenges. Finally, the detection limit of the oSlip DNA for HBV is too high for direct assays. This means that some kind of nucleic acid preamplification, such as PCR, would be required for this particular HBV application. Note that it is not usual to couple off-chip PCR with PAD detection.[184] The results of our efforts to address these challenges will be reported in due course.

Chapter 6: Summary and Conclusion

In this dissertation, four types of paper-based analytical devices are described. The first device focuses on multi-analyte separation. The second and third devices are designed for sample enrichment. The fourth device is a sensitive biosensor with electrochemical detection.

Specifically, Chapter 2 discusses the design of a 3D PAD (oPAD-Ep) for electrophoretic separation of serum proteins. The oPAD-Ep is fabricated based on the principle of origami to shorten the channel length. The key finding is that only ~10 V voltage supply is enough to generate a sufficient electric field in the channel (a few kV/m) for electrophoresis, which avoids high voltage conditions in conventional designs. The multilayer design enables convenient sample introduction by the use of a slip layer as well as easy product analysis and reclamation, thus making the oPAD-Ep more user-friendly and suitable for POC applications.

Chapter 3 focuses on the sample enrichment based on the isotachophoresis technique. The device (called oPAD-ITP), similar to the oPAD-Ep (Chapter 2), is also based on the origami design. The electrolyte conditions in the channel are controlled so that sample ions transport at a velocity between two different electrolytes. The specific electrolyte condition leads to a non-linear electric field gradient in

the channel and a sharp electric field boundary between the two electrolytes. The key finding is that single-stranded and double-stranded DNA with various lengths (from 23 to 1517 bp) can be enriched at the boundary of the two electrolytes with similar enrichment factor (~100) and collection efficiency (~20%). This PAD design can be integrated with other detection systems and lower the limit of detections by two orders of magnitude.

Chapter 4 discusses the faradaic ion concentration polarization experiments for sample enrichment on paper (hyPAD). The hyPAD uses bipolar electrode based faradaic electrochemistry to create a local electric field gradient in the paper channel and concentrate charged anlaytes with a counter-flow. The key finding is that the hyPAD can be fabricated easily with low-cost materials and the enrichment process in hyPADs can be tuned via electrochemistry. Charged analytes including DNA, proteins, nanoparticles, can be enriched by 200-500 fold within 5 min.

Chapter 5 focuses on using an electrochemical method for the detection of DNA hybridization assays on paper (oSlip-DNA). The electrochemical method is sensitive, fast, and robust. The device is low-cost, user-friendly, and yet sophisticated enough to enable microbead-based assay and timely control of the reagent transport. The key finding is that this electrochemical method integrates two stages of

amplification: magnetic enrichment (~25 fold) and electrochemical signal amplification via silver nanoparticles (~250,000 fold). Therefore, the oSlip-DNA, which can be fabricated at a cost of 36 cents per device, is capable to detect Hepatitis B Virus DNA with a detection limit of 85 pM.

References

1. *Jiang, X.; Fan, Z. H. Fabrication and Operation of Paper-Based Analytical Devices. Annu. Rev. Anal. Chem.* **2016**.
2. *Cunningham, J. C.; DeGregory, P. R.; Crooks, R. M. New Functionalities for Paper-Based Sensors Lead to Simplified User Operation, Lower Limits of Detection, and New Applications. Annu. Rev. Anal. Chem.* **2016**, *9*, 183-202.
3. *Martinez, A. W.; Phillips, S. T.; Whitesides, G. M.; Carrilho, E. Diagnostics for the Developing World: Microfluidic Paper-Based Analytical Devices. Anal. Chem.* **2010**, *82*, 3-10.
4. *Tüd s, A. J.; Besselink, G. A.; Schasfoort, R. B. Trends in miniaturized total analysis systems for point-of-care testing in clinical chemistry. Lab Chip* **2001**, *1*, 83-95.
5. *Yager, P.; Domingo, G. J.; Gerdes, J. Point-of-care diagnostics for global health. Annu. Rev. Biomed. Eng.* **2008**, *10*, 107-144.
6. *Chin, C. D.; Linder, V.; Sia, S. K. Commercialization of microfluidic point-of-care diagnostic devices. Lab Chip* **2012**, *12*, 2118-2134.
7. *Yager, P.; Edwards, T.; Fu, E.; Helton, K.; Nelson, K.; Tam, M. R.; Weigl, B. H. Microfluidic diagnostic technologies for global public health. Nature* **2006**, *442*, 412-418.
8. *Gubala, V.; Harris, L. F.; Ricco, A. J.; Tan, M. X.; Williams, D. E. Point of care diagnostics: status and future. Anal. Chem.* **2011**, *84*, 487-515.

9. Gervais, L.; De Rooij, N.; Delamarche, E. Microfluidic chips for point-of-care immunodiagnostics. *Adv. Mater.* **2011**, *23*.
10. Yetisen, A. K.; Akram, M. S.; Lowe, C. R. Paper-based microfluidic point-of-care diagnostic devices. *Lab Chip* **2013**, *13*, 2210-2251.
11. Fu, E.; Lutz, B.; Kauffman, P.; Yager, P. Controlled reagent transport in disposable 2D paper networks. *Lab Chip* **2010**, *10*, 918-920.
12. Liu, H.; Crooks, R. M. Three-dimensional paper microfluidic devices assembled using the principles of origami. *J. Am. Chem. Soc.* **2011**, *133*, 17564-17566.
13. Wang, C.-C.; Hennek, J. W.; Ainla, A.; Kumar, A. A.; Lan, W.-J.; Im, J.; Smith, B. S.; Zhao, M.; Whitesides, G. M. A Paper-Based "Pop-up" Electrochemical Device for Analysis of Beta-Hydroxybutyrate. *Anal. Chem.* **2016**, *88*, 6326-6333.
14. Cheng, C. M.; Martinez, A. W.; Gong, J.; Mace, C. R.; Phillips, S. T.; Carrilho, E.; Mirica, K. A.; Whitesides, G. M. paper-based elisa. *Angew. Chem., Int. Ed.* **2010**, *49*, 4771-4774.
15. Müller, R.; Clegg, D. L. Automatic paper chromatography. *Anal. Chem.* **1949**, *21*, 1123-1125.
16. Wide, L.; Gemzell, C. A. An immunological pregnancy test. *Acta Endrocrinol.* **1960**, *35*, 261-267.
17. Matthews, D.; Bown, E.; Watson, A.; Holman, R.; Steemson, J.; Hughes, S.; Scott, D. Pen-sized digital 30-second blood glucose meter. *Lancet* **1987**, *329*, 778-779.
18. Martinez, A. W.; Phillips, S. T.; Butte, M. J.; Whitesides, G. M. Patterned paper as a platform for

inexpensive, low-volume, portable bioassays. *Angew. Chem., Int. Ed.* **2007**, *46*, 1318-1320.

19. Martinez, A. W.; Phillips, S. T.; Whitesides, G. M. *Three-dimensional microfluidic devices fabricated in layered paper and tape*. *Proc. Natl. Acad. Sci. U.S.A.* **2008**, *105*, 19606-19611.
20. Carrilho, E.; Martinez, A. W.; Whitesides, G. M. *Understanding Wax Printing: A Simple Micropatterning Process for Paper-Based Microfluidics*. *Anal. Chem.* **2009**, *81*, 7091-7095.
21. Jiang, X.; Fan, Z. H. *Fabrication and Operation of Paper-Based Analytical Devices*. *Annu. Rev. Anal. Chem.* **2016**, *9*, 203-22.
22. Li, X.; Tian, J.; Nguyen, T.; Shen, W. *Paper-based microfluidic devices by plasma treatment*. *Anal. Chem.* **2008**, *80*, 9131-9134.
23. Bruzewicz, D. A.; Reches, M.; Whitesides, G. M. *Low-cost printing of poly (dimethylsiloxane) barriers to define microchannels in paper*. *Anal. Chem.* **2008**, *80*, 3387-3392.
24. Fenton, E. M.; Mascarenas, M. R.; López, G. P.; Sibbett, S. S. *Multiplex lateral-flow test strips fabricated by two-dimensional shaping*. *ACS Appl. Mater. Interfaces* **2008**, *1*, 124-129.
25. Abe, K.; Suzuki, K.; Citterio, D. *Inkjet-printed microfluidic multianalyte chemical sensing paper*. *Anal. Chem.* **2008**, *80*, 6928-6934.
26. Maejima, K.; Tomikawa, S.; Suzuki, K.; Citterio, D. *Inkjet printing: an integrated and green chemical approach to microfluidic paper-based analytical devices*. *Rsc Adv.* **2013**, *3*, 9258-9263.

27. Kwong, P.; Gupta, M. Vapor phase deposition of functional polymers onto paper-based microfluidic devices for advanced unit operations. Anal. Chem. **2012**, *84*, 10129-10135.
28. Olkkonen, J.; Lehtinen, K.; Erho, T. Flexographically printed fluidic structures in paper. Anal. Chem. **2010**, *82*, 10246-10250.
29. de Tarso Garcia, P.; Cardoso, T. M. G.; Garcia, C. D.; Carrilho, E.; Coltro, W. K. T. A handheld stamping process to fabricate microfluidic paper-based analytical devices with chemically modified surface for clinical assays. Rsc Adv. **2014**, *4*, 37637-37644.
30. Mahadeva, S. K.; Walus, K.; Stoeber, B. Paper as a platform for sensing applications and other devices: A review. ACS Appl. Mater. Interfaces **2015**, *7*, 8345-8362.
31. Yang, Y.; Noviana, E.; Nguyen, M. P.; Geiss, B. J.; Dandy, D. S.; Henry, C. S. Paper-Based Microfluidic Devices: Emerging Themes and Applications. Anal. Chem. **2016**.
32. Anderson, J. R.; Chiu, D. T.; Jackman, R. J.; Cherniavskaya, O.; McDonald, J. C.; Wu, H.; Whitesides, S. H.; Whitesides, G. M. Fabrication of topologically complex three-dimensional microfluidic systems in PDMS by rapid prototyping. Anal. Chem. **2000**, *72*, 3158-3164.
33. Unger, M. A.; Chou, H.-P.; Thorsen, T.; Scherer, A.; Quake, S. R. Monolithic microfabricated valves and pumps by multilayer soft lithography. Science **2000**, *288*, 113-116.
34. Luo, Y.; Zare, R. N. Perforated membrane method for fabricating three-dimensional polydimethylsiloxane microfluidic devices. Lab Chip **2008**, *8*, 1688-1694.

35. Kartalov, E. P.; Walker, C.; Taylor, C. R.; Anderson, W. F.; Scherer, A. Microfluidic vias enable nested bioarrays and autoregulatory devices in Newtonian fluids. *Proc. Natl. Acad. Sci. U.S.A.* **2006**, *103*, 12280-12284.
36. Bhargava, K. C.; Thompson, B.; Malmstadt, N. Discrete elements for 3D microfluidics. *Proc. Natl. Acad. Sci. U.S.A.* **2014**, *111*, 15013-15018.
37. Liu, H.; Xiang, Y.; Lu, Y.; Crooks, R. M. Aptamer-Based Origami Paper Analytical Device for Electrochemical Detection of Adenosine. *Angew. Chem., Int. Ed.* **2012**, *51*, 6925-6928.
38. Washburn, E. W. The dynamics of capillary flow. *Phys. Rev.* **1921**, *17*, 273.
39. Mendez, S.; Fenton, E. M.; Gallegos, G. R.; Petsev, D. N.; Sibbett, S. S.; Stone, H. A.; Zhang, Y.; López, G. P. Imbibition in porous membranes of complex shape: quasi-stationary flow in thin rectangular segments. *Langmuir* **2009**, *26*, 1380-1385.
40. Apilux, A.; Ukita, Y.; Chikae, M.; Chailapakul, O.; Takamura, Y. Development of automated paper-based devices for sequential multistep sandwich enzyme-linked immunosorbent assays using inkjet printing. *Lab Chip* **2013**, *13*, 126-135.
41. Lutz, B.; Liang, T.; Fu, E.; Ramachandran, S.; Kauffman, P.; Yager, P. Dissolvable fluidic time delays for programming multi-step assays in instrument-free paper diagnostics. *Lab Chip* **2013**, *13*, 2840-2847.
42. Li, X.; Zwanenburg, P.; Liu, X. Magnetic timing valves for fluid control in paper-based microfluidics. *Lab Chip* **2013**, *13*, 2609-2614.

43. Liu, H.; Li, X.; Crooks, R. M. Paper-Based SlipPAD for High-Throughput Chemical Sensing. *Anal. Chem.* **2013**, *85*, 4263-4267.
44. Renault, C.; Li, X.; Fosdick, S. E.; Crooks, R. M. Hollow-channel paper analytical devices. *Anal. Chem.* **2013**, *85*, 7976-7979.
45. Renault, C.; Koehne, J.; Ricco, A. J.; Crooks, R. M. Three-Dimensional Wax Patterning of Paper Fluidic Devices. *Langmuir* **2014**, *30*, 7030-7036.
46. Renault, C.; Anderson, M. J.; Crooks, R. M. Electrochemistry in Hollow-Channel Paper Analytical Devices. *J. Am. Chem. Soc.* **2014**, *136*, 4616-4623.
47. Li, L.; Ismagilov, R. F. Protein crystallization using microfluidic technologies based on valves, droplets, and SlipChip. *Annu. Rev. Biophys.* **2010**, *39*, 139-158.
48. Pompano, R. R.; Liu, W.; Du, W.; Ismagilov, R. F. Microfluidics using spatially defined arrays of droplets in one, two, and three dimensions. *Annu. Rev. Anal. Chem.* **2011**, *4*, 59-81.
49. Glavan, A. C.; Martinez, R. V.; Maxwell, E. J.; Subramaniam, A. B.; Nunes, R. M.; Soh, S.; Whitesides, G. M. Rapid fabrication of pressure-driven open-channel microfluidic devices in omniphobic RF paper. *Lab Chip* **2013**, *13*, 2922-2930.
50. Nie, J.; Liang, Y.; Zhang, Y.; Le, S.; Li, D.; Zhang, S. One-step patterning of hollow microstructures in paper by laser cutting to create microfluidic analytical devices. *Analyst* **2013**, *138*, 671-676.
51. Liu, B.; Du, D.; Hua, X.; Yu, X. Y.; Lin, Y. Paper-Based Electrochemical Biosensors: From Test Strips to Paper-Based Microfluidics. *Electroanalysis* **2014**, *26*, 1214-1223.

52. Gencoglu, A.; Minerick, A. R. Electrochemical detection techniques in micro-and nanofluidic devices. *Microfluid. Nanofluid.* **2014**, *17*, 781-807.
53. Rowe, A. A.; Bonham, A. J.; White, R. J.; Zimmer, M. P.; Yadgar, R. J.; Hobza, T. M.; Honea, J. W.; Ben-Yaacov, I.; Plaxco, K. W. CheapStat: An open-source,"do-it-yourself" potentiostat for analytical and educational applications. *Plos One* **2011**, *6*, e23783.
54. Dungchai, W.; Chailapakul, O.; Henry, C. S. Electrochemical detection for paper-based microfluidics. *Anal. Chem.* **2009**, *81*, 5821-5826.
55. Mandal, P.; Dey, R.; Chakraborty, S. Electrokinetics with "paper-and-pencil" devices. *Lab Chip* **2012**, *12*, 4026-4028.
56. Nie, Z. H.; Nijhuis, C. A.; Gong, J. L.; Chen, X.; Kumachev, A.; Martinez, A. W.; Narovlyansky, M.; Whitesides, G. M. Electrochemical sensing in paper-based microfluidic devices. *Lab Chip* **2010**, *10*, 477-483.
57. Scida, K.; Cunningham, J. C.; Renault, C.; Richards, I.; Crooks, R. M. Simple, Sensitive, and Quantitative Electrochemical Detection Method for Paper Analytical Devices. *Anal. Chem.* **2014**, *86*, 6501-6507.
58. Lan, W.-J.; Maxwell, E. J.; Parolo, C.; Bwambok, D. K.; Subramaniam, A. B.; Whitesides, G. M. Paper-based electroanalytical devices with an integrated, stable reference electrode. *Lab Chip* **2013**, *13*, 4103-4108.
59. Wang, Y.; Ge, L.; Wang, P.; Yan, M.; Ge, S.; Li, N.; Yu, J.; Huang, J. Photoelectrochemical lab-on-paper device equipped with a porous Au-paper electrode and fluidic delay-switch for sensitive detection of DNA hybridization. *Lab Chip* **2013**, *13*, 3945-3955.

60. Maxwell, E. J.; Mazzeo, A. D.; Whitesides, G. M. Paper-based electroanalytical devices for accessible diagnostic testing. *MRS Bull.* **2013**, *38*, 309-314.
61. Magdeldin, S., Ed. *Gel Electrophoresis - Principles and Basics*. InTech: Croatia, 2012.
62. Tiselius, A. A new apparatus for electrophoretic analysis of colloidal mixtures. *Trans. Faraday Soc.* **1937**, *33*, 524-531.
63. Martin, N.; Franglen, G. The use and limitations of filter-paper electrophoresis. *J. Clin. Pathol.* **1954**, *7*, 87-105.
64. Scopes, R. Methods for starch-gel electrophoresis of sarcoplasmic proteins. An investigation of the relative mobilities of the glycolytic enzymes from the muscles of a variety of species. *Biochem. J.* **1968**, *107*, 139-150.
65. Thorne, H. Electrophoretic separation of polyoma virus DNA from host cell DNA. *Virology* **1966**, *29*, 234-239.
66. Meyers, J. A.; Sanchez, D.; Elwell, L. P.; Falkow, S. Simple agarose gel electrophoretic method for the identification and characterization of plasmid deoxyribonucleic acid. *J. Bacteriol.* **1976**, *127*, 1529-1537.
67. Giri, K. Two-Dimensional Agar Electrophoresis of Serum Mucoproteins. **1957**.
68. Bachvaroff, R.; McMaster, P. R. Separation of microsomal RNA into five bands during agar electrophoresis. *Science* **1964**, *143*, 1177-1179.
69. Chrambach, A.; Rodbard, D. Polyacrylamide gel electrophoresis. *Science* **1971**, *172*, 440-451.
70. Weber, K.; Osborn, M. The reliability of molecular weight determinations by dodecyl sulfate-polyacrylamide

gel electrophoresis. *J. Biol. Chem.* **1969**, *244*, 4406-4412.

71. Schägger, H.; Von Jagow, G. *Tricine-sodium dodecyl sulfate-polyacrylamide gel electrophoresis for the separation of proteins in the range from 1 to 100 kDa*. *Anal. Biochem.* **1987**, *166*, 368-379.
72. Pedersen-Bjergaard, S.; Rasmussen, K. E. *Liquid-liquid-liquid microextraction for sample preparation of biological fluids prior to capillary electrophoresis*. *Anal. Chem.* **1999**, *71*, 2650-2656.
73. Neuhoff, V.; Arold, N.; Taube, D.; Ehrhardt, W. *Improved staining of proteins in polyacrylamide gels including isoelectric focusing gels with clear background at nanogram sensitivity using Coomassie Brilliant Blue G-250 and R-250*. *Electrophoresis* **1988**, *9*, 255-262.
74. Bjellqvist, B.; Ek, K.; Righetti, P. G.; Gianazza, E.; Görg, A.; Westermeier, R.; Postel, W. *Isoelectric focusing in immobilized pH gradients: principle, methodology and some applications*. *J. Biochem. Biophys. Methods* **1982**, *6*, 317-339.
75. Ge, L.; Wang, S.; Ge, S.; Yu, J.; Yan, M.; Li, N.; Huang, J. *Electrophoretic separation in a microfluidic paper-based analytical device with an on-column wireless electrogenerated chemiluminescence detector*. *Chem. Commun.* **2014**, *50*, 5699-5702.
76. Chen, S. S.; Hu, C. W.; Yu, I. F.; Liao, Y. C.; Yang, J. T. *Origami paper-based fluidic batteries for portable electrophoretic devices*. *Lab Chip* **2014**, *14*, 2124-2130.

77. Scida, K.; Li, B. L.; Ellington, A. D.; Crooks, R. M. DNA Detection Using Origami Paper Analytical Devices. Anal. Chem. **2013**, 85, 9713-9720.
78. Ge, L.; Wang, S. M.; Song, X. R.; Ge, S. G.; Yu, J. H. 3D Origami-based multifunction-integrated immunodevice: low-cost and multiplexed sandwich chemiluminescence immunoassay on microfluidic paper-based analytical device. Lab Chip **2012**, 12, 3150-3158.
79. Cybulski, J. S.; Clements, J.; Prakash, M. Foldscope: Origami-Based Paper Microscope. Plos One **2014**, 9, e98781.
80. Lathrop, D. K.; Ervin, E. N.; Barrall, G. A.; Keehan, M. G.; Kawano, R.; Krupka, M. A.; White, H. S.; Hibbs, A. H. Monitoring the escape of DNA from a nanopore using an alternating current signal. J. Am. Chem. Soc. **2010**, 132, 1878-1885.
81. Bell, P. J.; Karuso, P. Epicocconone, A Novel Fluorescent Compound from the Fungus Epicoccum n igrum. J. Am. Chem. Soc. **2003**, 125, 9304-9305.
82. Hlushkou, D.; Perdue, R. K.; Dhopeshwarkar, R.; Crooks, R. M.; Tallarek, U. Electric field gradient focusing in microchannels with embedded bipolar electrode. Lab Chip **2009**, 9, 1903-1913.
83. Renkin, E. M. Filtration, diffusion, and molecular sieving through porous cellulose membranes. J. Gen. Physiol. **1954**, 38, 225-243.
84. Kunkel, H. G.; Tiselius, A. Electrophoresis of proteins on filter paper. J. Gen. Physiol. **1951**, 35, 89-118.
85. Moghadam, B. Y.; Connelly, K. T.; Posner, J. D. Isotachophoretic Preconcenetration on Paper-Based Microfluidic Devices. Anal. Chem. **2014**, 86, 5829-5837.

86. Oh, Y.-J.; Gamble, T. C.; Leonhardt, D.; Chung, C.-H.; Brueck, S. R. J.; Ivory, C. F.; Lopez, G. P.; Petsev, D. N.; Han, S. M. Monitoring FET flow control and wall adsorption of charged fluorescent dye molecules in nanochannels integrated into a multiple internal reflection infrared waveguide. *Lab Chip* **2008**, *8*, 251-258.
87. Wu, J.; Gerstandt, K.; Zhang, H.; Liu, J.; Hinds, B. J. Electrophoretically induced aqueous flow through single-walled carbon nanotube membranes. *Nature Nanotech.* **2012**, *7*, 133-139.
88. Laws, D. R.; Hlushkou, D.; Perdue, R. K.; Tallarek, U.; Crooks, R. M. Bipolar electrode focusing: simultaneous concentration enrichment and separation in a microfluidic channel containing a bipolar electrode. *Anal. Chem.* **2009**, *81*, 8923-8929.
89. Milanova, D.; Chambers, R. D.; Bahga, S. S.; Santiago, J. G. Electrophoretic mobility measurements of fluorescent dyes using on-chip capillary electrophoresis. *Electrophoresis* **2011**, *32*, 3286-3294.
90. Jeppson, J.; Laurell, C.; Franzen, B. Agarose gel electrophoresis. *Clin. Chem.* **1979**, *25*, 629-638.
91. Kyle, R.; Katzmann, J.; Lust, J.; Dispenzieri, A., *Clinical Indications and Applications of Electrophoresis and Immunofixation*, in *Manual of Clinical Immunology*, N. Rose, R. Hamiliton, and B. Detrick, Editors. 2002, ASM Press: Washington DC. p. 66-70.
92. Josephson, R.; Mikolajick, E.; Sinha, D. Gel isoelectric focusing of selected bovine immunoglobulins. *J. Dairy Sci.* **1972**, *55*, 1508-1510.

93. Abramson, H. A.; Moyer, L. S.; Gorin, M. H. *Electrophoresis of Proteins and the Chemistry of Cell Surfaces*. Hafner Publishing Company, Inc.: New York, 1942.
94. Dawson, R. M. C. *Data for Biochemical Research, 3rd*. Clarendon Press: Oxford, 1989.
95. Putnam, F. W., Ed. *The Plasma Proteins: Structure, Function, and Genetic Control*. Vol. 3. Elsevier: London, 2012.
96. Jung, B.; Bharadwaj, R.; Santiago, J. G. On-chip millionfold sample stacking using transient isotachophoresis. *Anal. Chem.* **2006**, *78*, 2319-2327.
97. Luo, L.; Li, X.; Crooks, R. M. Low-Voltage Origami-Paper-Based Electrophoretic Device for Rapid Protein Separation. *Anal. Chem.* **2014**, *86*, 12390-12397.
98. Du, W. B.; Li, L.; Nichols, K. P.; Ismagilov, R. F. SlipChip. *Lab Chip* **2009**, *9*, 2286-2292.
99. Shen, F.; Du, W. B.; Kreutz, J. E.; Fok, A.; Ismagilov, R. F. Digital PCR on a SlipChip. *Lab Chip* **2010**, *10*, 2666-2672.
100. Rosenfeld, T.; Bercovici, M. 1000-fold sample focusing on paper-based microfluidic devices. *Lab Chip* **2014**, *14*, 4465-4474.
101. Moghadam, B. Y.; Connelly, K. T.; Posner, J. D. Two Orders of Magnitude Improvement in Detection Limit of Lateral Flow Assays Using Isotachophoresis. *Anal. Chem.* **2015**, *87*, 1009-1017.
102. Carrilho, E.; Phillips, S. T.; Vella, S. J.; Martinez, A. W.; Whitesides, G. M. Paper microzone plates. *Anal. Chem.* **2009**, *81*, 5990-5998.
103. Ellerbee, A. K.; Phillips, S. T.; Siegel, A. C.; Mirica, K. A.; Martinez, A. W.; Striehl, P.; Jain, N.;

Prentiss, M.; Whitesides, G. M. Quantifying Colorimetric Assays in Paper-Based Microfluidic Devices by Measuring the Transmission of Light through Paper. Anal. Chem. **2009**, *81*, 8447-8452.

104. *Zhao, W.; Ali, M. M.; Aguirre, S. D.; Brook, M. A.; Li, Y. Paper-based bioassays using gold nanoparticle colorimetric probes. Anal. Chem.* **2008**, *80*, 8431-8437.
105. *Zhang, X.; Li, J.; Chen, C.; Lou, B.; Zhang, L.; Wang, E. A self-powered microfluidic origami electrochemiluminescence biosensing platform. Chem. Commun.* **2013**, *49*, 3866-3868.
106. *Ge, L.; Yan, J.; Song, X.; Yan, M.; Ge, S.; Yu, J. Three-dimensional paper-based electrochemiluminescence immunodevice for multiplexed measurement of biomarkers and point-of-care testing. Biomaterials* **2012**, *33*, 1024-1031.
107. *Delaney, J. L.; Hogan, C. F.; Tian, J.; Shen, W. Electrogenerated chemiluminescence detection in paper-based microfluidic sensors. Anal. Chem.* **2011**, *83*, 1300-1306.
108. *Parolo, C.; Merkoçi, A. Paper-based nanobiosensors for diagnostics. Chem. Soc. Rev.* **2013**, *42*, 450-457.
109. *Persat, A.; Marshall, L. A.; Santiago, J. G. Purification of nucleic acids from whole blood using isotachophoresis. Anal. Chem.* **2009**, *81*, 9507-9511.
110. *Walker, P. A.; Morris, M. D.; Burns, M. A.; Johnson, B. N. Isotachophoretic separations on a microchip. Normal Raman spectroscopy detection. Anal. Chem.* **1998**, *70*, 3766-3769.
111. *Everaerts, F. M.; Beckers, J. L.; Verheggen, T. P. Isotachophoresis: theory, instrumentation and applications*. Elsevier, 2011.

112. Qu, Y. T.; Marshall, L. A.; Santiago, J. G. Simultaneous Purification and Fractionation of Nucleic Acids and Proteins from Complex Samples Using Bidirectional Isotachophoresis. *Anal. Chem.* **2014**, *86*, 7264-7268.
113. Malá, Z.; Gebauer, P.; Bo ek, P. Recent progress in analytical capillary isotachophoresis. *Electrophoresis* **2013**, *34*, 19-28.
114. Smejkal, P.; Bottenus, D.; Breadmore, M. C.; Guijt, R. M.; Ivory, C. F.; Foret, F.; Macka, M. Microfluidic isotachophoresis: A review. *Electrophoresis* **2013**, *34*, 1493-1509.
115. Bahga, S. S.; Santiago, J. G. Coupling isotachophoresis and capillary electrophoresis: a review and comparison of methods. *Analyst* **2013**, *138*, 735-754.
116. Bercovici, M.; Han, C. M.; Liao, J. C.; Santiago, J. G. Rapid hybridization of nucleic acids using isotachophoresis. *Proc. Natl. Acad. Sci. U.S.A.* **2012**, *109*, 11127-11132.
117. Garcia-Schwarz, G.; Santiago, J. G. Rapid High-Specificity microRNA Detection Using a Two-stage Isotachophoresis Assay. *Angew. Chem.* **2013**, *125*, 11748-11751.
118. Chambers, R. D.; Santiago, J. G. Imaging and Quantification of Isotachophoresis Zones Using Nonfocusing Fluorescent Tracers. *Anal. Chem.* **2009**, *81*, 3022-3028.
119. Lodish, H. F.; Berk, A.; Zipursky, S. L.; Matsudaira, P.; Baltimore, D.; Darnell, J. *Molecular cell biology*. Vol. 4. Citeseer, 2000.
120. Davis, L. *Basic methods in molecular biology*. Elsevier, 2012.

121. Araújo, A. C.; Song, Y.; Lundeberg, J.; Ståhl, P. L.; Brumer III, H. Activated paper surfaces for the rapid hybridization of DNA through capillary transport. *Anal. Chem.* **2012**, *84*, 3311-3317.
122. Anand, R. K.; Sheridan, E.; Knust, K. N.; Crooks, R. M. Bipolar electrode focusing: faradaic ion concentration polarization. *Anal. Chem.* **2011**, *83*, 2351-2358.
123. Zangle, T. A.; Mani, A.; Santiago, J. G. Theory and experiments of concentration polarization and ion focusing at microchannel and nanochannel interfaces. *Chem. Soc. Rev.* **2010**, *39*, 1014-1035.
124. Kim, S. J.; Ko, S. H.; Kang, K. H.; Han, J. Direct seawater desalination by ion concentration polarization. *Nature Nanotech.* **2010**, *5*, 297-301.
125. Crooks, R. M. Principles of Bipolar Electrochemistry. *ChemElectroChem* **2016**, *3*, 357-359.
126. Fosdick, S. E.; Knust, K. N.; Scida, K.; Crooks, R. M. Bipolar Electrochemistry. *Angew. Chem., Int. Ed.* **2013**, *52*, 10438-10456.
127. Dhopeshwarkar, R.; Hlushkou, D.; Nguyen, M.; Tallarek, U.; Crooks, R. M. Electrokinetics in microfluidic channels containing a floating electrode. *J. Am. Chem. Soc.* **2008**, *130*, 10480-10481.
128. Mavré, F.; Anand, R. K.; Laws, D. R.; Chow, K.-F.; Chang, B.-Y.; Crooks, J. A.; Crooks, R. M. Bipolar electrodes: a useful tool for concentration, separation, and detection of analytes in microelectrochemical systems. *Anal. Chem.* **2010**, *82*, 8766-8774.
129. Loget, G.; Zigah, D.; Bouffier, L.; Sojic, N.; Kuhn, A. Bipolar electrochemistry: from materials science to

motion and beyond. *Acc. Chem. Res.* **2013**, *46*, 2513-2523.

130. Hu, J.; Wang, S.; Wang, L.; Li, F.; Pingguan-Murphy, B.; Lu, T. J.; Xu, F. Advances in paper-based point-of-care diagnostics. *Biosens. Bioelectron.* **2014**, *54*, 585-597.
131. Sackmann, E. K.; Fulton, A. L.; Beebe, D. J. The present and future role of microfluidics in biomedical research. *Nature* **2014**, *507*, 181-189.
132. Lin, C.-C.; Hsu, J.-L.; Lee, G.-B. Sample preconcentration in microfluidic devices. *Microfluid. Nanofluid.* **2011**, *10*, 481-511.
133. Slouka, Z.; Senapati, S.; Chang, H.-C. Microfluidic systems with ion-selective membranes. *Annu. Rev. Anal. Chem.* **2014**, *7*, 317-335.
134. Abbas, A.; Brimer, A.; Slocik, J. M.; Tian, L.; Naik, R. R.; Singamaneni, S. Multifunctional analytical platform on a paper strip: separation, preconcentration, and subattomolar detection. *Anal. Chem.* **2013**, *85*, 3977-3983.
135. Li, X.; Luo, L.; Crooks, R. M. Low-voltage paper isotachophoresis device for DNA focusing. *Lab Chip* **2015**, *15*, 4090-4098.
136. Byrnes, S.; Bishop, J.; Lafleur, L.; Buser, J.; Lutz, B.; Yager, P. One-step purification and concentration of DNA in porous membranes for point-of-care applications. *Lab Chip* **2015**, *15*, 2647-2659.
137. Kim, S. J.; Song, Y.-A.; Han, J. Nanofluidic concentration devices for biomolecules utilizing ion concentration polarization: theory, fabrication, and applications. *Chem. Soc. Rev.* **2010**, *39*, 912-922.

138. Li, M.; Anand, R. K. Recent advancements in ion concentration polarization. *Analyst* **2016**, *141*, 3496-3510.
139. Gong, M. M.; Nosrati, R.; San Gabriel, M. C.; Zini, A.; Sinton, D. Direct DNA analysis with paper-based ion concentration polarization. *J. Am. Chem. Soc.* **2015**, *137*, 13913-13919.
140. Gong, M. M.; Zhang, P.; MacDonald, B. D.; Sinton, D. Nanoporous membranes enable concentration and transport in fully wet paper-based assays. *Anal. Chem.* **2014**, *86*, 8090-8097.
141. Yang, R.-J.; Pu, H.-H.; Wang, H.-L. Ion concentration polarization on paper-based microfluidic devices and its application to preconcentrate dilute sample solutions. *Biomicrofluidics* **2015**, *9*, 014122.
142. Han, S. I.; Hwang, K. S.; Kwak, R.; Lee, J. H. Microfluidic paper-based biomolecule preconcentrator based on ion concentration polarization. *Lab Chip* **2016**, *16*, 2219-2227.
143. Hong, S.; Kwak, R.; Kim, W. Paper-Based Flow Fractionation System Applicable to Preconcentration and Field-Flow Separation. *Anal. Chem.* **2016**, *88*, 1682-1687.
144. Yeh, S.-H.; Chou, K.-H.; Yang, R.-J. Sample pre-concentration with high enrichment factors at a fixed location in paper-based microfluidic devices. *Lab Chip* **2016**, *16*, 925-931.
145. Li, X.; Scida, K.; Crooks, R. M. Detection of Hepatitis B Virus DNA with a Paper Electrochemical Sensor. *Anal. Chem.* **2015**, *87*, 9009-9015.
146. Knust, K. N.; Sheridan, E.; Anand, R. K.; Crooks, R. M. Dual-channel bipolar electrode focusing: simultaneous

separation and enrichment of both anions and cations. *Lab Chip* **2012**, *12*, 4107-4114.

147. Perdue, R. K.; Laws, D. R.; Hlushkou, D.; Tallarek, U.; Crooks, R. M. Bipolar electrode focusing: the effect of current and electric field on concentration enrichment. *Anal. Chem.* **2009**, *81*, 10149-10155.
148. Sheridan, E.; Hlushkou, D.; Knust, K. N.; Tallarek, U.; Crooks, R. M. Enrichment of cations via bipolar electrode focusing. *Anal. Chem.* **2012**, *84*, 7393-7399.
149. Hanauer, M.; Pierrat, S.; Zins, I.; Lotz, A.; Sönnichsen, C. Separation of nanoparticles by gel electrophoresis according to size and shape. *Nano Lett.* **2007**, *7*, 2881-2885.
150. Zhang, X.; Servos, M. R.; Liu, J. W. Instantaneous and Quantitative Functionalization of Gold Nanoparticles with Thiolated DNA Using a pH-Assisted and Surfactant-Free Route. *J. Am. Chem. Soc.* **2012**, *134*, 7266-7269.
151. Dequaire, M.; Degrand, C.; Limoges, B. An electrochemical metalloimmunoassay based on a colloidal gold label. *Anal. Chem.* **2000**, *72*, 5521-5528.
152. Li, L.; Ismagilov, R. F. Protein Crystallization Using Microfluidic Technologies Based on Valves, Droplets and SlipChip. *Annu. Rev. Biophys.* **2010**, *39*, 139-158.
153. Cao, Y. W. C.; Jin, R. C.; Mirkin, C. A. Nanoparticles with Raman spectroscopic fingerprints for DNA and RNA detection. *Science* **2002**, *297*, 1536-1540.
154. Rehermann, B.; Nascimbeni, M. Immunology of hepatitis B virus and hepatitis C virus infection. *Nat. Rev. Immunol.* **2005**, *5*, 215-229.
155. Bottcher, B.; Wynne, S. A.; Crowther, R. A. Determination of the fold of the core protein of

hepatitis B virus by electron cryomicroscopy. *Nature* **1997**, *386*, 88-91.

156. Beasley, R. P.; Lin, C.-C.; Hwang, L.-Y.; Chien, C.-S. *Hepatocellular carcinoma and hepatitis B virus: a prospective study of 22 707 men in Taiwan*. *Lancet* **1981**, *318*, 1129-1133.
157. Brechot, C.; Scotto, J.; Charnay, P.; Hadchouel, M.; Degos, F.; Trepo, C.; Tiollais, P. *Detection of hepatitis B virus DNA in liver and serum: a direct appraisal of the chronic carrier state*. *Lancet* **1981**, *318*, 765-768.
158. Gupta, B. P.; Jayasuryan, N.; Jameel, S. *Direct detection of hepatitis B virus from dried blood spots by polymerase chain reaction amplification*. *J. Clin. Microbiol.* **1992**, *30*, 1913-1916.
159. Hadziyannis, S. J.; Lieberman, H. M.; Karvountzis, G. G.; Shafritz, D. A. *Analysis of Liver Disease, Nuclear HBcAg, Viral Replication, and Hepatitis B Virus DNA in Liver and Serum of HBcAg Vs. Anti-HBe Positive Carriers of Hepatitis B Virus*. *Hepatology* **1983**, *3*, 656-662.
160. Ulrich, P. P.; Bhat, R. A.; Seto, B.; Mack, D.; Sninsky, J.; Vyas, G. N. *Enzymatic amplification of hepatitis B virus DNA in serum compared with infectivity testing in chimpanzees*. *J. Infect. Dis.* **1989**, *160*, 37-43.
161. Caliendo, A. M.; Valsamakis, A.; Bremer, J. W.; Ferreira-Gonzalez, A.; Granger, S.; Sabatini, L.; Tsongalis, G. J.; Wang, Y. F. W.; Yen-Lieberman, B.; Young, S. *Multilaboratory evaluation of real-time PCR tests for hepatitis B virus DNA quantification*. *J. Clin. Microbiol.* **2011**, *49*, 2854-2858.

162. Li, M.; Cushing, S. K.; Liang, H.; Suri, S.; Ma, D.; Wu, N. Plasmonic nanorice antenna on triangle nanoarray for surface-enhanced raman scattering detection of hepatitis B virus DNA. *Anal. Chem.* **2013**, *85*, 2072-2078.
163. Lu, X.; Dong, X.; Zhang, K.; Han, X.; Fang, X.; Zhang, Y. A gold nanorods-based fluorescent biosensor for the detection of hepatitis B virus DNA based on fluorescence resonance energy transfer. *Analyst* **2013**, *138*, 642-650.
164. Bastian, L. A.; Nanda, K.; Hasselblad, V.; Simel, D. L. Diagnostic efficiency of home pregnancy test kits: a meta-analysis. *Arch. Fam. Med.* **1998**, *7*, 465.
165. Posthuma-Trumpie, G. A.; Korf, J.; van Amerongen, A. Lateral flow (immuno) assay: its strengths, weaknesses, opportunities and threats. A literature survey. *Anal. Bioanal. Chem.* **2009**, *393*, 569-582.
166. Fu, E.; Ramsey, S. A.; Kauffman, P.; Lutz, B.; Yager, P. Transport in two-dimensional paper networks. *Microfluid. Nanofluid.* **2011**, *10*, 29-35.
167. Ballerini, D. R.; Li, X.; Shen, W. Patterned paper and alternative materials as substrates for low-cost microfluidic diagnostics. *Microfluid. Nanofluid.* **2012**, *13*, 769-787.
168. Cate, D. M.; Dungchai, W.; Cunningham, J. C.; Volckens, J.; Henry, C. S. Simple, distance-based measurement for paper analytical devices. *Lab Chip* **2013**, *13*, 2397-2404.
169. Cunningham, J. C.; Brenes, N. J.; Crooks, R. M. Paper Electrochemical Device for Detection of DNA and Thrombin by Target-Induced Conformational Switching. *Anal. Chem.* **2014**, *86*, 6166-6170.

170. Li, B.; Zhang, W.; Chen, L.; Lin, B. A fast and low-cost spray method for prototyping and depositing surface-enhanced Raman scattering arrays on microfluidic paper based device. *Electrophoresis* **2013**, *34*, 2162-2168.
171. Lee, C. H.; Hankus, M. E.; Tian, L.; Pellegrino, P. M.; Singamaneni, S. Highly sensitive surface enhanced Raman scattering substrates based on filter paper loaded with plasmonic nanostructures. *Anal. Chem.* **2011**, *83*, 8953-8958.
172. Ho, J.; Tan, M. K.; Go, D. B.; Yeo, L. Y.; Friend, J. R.; Chang, H.-C. Paper-based microfluidic surface acoustic wave sample delivery and ionization source for rapid and sensitive ambient mass spectrometry. *Anal. Chem.* **2011**, *83*, 3260-3266.
173. Lutz, B. R.; Trinh, P.; Ball, C.; Fu, E.; Yager, P. Two-dimensional paper networks: programmable fluidic disconnects for multi-step processes in shaped paper. *Lab Chip* **2011**, *11*, 4274-4278.
174. Zhang, X.; Servos, M. R.; Liu, J. W. Fast pH-assisted functionalization of silver nanoparticles with monothiolated DNA. *Chem. Commun.* **2012**, *48*, 10114-10116.
175. Zhang, X.; Servos, M. R.; Liu, J. Instantaneous and quantitative functionalization of gold nanoparticles with thiolated DNA using a pH-assisted and surfactant-free route. *J. Am. Chem. Soc.* **2012**, *134*, 7266-7269.
176. Zou, S.; Janel, N.; Schatz, G. C. Silver nanoparticle array structures that produce remarkably narrow plasmon lineshapes. *J. Chem. Phys.* **2004**, *120*, 10871-10875.
177. Lu, Y.; Liu, G. L.; Lee, L. P. High-density silver nanoparticle film with temperature-controllable

interparticle spacing for a tunable surface enhanced Raman scattering substrate. *Nano Lett.* **2005**, *5*, 5-9.

178. Chaloupka, K.; Malam, Y.; Seifalian, A. M. *Nanosilver as a new generation of nanoproduct in biomedical applications*. *Trends Biotechnol.* **2010**, *28*, 580-588.
179. Cao, Y.; Jin, R.; Mirkin, C. A. *DNA-modified core-shell Ag/Au nanoparticles*. *J. Am. Chem. Soc.* **2001**, *123*, 7961-7962.
180. Rodbard, D.; Feldman, Y.; Jaffe, M.; Miles, L. *Kinetics of two-site immunoradiometric ('sandwich`) assays—II: Studies on the nature of the-high-dose hook effect*. *Immunochemistry* **1978**, *15*, 77-82.
181. Chen, C. J.; Yang, H. I.; Iloeje, U. H. *Hepatitis B virus DNA levels and outcomes in chronic hepatitis B*. *Hepatology* **2009**, *49*, S72-S84.
182. Drummond, T. G.; Hill, M. G.; Barton, J. K. *Electrochemical DNA sensors*. *Nat. Biotechnol.* **2003**, *21*, 1192-1199.
183. Bard, A. J.; Faulkner, L. R. *Electrochemical methods: fundamentals and applications*. Vol. 2. Wiley New York, 1980.
184. Kim, Y. T.; Jung, J. H.; Choi, Y. K.; Seo, T. S. *A packaged paper fluidic-based microdevice for detecting gene expression of influenza A virus*. *Biosens. Bioelectron.* **2014**, *61*, 485-490.